SPACE AND TIME SCALES OF LOW FREQUENCY VARIABILITY IN THE OCEAN

by

Xiaoyun Zang

B.S., Nanjing Institute of Meteorology (1992)
M.S., Institute of Atmospheric Physics, Academia Sinica (1995)

Submitted to the Joint Program in Physical Oceanography
in partial fulfillment of the requirements for the degree of

Master of Science

at the

MASSACHUSETTS INSTITUTE OF TECHNOLOGY
and the

WOODS HOLE OCEANOGRAPHIC INSTITUTION

January 18 1998

Author

Joint Program in Physical Oceanography
Massachusetts Institute of Technology
Woods Hole Oceanographic Institution
January 18,1998

Certified by .....

Carl Wunsch
Cecil and Ida Green Professor of Physical Oceanography
Thesis Supervisor

Accepted by .....

Brechner Owens
Chairman, Joint Committee for Physical Oceanography
Massachusetts Institute of Technology
Woods Hole Oceanographic Institution

SPACE AND TIME SCALES OF LOW FREQUENCY VARIABILITY IN THE OCEAN

by

Xiaoyun Zang

Submitted in partial fulfillment of the requirements for the degree of
Master of Science at the Massachusetts Institute of Technology
and the Woods Hole Oceanographic Institution
January 18,1998

Abstract

We have contrived a regional model $\Phi(K, \omega, n, \phi, \lambda)$ for the distribution of low frequency variability energy in horizontal wavenumber, frequency, vertical mode and geography. We assume horizontal isotropy, $\Phi(K, \omega, n, \phi, \lambda) = 2\pi K \Psi(k, l, \omega, n, \phi, \lambda)$, with K designating the amplitude of total horizontal wavenumber.

The parameters of $\Phi(K, \omega, n, \phi, \lambda)$ can be derived from observations: (i) satellite altimetry measurements yield the surface eddy kinetic energy wavenumber and frequency spectra and the geographic distribution of surface eddy kinetic energy magnitude, (ii) XBT measurements yield the temperature wavenumber spectra, (iii) current meter and thermistor measurements yield the frequency spectra of kinetic energy and temperature, (iv) tomographic measurements yield the frequency spectra of range– and depth–averaged temperature, and (v) the combination of satellite altimetry and current meter measurements yields the vertical partitioning of kinetic energy among dynamical modes. We assume the form of the geography–independent part of our model $\Phi(K, \omega, n) \propto K^p \omega^q$. The observed kinetic energy and temperature wavenumber spectra suggest $p = 3/2$ at $K < K_0$ and $p = -2$ at $K > K_0$ for the barotropic mode, and $p = -1/2$ at $K < K_0$ and $p = -3$ at $K > K_0$ for the baroclinic mods, where K_0 is the transitional wavenumber of the wavenumber spectra. The observed frequency spectra of temperature and kinetic energy suggest that $q = -1/2$ for $\omega < \omega_0$ and $q = -2$ for $\omega > \omega_0$, where ω_0 is the transitional frequency of the frequency spectra. The combination of satellite altimetry and current meter measurements suggests the vertical structure of the low frequency variability is governed by the first few modes. The geography–dependent part of our model is the energy magnitude.

Although we have shown analytically that the tomographic measurements behave as a low–pass filter, it is impossible to identify this filtering effect in the real data due to the strong geographic variability of the energy magnitude and the vertical gradient of the mean temperature. The model wavenumber spectrum is appropriate only where the statistical properties are relatively homogeneous in space.

Thesis Supervisor: Carl Wunsch
Title: Cecil and Ida Green Professor of Physical Oceanography

Acknowledgments

I would first like to thank my advisor, Carl Wunsch, for his encouragement and constructive criticism throughout the course of this work. I am extremely grateful to him for reading this thesis several times, even during weekends and holidays, and for providing feedback promptly. I benefited greatly from his illuminating comments. Above all, he constantly taught me how to communicate effectively.

Many members of the physical oceanography departments at MIT and WHOI have made contributions to this work. In particular, Detlef Stammer generously provided me surface kinetic energy spectra and was ready to talk with me whenever I asked. Glenn Flierl, Nelson Hogg, Rui Xin Huang, Joe Pedlosky and Mike Spall gave me many useful comments. Karl Helfrich kindly supported my first year in the Joint Program.

I am indebted to Dimitris Menemenlis, Brian Dushaw (University of Washington) and Bruce Cornuelle (Scripps Institution of Oceanography) for providing me tomographic data and XBT data. Charmaine King gave me particular support in processing the data and in computing.

I am indebted to my many fellow students. In particular, Brian Arbic, Albert Fischer, Christophe Herbaut and Francois Primeau didn't mind taking all the trouble to read my thesis and to listen to my talks many times. Alexandre Ganachaud was always ready to do me a favor.

My special thanks go to my wife, Bibo Lai, for her love and care.

My first year in the Joint Program was supported by the National Science Foundation under grant OCE 92-16628, then were supported by the National Science Foundation under grant OCE 95-29545.

Contents

Chapter 1

Introduction

The time–dependent motions of the ocean can be divided into several different groups according to their frequencies, e.g. tides, internal waves, inertial waves, etc. Low frequency oceanic variability is one such group of time–dependent motion. By the expression "low frequency variability", we mean the time–dependent motion with a time scale longer than a day and a spatial scale ranging from tens of kilometers to the ocean basin scales. It was not realized that the ocean's general circulation is strongly time–dependent until the 1960s. The main hindrance to our understanding of the ocean general circulation is lack of data. Very little of the ocean has been actually sampled.

In the last decade, the advent of modern measurement technology: ocean acoustic tomography and satellite observations of sea surface topography, enables oceanographers to observe the ocean circulation and its variability on sufficiently fine space and time scales. The principles and applications of satellite remoting and acoustic tomography have been reviewed by Munk and Wunsch [1982]. Satellite altimetry has proven to be extremely important in providing nearly-synoptic and basin–wide observations of the three dimensional state of the sea surface shape $\eta(x, y, t)$. Due to the intimate coupling of the sea surface shape (the slope of the surface) with the near surface geostrophic flow field, altimetric data have become indispensible in in-

vestigating the low frequency oceanic variability. Based on two years of high-quality TOPEX/POSEIDON data, Wunsch and Stammer [1995] constructed the first global frequency-wavenumber spectrum of sea surface height (SSH) variability and related one-dimensional wavenumber spectra for SSH and sea surface slope.

The tomographic method was introduced by Munk and Wunsch [1979] in direct response to the formidable task of measuring and understanding the behaviour of both the mesoscale and larger-scale features associated with the general circulation. Two advantages of the tomographic measurements over the spot measurements are the geometric increase of information with each additional instrument deployed, and the spatial integration inherent in the measurement. We will show analytically that the spatial integration acts as a *low-pass filter*, which filters out the small scale motions. The path–band width of the filter is related to the length of the acoustic ray path.

Combining the results from different measurements, we obtain the following different kinds of spectral descriptions of the oceanic low frequency variability.

Measurement Name	Spectral Type
thermistor	temperature frequency spectra at different depths
current meter	velocity frequency spectra at different depths
X B T	temperature wavenumber spectra at different depths
satellite altimetry	surface kinetic energy frequency–wavenumber spectra
acoustic tomography	range–averaged temperature frequency spectra

Table 1.1: All spectra from different measurements.

In addition, the combination of current meter and altimeter data yields what is the partition of oceanic horizontal kinetic energy among vertical modes [Wunsch 1997].

The low frequency oceanic varibility is a multivariate and multidimensional pro-

cess. We have different kinds of spectra (frequency and wavenumber) for different variables (temperature, velocity and density) at different depths and different places in the ocean. How can we describe this large amount of data using as few parameters as possible? The incentive for this work is to answer this question.

Using linear dynamics under the hypothesis of horizontal isotropy and vertical symmetry of the wave field, Garrett and Munk [1972] patched together a universal simple algebraic representation of the distribution of internal wave energy in wavenumber frequency space in the deep ocean, which has become known as the *Garrett-Munk spectrum*. Later Garrett and Munk [1975] gave an improved version. The GM spectrum is focused on internal waves ($f < \omega < N$). A scientifically interesting problem is to find out whether we can extend the GM spectrum to lower frequencies. We will combine the model, current meter, altimetry, XBT and acoustic methods to produce an analytic wavenumber and frequency spectrum of low frequency oceanic variability with an emphasis on obtaining answers to the following questions: Is there a universal frequency/wavenumber spectrum of the low frequency variability? If not, how do the components of the frequency-wavenumber spectrum (energy level, spectral shape, ...) vary with the physical environment (topography, proximity of large currents, etc.)? Our method is analogous to that of Garrett and Munk [1972].

The three dimensional frequency/wavenumber spectrum is a fundamental element in a description of the ocean circulation variability [Wunsch and Stammer 1995]. The potential use of such a spectrum is wide. First, the spectral representation is important in that most time–dependent phenomena are expressed theoretically in terms of frequency and wavenumber. Therefore, if the data are also expressed in the form of frequency and wavenumber, it will be convenient for comparing and combining the theory with the observations. Second, the three dimensional frequency/wavenumber spectrum tells us how the energy of time–dependent ocean general circulation is distributed among different space and time scales and what are the dominant space and time scales of low frequency variability. Accordingly, the three dimensional fre-

quency/wavenumber spectrum provides a basis for practical filter designing. Third, such a spectrum is also useful for evaluating the quality of the sampled data and for the design of observational strategies. Moreover, it can be used as a standard to judge the skill of the global-scale general circulation models. Stammer et al.[1996] have compared the two dimensional frequency/wavenumber spectrum of TOPEX/POSEIDON data with that of an ocean climate model. The three dimensional frequency/wavenumber spectrum also gives rise to fundamental dynamical and theoretical issues of why the particular spectral forms are displayed by the ocean.

In chapter 2, a simple model is presented, the equations are solved and the solutions are normalized. Chapter 3 presents the frequency spectrum of the spatially averaged temperature as well as the frequency/wavenumber spectra of the kinetic energy and temperature. In chapter 4 the observed properties of ocean low frequency variability are presented and we focus on describing how the low frequency oceanic variability energy is distributed among horizontal wavenumber, frequency and vertical mode. A simple model for the energy density $\Phi(K, \omega, n, \phi, \lambda)$ is contrived in chapter 5. Conclusion and discussion are presented in chapter 6.

Chapter 2

Dynamical model for low-frequency motion

2.1 The governing equations

Away from the equator and beneath the upper mixed layer, the time-dependent motions of the continuously stratified ocean can be described by the following dimensional linearized equations [Gill, 1982]:

$$\frac{\partial \hat{u}}{\partial \hat{t}} - \hat{f}\hat{v} = -\frac{1}{\rho_0}\frac{\partial \hat{p}}{\partial \hat{x}}, \tag{2.1}$$

$$\frac{\partial \hat{v}}{\partial \hat{t}} + \hat{f}\hat{u} = -\frac{1}{\rho_0}\frac{\partial \hat{p}}{\partial \hat{y}}, \tag{2.2}$$

$$0 = -\frac{1}{\rho_0}\frac{\partial \hat{p}}{\partial \hat{z}} - \frac{1}{\rho_0}\hat{\rho}g, \tag{2.3}$$

$$\frac{\partial \hat{\rho}}{\partial \hat{t}} + \hat{w}\frac{\partial \rho_0(z)}{\partial \hat{z}} = 0, \tag{2.4}$$

$$\frac{\partial \hat{u}}{\partial \hat{x}} + \frac{\partial \hat{v}}{\partial \hat{y}} + \frac{\partial \hat{w}}{\partial \hat{z}} = 0. \tag{2.5}$$

Here we have assumed that the oceanic mean velocities are zero, i.e., $u_0 = v_0 = w_0 = 0$. Equations (2.1) and (2.2) are the horizontal momentum equations, equation (2.3) is the hydrostatic equation, equation (2.4) is the density conservation equation

and equation (2.5) is the continuity equation. The variables $\hat{u}$, $\hat{v}$ and $\hat{w}$ are the perturbation velocities, $\hat{\rho}$ is the perturbation density, $\hat{p}$ is the perturbation pressure, $\hat{f}$ is the Coriolis parameter and $\rho_0(z)$ is the density of the rest ocean. By using the Boussinesq approximation, ρ_0 is treated as constant in equations (2.1) and (2.2). The carat ($\hat{}$) denotes dimensional quantities.

We adopt the following scaling [Pedlosky, 1987]:

$$\hat{x} = Lx, \hat{y} = Ly, \hat{z} = Hz, \hat{t} = Tt, \tag{2.6}$$

$$\hat{f} = f_0 + \beta_0 \hat{y} = f_0 f, f = 1 + \beta y, \beta = \frac{\beta_0 L}{f_0}, \tag{2.7}$$

$$\hat{u} = Uu, \hat{v} = Uv, \hat{w} = \frac{UH}{L} w, \hat{p} = \rho_0 f_0 LUp, \hat{\rho} = \rho_0 \frac{f_0 UL}{gH} \rho. \tag{2.8}$$

Here we choose a length scale $L = 100$ km, depth scale $H = 4.5$ km, velocity scale $U = 0.1$ m/s, coriolis parameter $f_0 = 7 \times 10^{-5}$ s^{-1}, and time scale $T = 1/f_0$. If the β effect is not considered, $f = 1$.

Substitution of the above scaling into the dimensional equations yields the following nondimensional equations:

$$\frac{\partial u}{\partial t} - fv = -\frac{\partial p}{\partial x}, \tag{2.9}$$

$$\frac{\partial v}{\partial t} + fu = -\frac{\partial p}{\partial y}, \tag{2.10}$$

$$\frac{\partial p}{\partial z} = -\rho, \tag{2.11}$$

$$\frac{\partial \rho}{\partial t} - \frac{\hat{N}^2 H^2}{f_0^2 L^2} w = 0, \tag{2.12}$$

$$\frac{\partial u}{\partial x} + \frac{\partial v}{\partial y} + \frac{\partial w}{\partial z} = 0. \tag{2.13}$$

Here the buoyancy frequency is

$$\hat{N}^2 = -\frac{g}{\rho_0}\frac{\partial \rho_0(z)}{\partial \hat{z}} = N_0^2 N^2(z), \tag{2.14}$$

where N_0 is the scale of the buoyancy frequency and $N(z)$ is a nondimensional function of z which represents the vertical structure of the buoyancy frequency.

From equations (2.11) and (2.12), by eliminating ρ, we get

$$\frac{\partial^2 p}{\partial z \partial t} = -s^2 N^2 w, \tag{2.15}$$

where we have defined

$$s = \frac{N_0 H}{f_0 L}. \tag{2.16}$$

An equation with only one dependent variable, p, can be obtained by eliminating u, v, w and ρ from equations (2.9)–(2.13). We derive the equation in terms of p because it's easy to find u, v, w and ρ once p is known and the boundary conditions are simple when p is used [Leblond and Mysak, 1978].

A single equation for p is

$$(\frac{\partial^2}{\partial t^2}+f^2)[\frac{\partial^3 p}{\partial x^2 \partial t}+\frac{\partial^3 p}{\partial y^2 \partial t}+(\frac{\partial^2}{\partial t^2}+f^2)\frac{\partial}{\partial z}(\frac{1}{s^2 N^2}\frac{\partial^2 p}{\partial z \partial t})]+\beta(f^2\frac{\partial p}{\partial x}-\frac{\partial^3 p}{\partial x^2 \partial t}-2f\frac{\partial^2 p}{\partial y \partial t}) = 0. \tag{2.17}$$

Following custom, we use the method of separation of variables to solve the above equation. We have

$$p(x,y,z,t) = \sum_{n=0}^{n=+\infty} \ddot{p}_n(x,y,z,t) = \sum_{n=0}^{n=+\infty} P_n(x,y,t)F_n(z), \tag{2.18}$$

therefore the solution is written as the sum of various vertical modes. The vertical modes are orthogonal to each other, and are called normal modes. The vertical structure of a mode is described by $F_n(z)$, while $P_n(x,y,t)$ represents the horizontal propagation of the mode, and $\ddot{p}_n(x,y,z,t)$ is the full solution for each mode.

Substitution of equation (2.18) into (2.17) gives the horizontal component

$$(\frac{\partial^2}{\partial t^2}+f^2)[\frac{\partial^3 P_n}{\partial x^2\partial t}+\frac{\partial^3 P_n}{\partial y^2\partial t}-r_n^2(\frac{\partial^2}{\partial t^2}+f^2)\frac{\partial P_n}{\partial t}]+\beta(f^2\frac{\partial P_n}{\partial x}-\frac{\partial^3 P_n}{\partial x^2\partial t}-2f\frac{\partial^2 P_n}{\partial y\partial t})=0, \tag{2.19}$$

and the vertical component

$$\frac{d}{dz}(\frac{1}{s^2N^2}\frac{dF_n}{dz})=-r_n^2F_n, \tag{2.20}$$

where r_n^2 is the separation constant.

In order to simplify equation (2.20), we define

$$G_n(z)=\frac{1}{s^2N^2}\frac{dF_n}{dz}. \tag{2.21}$$

Substitution of (2.21) into (2.20) gives

$$\frac{dG_n}{dz}=-r_n^2F_n, \tag{2.22}$$

and

$$\frac{d^2G_n}{dz^2}+r_n^2S^2N^2G_n=0. \tag{2.23}$$

If the ocean is vertically bounded, the equation (2.23) and the two vertical boundary conditions constitute an eigenvalue problem for the eigenvalue r_n and eigenfunction $G_n(z)$. For a realistic profile of $\hat{N}(\hat{z})$, we can solve it numerically. If the ocean is vertically unbounded, the solution to equation (2.23) takes the form of waves, either trapped or propagating, depending on the values of $N(z)$ and r_n [Wunsch and Stammer, 1997].

2.2 The form of $\hat{N}(\hat{z})$

Analytic solutions to the vertical equation (2.23) are available for a few forms of $\hat{N}(\hat{z})$. The simplest situation is $\hat{N}(\hat{z})$=constant. However, analytical solutions can also be obtained using the exponential profile $\hat{N}(\hat{z})=N_0e^{\hat{z}/b}=N_0e^{az}$ [Garrett and

Munk 1972], which more closely resembles actual buoyancy profiles in the ocean. In spite of the different quantitative results for $\hat{N}(\hat{z})$=constant and $\hat{N}(\hat{z}) = N_0 e^{\hat{z}/b}$, the qualitative nature of the solutions remains unchanged.

Emery et al. [1984] used the long term mean temperature and salinity profiles to investigate the geographic and seasonal distributions of buoyancy frequency. They found that there are marked meridional and zonal changes in the mean $\hat{N}$–profiles, primarily within the upper 1000m. As shown in figure 2.1 the contours of buoyancy frequency are relatively uniform within the "abyssal ocean", defined as extending from $40°S$ to $48°N$ and between depths of 1 and 4 km. The $\hat{N}(\hat{z})$ at $\hat{z} = 1000$m is about 0.004 s^{-1}. The following model for the buoyancy frequency:

$$\hat{N}(\hat{z}) = N_0 N(z), N(z) = e^{az}, N_0 = 0.04 s^{-1}, a = 11.25 \tag{2.24}$$

is a reasonable fit to the real $\hat{N}(\hat{z})$ below 1 km [Figure 2.2]. We will use this model of $\hat{N}(\hat{z})$ in our study. Although large differences exist between the model and observations above 1 km, where there are strong seasonal and geographical variations of $\hat{N}(\hat{z})$, we will use this model in our study because of its simplicity.

2.3 Vertical representation

Given the idealized exponential form for $N(z)$, we can solve equation (2.23) analytically. There are two typical types of solutions to equation (2.23): propagating waves and standing modes. The mode solutions are determined by the equation (2.23) and two vertical boundary conditions. In the standing mode representation, vertically upward and downward propagating wave components have equal amplitude and a fixed phase relation, thus forming a mode. In the propagating wave representation, the ocean is taken as vertically unbounded, the amplitudes and phases of the waves are independent and the vertical structure is approximated by WKBJ solutions [Müller et al 1978].

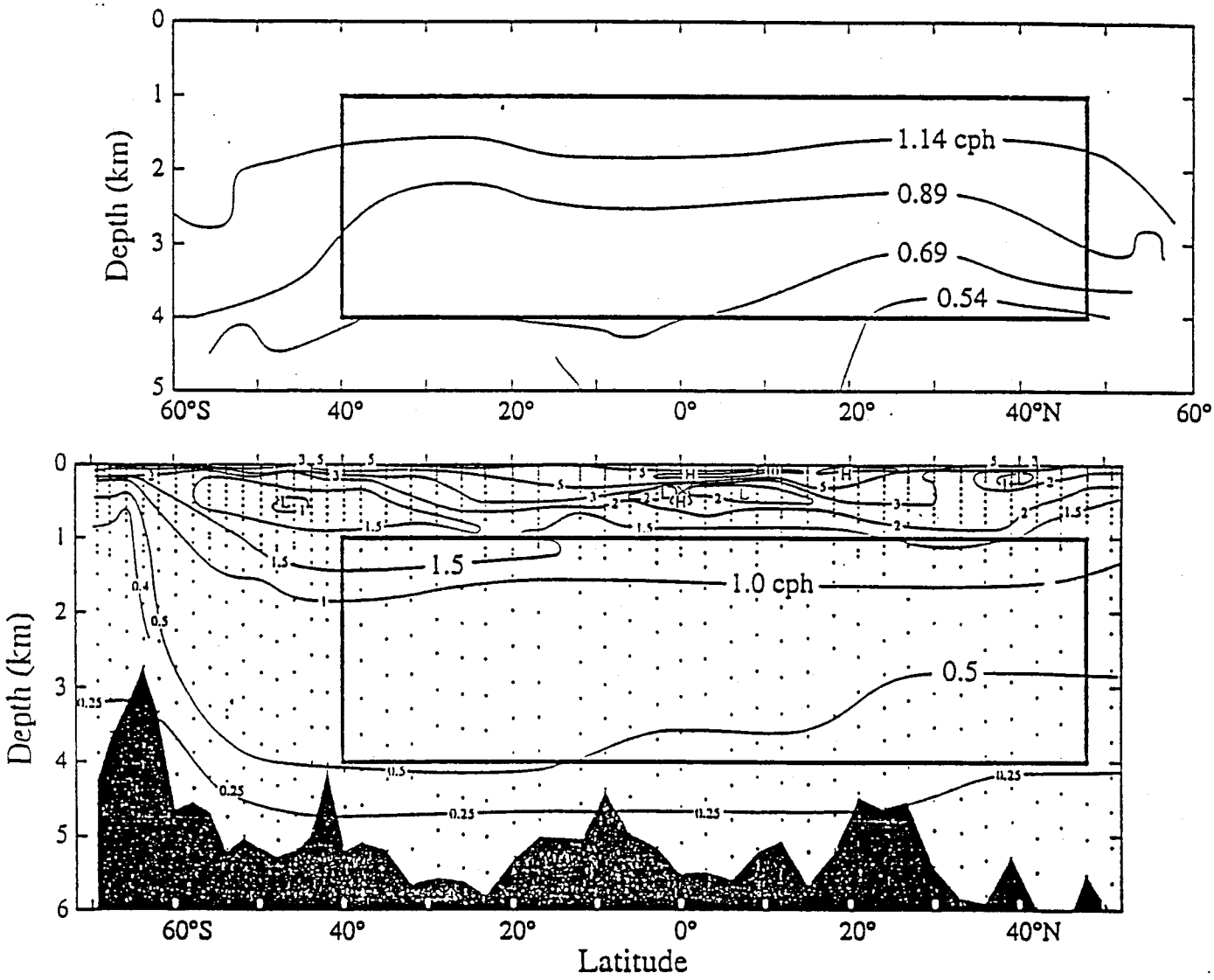

Figure 2-1: Contours of buoyancy frequency as function of latitude. TOP: global average of 10 degree squares. BOTTOM: Central Pacific (Munk and Wunsch 1997).

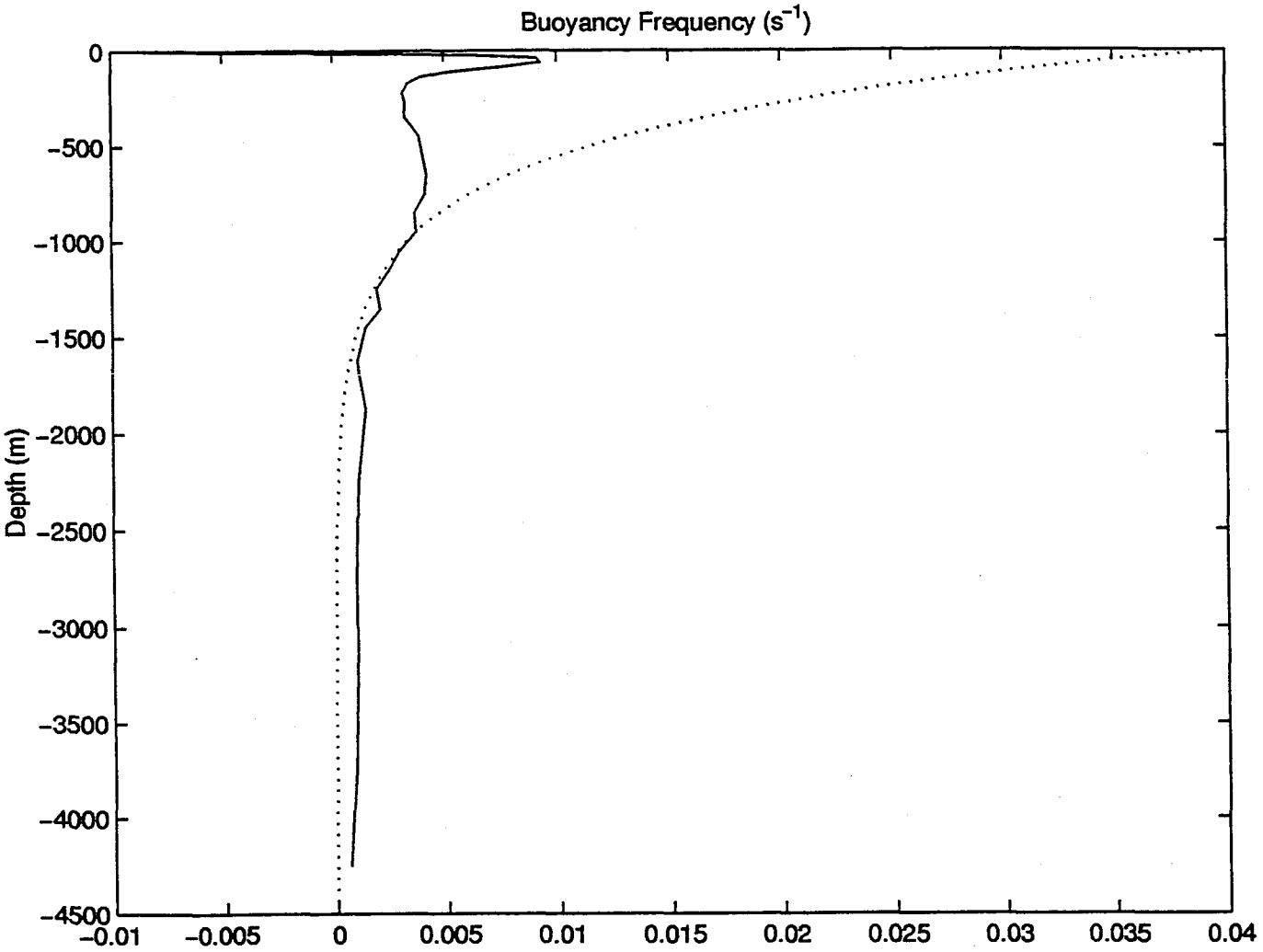

Figure 2-2: The vertical structure of buoyancy frequency. Solid line: from near 33.2°N, 21.9°W. Dashed line: for the model.

2.3.1 The WKBJ approximation

The WKBJ solution to the equation (2.23) is [Bender and Orszag, 1978]:

$$G_n(z) = \frac{C_1}{\sqrt{N}} e^{isr_n \int N dz} + \frac{C_2}{\sqrt{N}} e^{-isr_n \int N dz}. \tag{2.25}$$

The condition for the WKBJ approximation to hold is:

$$|\frac{d}{dz}\frac{1}{sr_n N}| \ll 1. \tag{2.26}$$

That is:

$$\frac{a}{sr_n} \ll 1. \tag{2.27}$$

So the WKBJ solution is better for slowly varying $N(z)$ and higher modes (larger r_n). Because the internal waves are dominated by high modes, the vertical structure is represented by propagating waves in GM spectrum.

2.3.2 The normal modes

The vertical component equation and the two boundary conditions form the eigenvalue problem, whose solutions are the modes $G_n(z)$ and eigenvalues r_n. The subscript n=0, 1, 2, ..., represents the mode number. The zeroth mode is the barotropic one.

Here we use the rigid-lid upper and lower boundary conditions:

$$\hat{w}(\hat{z}) = 0 \qquad at \qquad \hat{z} = 0 \qquad and \qquad \hat{z} = -H. \tag{2.28}$$

By using equations (2.15), (2.18) and (2.21), we can write the vertical boundary conditions in terms of $G_n(z)$:

$$G_n(z) = 0 \qquad at \qquad z = 0 \qquad and \qquad z = -1. \tag{2.29}$$

Using $N(z) = e^{az}$, the solution to equation (2.23) is

$$G_n(z) = A_n J_0(\frac{sr_n}{a}e^{az}) + B_n Y_0(\frac{sr_n}{a}e^{az}), \tag{2.30}$$

where $J_0(z)$ is the Bessel function of the first kind, of order zero and $Y_0(z)$ is the Bessel function of the second kind, of order zero.

Under the rigid-lid boundary conditions, we get the eigenvalue equation:

$$J_0(\xi_{-1})Y_0(\xi_0) - J_0(\xi_0)Y_0(\xi_{-1}) = 0, \tag{2.31}$$

where for simplicity we have defined:

$$\xi = \frac{sr_n}{a}e^{az}, \qquad \xi_0 = \frac{sr_n}{a}, \qquad \xi_{-1} = \frac{sr_n}{a}e^{-a}. \tag{2.32}$$

The corresponding eigenfunction is

$$G_n(z) = A_n[J_0(\xi) - \frac{J_0(\xi_p)}{Y_0(\xi_p)}Y_0(\xi)] = A_n\Gamma_n(z), \tag{2.33}$$

where

$$p = 0 \qquad or \qquad -1, \tag{2.34}$$

and

$$\Gamma_n(z) = J_0(\xi) - \frac{J_0(\xi_p)}{Y_0(\xi_p)}Y_0(\xi) = J_0(\frac{sr_n}{a}e^{az}) - \frac{J_0(sr_n/a)}{Y_0(sr_n/a)}Y_0(\frac{sr_n}{a}e^{az}). \tag{2.35}$$

From equation (2.22), we get

$$F_n(z) = -\frac{1}{r_n^2}\frac{dG_n}{dz} = -\frac{A_n}{r_n^2}\frac{d\Gamma_n(z)}{dz}. \tag{2.36}$$

The first four eigenvalues are listed in the following table, and the corresponding first four normal modes are shown in figure 2.3.

Mode No.	Eigenvalue	Equivalent Deformation Radius
0	0	∞
1	1.117	89.5(km)
2	2.486	40.2(km)
3	3.860	25.9(km)

Table 2.1: Eigenvalues and equivalent deformation radius

Here we overestimate the first baroclinic Rossby deformation radius. The typical first baroclinic Rossby deformation radius is about 50 km in middle latitudes. The difference is due to the fact that we used the idealized formula for $\hat{N}(\hat{z})$ and the eigenvalues of the equation (2.23) are determined by the form of $N(z)$. In the GM spectrum, because short propagating waves are assumed in the vertical direction, most of the results can be expressed in terms of the local $N(z)$ and it doesn't much matter which model of $N(z)$ is taken.

To a good first approximation, most of the baroclinic energy can be found in a form in which the thermocline simply moves up and down, the entire water column moving together [Wunsch 1981]. This dominance of the "lowest mode" is in striking contrast to the mixture of high modes required to describe the internal-wave observations [Munk 1981]. The simplest explanation of this lowest-mode character of the observations is in the tendency of quasi-geostrophic nonlinear interactions to drive the motion toward larger scales both in the vertical and horizontal [Charney 1971, Rhines 1977, Fu and Flierl, 1979]. Wunsch [1997] made a survey of the vertical structure of kinetic energy profiles in a large number of globally distributed long current records. He found that in most regions the water–column–averaged kinetic energy is dominated by the barotropic and first baroclinic modes, and because of the near-surface intensification of baroclinic modes sea surface height variability mainly reflects the first baroclinic mode, and thus the motion of the main thermocline. Therefore, barotropic models alone can't describe the sea surface height variability.

2.4 Horizontally propagating waves

Consider horizontally propagating wave solutions to equation (2.19) as

$$P_n(x,y,t) = \int\int\int \tilde{p}_n(k,l,\sigma)e^{i(kx+ly-\sigma t)}dkdld\sigma. \tag{2.37}$$

Substitution of equation (2.37) into (2.19) yields the dispersion relation:

$$\sigma(f^2-\sigma^2)[k^2+l^2+r_n^2(f^2-\sigma^2)]+\beta[(f^2-\sigma^2)k+2fl\sigma]=0. \tag{2.38}$$

The equation (2.38) is typically simpified in two limits: the high frequency limit and the low frequency limit [Gill, 1982].

(1) In the high frequency limit, i.e., $\sigma >> f$ with $\beta \to 0$, the dispersion relation equation (2.38) can be simplified as

$$k^2+l^2+r_n^2(f^2-\sigma^2)=0. \tag{2.39}$$

Because the hydrostatic approximation was made in equation (2.3) which is equivalent to the assumption that $\sigma << N$, equation (2.39) holds only for $f << \sigma << N$. The GM spectrum is focused on this frequency range.

(2) In the low frequency limit, i.e., $\sigma << f$, the dispersion relation equation can be approximated by

$$\sigma(k^2+l^2+f^2r_n^2)+\beta k=0. \tag{2.40}$$

This is the Rossby wave dispersion relation. We will restrict our attention to the low frequency limit in the following.

Substitution of equations (2.36) and (2.37) into (2.18) yields the solution for **each mode** for the pressure:

$$\ddot{p}_n(x,y,z,t) = \int\int\int[-\frac{\Upsilon(k,l,\sigma,n)}{r_n^2}\frac{d\Gamma_n(z)}{dz}]e^{i(kx+ly-\sigma t)}dkdld\sigma, \tag{2.41}$$

where we have set

$$\Upsilon(k,l,\sigma,n) = A_n \tilde{p}_n(k,l,\sigma). \tag{2.42}$$

At very low frequency, i.e., $\sigma << f$, the horizontal momentum equations (2.9) and (2.10) can be approximated by the geostrophic relations:

$$fv = \frac{\partial p}{\partial x}, \tag{2.43}$$

$$fu = -\frac{\partial p}{\partial y}. \tag{2.44}$$

Using equations (2.43), (2.44), (2.11) and (2.15), we find the wave solutions of **each mode** for the horizontal velocities, vertical velocity and density:

$$\ddot{u}_n(x,y,z,t) = \int\int\int [\frac{il\Upsilon(k,l,\sigma,n)}{fr_n^2}\frac{d\Gamma_n(z)}{dz}]e^{i(kx+ly-\sigma t)}dkdld\sigma, \tag{2.45}$$

$$\ddot{v}_n(x,y,z,t) = \int\int\int [-\frac{ik\Upsilon(k,l,\sigma,n)}{fr_n^2}\frac{d\Gamma_n(z)}{dz}]e^{i(kx+ly-\sigma t)}dkdld\sigma, \tag{2.46}$$

$$\ddot{w}_n(x,y,z,t) = \int\int\int [i\sigma\Upsilon(k,l,\sigma,n)\Gamma_n(z)]e^{i(kx+ly-\sigma t)}dkdld\sigma, \tag{2.47}$$

$$\ddot{\rho}_n(x,y,z,t) = \int\int\int [-\Upsilon(k,l,\sigma,n)s^2N^2(z)\Gamma_n(z)]e^{i(kx+ly-\sigma t)}dkdld\sigma. \tag{2.48}$$

2.5 Normalization:

In the above section, the solutions to the governing equations for low frequency oceanic motion were obtained. In order to relate the spectra of different variables, both to each other and to the total energy of each wave, we will normalize the solutions in this section.

Let $\dot{u}$, $\dot{v}$,$\dot{w}$ and $\dot{\rho}$ designate the **single wave** solution of each mode to equations (2.9)–(2.13), according to equations (2.45)–(2.48), we get:

$$\dot{u} = \frac{il\Upsilon(k,l,\sigma,n)}{fr_n^2}\frac{d\Gamma_n(z)}{dz}e^{i(kx+ly-\sigma t)}, \tag{2.49}$$

$$\dot{v} = -\frac{ik\Upsilon(k,l,\sigma,n)}{fr_n^2}\frac{d\Gamma_n(z)}{dz}e^{i(kx+ly-\sigma t)}, \tag{2.50}$$

$$\dot{w} = i\sigma\Upsilon(k,l,\sigma,n)\Gamma_n(z)e^{i(kx+ly-\sigma t)}, \tag{2.51}$$

$$\dot{\rho} = -\Upsilon(k,l,\sigma,n)s^2N^2(z)\Gamma_n(z)e^{i(kx+ly-\sigma t)}. \tag{2.52}$$

Let $\rho_0\hat{E}(k,l,\sigma,n)$ designate the dimensional total energy per unit surface area of the single wave with wavenumber k and l, frequency σ and mode number n. Then

$$\rho_0\hat{E}(k,l,\sigma,n) = \int_{-H}^{0}[\frac{\rho_0}{2}(|\hat{u}|^2 + |\hat{v}|^2) + \frac{g^2|\hat{\rho}|^2}{2\hat{N}^2\rho_0}]d\hat{z}, \tag{2.53}$$

where $\hat{u}$, $\hat{v}$ and $\hat{\rho}$ are the dimensional perturbation horizontal velocities and the dimensional perturbation density associated with the single wave, ρ_0 is the density of the rest ocean, and $\hat{N}$ is the dimensional buoyancy frequency [Gill 1982]. We have neglected the vertical kinetic energy which is much smaller than the horizontal kinetic energy for low frequency motion.

Substitution of the scaling equations (2.6) – (2.8) into (2.53) gives:

$$\rho_0\hat{E}(k,l,\sigma,n) = \frac{1}{2}\rho_0U^2H\int_{-1}^{0}[|\dot{u}|^2 + |\dot{v}|^2 + \frac{f_0^2L^2}{\hat{N}^2H^2}|\dot{\rho}|^2]dz. \tag{2.54}$$

If we let $E(k,l,\sigma,n)$ designate the corresponding nondimensional total energy of each wave, then

$$\frac{1}{2}\int_{-1}^{0}[|\dot{u}|^2 + |\dot{v}|^2 + \frac{f_0^2L^2}{\hat{N}^2H^2}|\dot{\rho}|^2]dz = E(k,l,\sigma,n), \tag{2.55}$$

and

$$\hat{E}(k,l,\sigma,n) = U^2HE(k,l,\sigma,n). \tag{2.56}$$

The normalization function $\Upsilon(k,l,\sigma,n)$ is derived from the equation (2.55). Substituting equations (2.45), (2.46), (2.48) and the idealized form of the buoyancy frequency $\hat{N} = N_0e^{az}$ into the equation (2.55) gives

$$\frac{\Upsilon^2(k,l,\sigma,n)}{2}\int_{-1}^{0}[\frac{(k^2+l^2)}{f^2r_n^4}(\frac{d\Gamma_n(z)}{dz})^2+s^2N^2(z)\Gamma_n^2(z)]dz=E(k,l,\sigma,n). \quad (2.57)$$

By using equation (2.35) and the properties of Bessel function [Abramowitz and Stegun, 1964], we get:

$$\int_{-1}^{0}(\frac{d\Gamma_n(z)}{dz})^2dz=\int_{\xi_{-1}}^{\xi_0}a\xi\Gamma_n^2(\xi)d\xi, \quad (2.58)$$

$$\int_{-1}^{0}N^2(z)\Gamma_n^2(z)dz=\int_{\xi_{-1}}^{\xi_0}\frac{a\xi}{s^2r_n^2}\Gamma_n^2(\xi)d\xi, \quad (2.59)$$

$$c=\int_{\xi_{-1}}^{\xi_0}\xi\Gamma_n^2(\xi)d\xi=\frac{2}{\pi^2}[Y_0^{-2}(\xi_0)-Y_0^{-2}(\xi_{-1})]. \quad (2.60)$$

Substitution of equations (2.58)–(2.60) into (2.57) yields

$$\frac{ac(k^2+l^2+f^2r_n^2)}{2f^2r_n^4}\Upsilon^2(k,l,\sigma,n)=E(k,l,\sigma,n). \quad (2.61)$$

The equation (2.61) yields the normalization function $\Upsilon(k,l,\sigma,n)$:

$$\Upsilon(k,l,\sigma,n)=g_a(k,l,\sigma,n)\frac{\sqrt{2}fr_n^2}{\sqrt{k^2+l^2+f^2r_n^2}}\sqrt{\frac{1}{ac}}, \quad (2.62)$$

where for simplification we have defined

$$g_a(k,l,\sigma,n)=\sqrt{E(k,l,\sigma,n)}. \quad (2.63)$$

Substitution of equation (2.62) into equations (2.45)–(2.48) yields the normalized solutions:

$$\ddot{u}_n(x,y,z,t)=\int\int\int[g_a(k,l,\sigma,n)\frac{i\sqrt{2}l}{\sqrt{k^2+l^2+f^2r_n^2}}\sqrt{\frac{1}{ac}}\frac{d\Gamma_n(z)}{dz}e^{i(kx+ly-\sigma t)}, \quad (2.64)$$

$$\ddot{v}_n(x,y,z,t) = \int\int\int [-g_a(k,l,\sigma,n)\frac{i\sqrt{2}k}{\sqrt{k^2+l^2+f^2r_n^2}}\sqrt{\frac{1}{ac}}\frac{d\Gamma_n(z)}{dz}e^{i(kx+ly-\sigma t)}, \quad (2.65)$$

$$\ddot{w}_n(x,y,z,t) = \int\int\int [g_a(k,l,\sigma,n)\frac{i\sqrt{2}fr_n\sigma}{\sqrt{k^2+l^2+f^2r_n^2}}r_n\sqrt{\frac{1}{ac}}\Gamma_n(z)e^{i(kx+ly-\sigma t)}, \quad (2.66)$$

$$\ddot{\rho}_n(x,y,z,t) = \int\int\int [-g_a(k,l,\sigma,n)\frac{\sqrt{2}fr_n}{\sqrt{k^2+l^2+f^2r_n^2}}s^2N^2(z)r_n\sqrt{\frac{1}{ac}}\Gamma_n(z)e^{i(kx+ly-\sigma t)}. \quad (2.67)$$

The above equations (2.64)–(2.67) can be simplified as :

$$\ddot{u}_n(x,y,z,t) = \int\int\int g_a(k,l,\sigma,n)u_a(k,l,\sigma,z,n)e^{i(kx+ly-\sigma t)}dkdld\sigma, \quad (2.68)$$

$$\ddot{v}_n(x,y,z,t) = \int\int\int g_a(k,l,\sigma,n)v_a(k,l,\sigma,z,n)e^{i(kx+ly-\sigma t)}dkdld\sigma, \quad (2.69)$$

$$\ddot{w}_n(x,y,z,t) = \int\int\int g_a(k,l,\sigma,n)w_a(k,l,\sigma,z,n)e^{i(kx+ly-\sigma t)}dkdld\sigma, \quad (2.70)$$

$$\ddot{\rho}_n(x,y,z,t) = \int\int\int g_a(k,l,\sigma,n)\rho_a(k,l,\sigma,z,n)e^{i(kx+ly-\sigma t)}dkdld\sigma, \quad (2.71)$$

where we have defined

$$u_a(k,l,\sigma,z,n) = \frac{i\sqrt{2}l}{\sqrt{k^2+l^2+f^2r_n^2}}P_n(z), \quad (2.72)$$

$$v_a(k,l,\sigma,z,n) = -\frac{i\sqrt{2}k}{\sqrt{k^2+l^2+f^2r_n^2}}P_n(z), \quad (2.73)$$

$$w_a(k,l,\sigma,z,n) = \frac{i\sqrt{2}fr_n\sigma}{\sqrt{k^2+l^2+f^2r_n^2}}Q_n(z), \quad (2.74)$$

$$\rho_a(k,l,\sigma,z,n) = -\frac{\sqrt{2}fr_n}{\sqrt{k^2+l^2+f^2r_n^2}}s^2N^2(z)Q_n(z), \quad (2.75)$$

and

$$P_n(z) = \sqrt{\frac{1}{ac}}\frac{d\Gamma_n(z)}{dz} = sr_ne^{az}\sqrt{\frac{1}{ac}}[\frac{J_0(\xi_p)}{Y_0(\xi_p)}Y_1(\xi) - J_1(\xi)], \quad n \geq 1, \quad (2.76)$$

$$Q_n(z) = r_n \sqrt{\frac{1}{ac}} \Gamma_n(z). \tag{2.77}$$

The eigenfunctions $P_n(z)$ and $Q_n(z)$ satisfy the orthogonal conditions

$$\int_{-1}^{0} P_m(z) P_n(z) dz = \delta_{nm}, \tag{2.78}$$

$$\int_{-1}^{0} S^2 N^2(z) Q_m(z) Q_n(z) dz = \delta_{nm}. \tag{2.79}$$

where δ_{nm} is the Kronecker delta function.

For the barotropic mode (n=0), we have

$$r_0 = 0.0, \quad P_0(z) = 1.0, \quad Q_0(z) = 0.0, \tag{2.80}$$

meaning that there is no vertical structure in the horizontal velocities and vertical velocity is zero.

The vertical eigenfunctions $P_n(z)$ and $Q_n(z)$ are plotted in figure 2.3 for n=0 to 3. An important property in figure 2.3 is the near–surface intensification of $P_n(z)$ for n=1 to 3. Equations (2.72) and (2.73) suggest that the vertical structure of the horizontal kinetic energy is proportional to $P_n^2(z)$, so that the vertical structure of baroclinic horizontal kinetic energy will correspondingly show a near–surface intensification.

2.6 The model for the temperature

To a good first approximation, the temperature variability can be attributed to the vertical advection of the mean vertical temperature profile. Thus the dimensional heat equation can be simply written as

$$\frac{\partial \hat{\theta}}{\partial \hat{t}} + \hat{w} \frac{\partial \theta_0(z)}{\partial \hat{z}} = 0. \tag{2.81}$$

where $\hat{\theta}$ is the dimensional perturbation temperature, $\hat{w}$ is the dimensional perturbation vertical velocity and $\theta_0(z)$ is the temperature of the rest state.

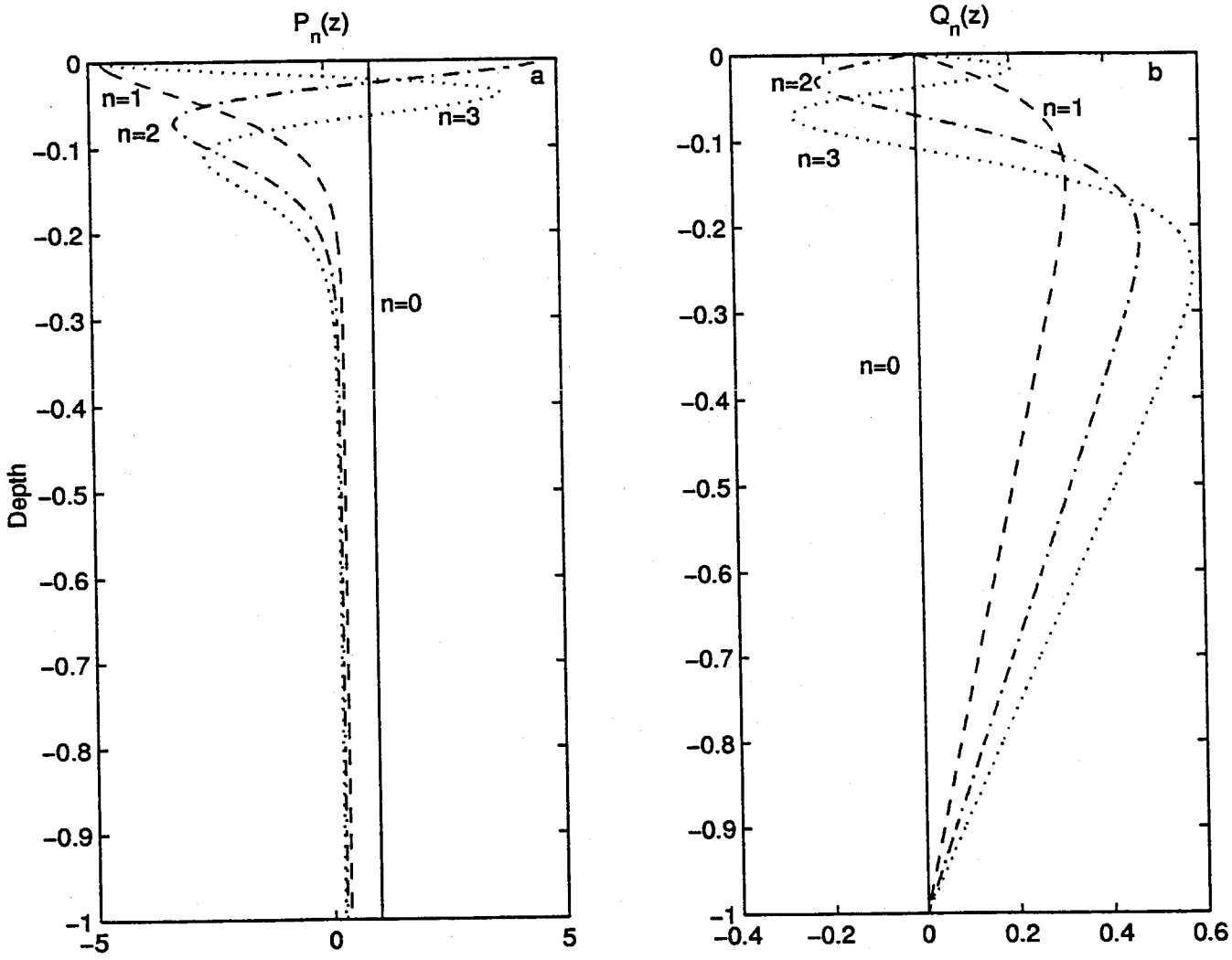

Figure 2-3: Normal modes 0 to 3 (a) Horizontal velocity (b) Vertical velocity.

The corresponding nondimensional equation is

$$\frac{\partial \theta}{\partial t} + \mu w = 0, \tag{2.82}$$

where

$$\mu = \frac{TW}{\Theta} \frac{\partial \theta_0(z)}{\partial \hat{z}}, \tag{2.83}$$

and Θ is the scale of the temperature $\hat{\theta}$. The Levitus et al. [1994] climatology is used to calculate the vertical gradient of the mean temperature at different places.

Substitution of equation (2.70) into (2.82) yields

$$\ddot{\theta}_n(x, y, z, t) = \int\int\int g_a(k, l, \sigma, n)\theta_a(k, l, \sigma, z, n)e^{i(kx+ly-\sigma t)}dkdld\sigma, \tag{2.84}$$

where

$$\theta_a(k, l, \sigma, z, n) = -\frac{\mu w_a}{\sigma}i = \frac{\sqrt{2}fr_n}{\sqrt{k^2 + l^2 + f^2 r_n^2}}\mu Q_n(z). \tag{2.85}$$

Equation (2.84) gives the solution for the temperature perturbation associated with the low frequency oceanic motion. In section 2.5, we related solutions for different variables to each other and to the total energy of each wave through the normalization process. By definition, the potential energy is associated with the density perturbation. For simplicity, we ignore variations in salt, so that density perturbations are proportional to the temperature perturbations to a first order approximation, thus the potential energy can be expressed in terms of the temperature perturbation also.

As shown in section 2.5, the potential energy per unit volume for a wave is defined as

$$\hat{P}_w = \frac{g^2|\hat{\rho}|^2}{2\hat{N}^2\rho_0} = \frac{\rho_0 U^2 f_0^2 L^2}{2\hat{N}^2 H^2} g_a^2 \rho_a^2. \tag{2.86}$$

From equations (2.12) and (2.82), we find the relation between the temperature perturbation and density perturbation

$$\rho_a = -\frac{S^2 N^2}{\mu}\theta_a. \tag{2.87}$$

Substituting equation (2.87) into (2.86), the potential energy can be expressed in terms of the temperature perturbation

$$\hat{P}_w = \frac{\rho_0 U^2}{2} \frac{S^2 N^2}{\mu^2} g_a^2 \theta_a^2. \tag{2.88}$$

Since we have normalized the total energy for each wave in section 2.5 and the potential energy is related to the temperature perturbation, the solution for temperature has been normalized, correspondingly.

2.7 Summary

In this chapter, we introduce a dynamical model for low frequency oceanic motion. Using the method of separation of variables, we separate the model equations into horizontal and vertical components. The solutions to the horizontal components are given in the form of propagating waves. The solution to the vertical component is determined by the buoyancy frequency $\hat{N}(\hat{z})$. An idealized exponential form for $\hat{N}(\hat{z})$ is assumed, the corresponding solution to the vertical component is given in the form of standing modes. The solution is normalized so that spectra of different variables can be related, both to each other and to the total energy of each wave.

The solution to the model equations can be summarized as:

$$u(x,y,z,t) = \sum_{n=0}^{n=+\infty} \ddot{u}_n(x,y,z,t) = \sum_{n=0}^{n=+\infty} \int\int\int g_a(k,l,\sigma,n) u_a(k,l,\sigma,z,n) e^{i(kx+ly-\sigma t)} dk dl d\sigma, \tag{2.89}$$

$$v(x,y,z,t) = \sum_{n=0}^{n=+\infty} \ddot{v}_n(x,y,z,t) = \sum_{n=0}^{n=+\infty} \int\int\int g_a(k,l,\sigma,n) v_a(k,l,\sigma,z,n) e^{i(kx+ly-\sigma t)} dk dl d\sigma, \tag{2.90}$$

$$w(x,y,z,t) = \sum_{n=0}^{n=+\infty} \ddot{w}_n(x,y,z,t) = \sum_{n=0}^{n=+\infty} \int\int\int g_a(k,l,\sigma,n) w_a(k,l,\sigma,z,n) e^{i(kx+ly-\sigma t)} dk dl d\sigma, \tag{2.91}$$

$$\rho(x,y,z,t) = \sum_{n=0}^{n=+\infty} \ddot{\rho}_n(x,y,z,t) = \sum_{n=0}^{n=+\infty} \int\int\int g_a(k,l,\sigma,n) \rho_a(k,l,\sigma,z,n) e^{i(kx+ly-\sigma t)} dk dl d\sigma, \tag{2.92}$$

$$\theta(x,y,z,t) = \sum_{n=0}^{n=+\infty} \ddot{\theta}_n(x,y,z,t) = \sum_{n=0}^{n=+\infty} \int\int\int g_a(k,l,\sigma,n)\theta_a(k,l,\sigma,z,n)e^{i(kx+ly-\sigma t)}dkdld\sigma, \tag{2.93}$$

where $\ddot{u}_n(x,y,z,t)$, $\ddot{v}_n(x,y,z,t)$, $\ddot{w}_n(x,y,z,t)$, $\ddot{\rho}_n(x,y,z,t)$ and $\ddot{\theta}_n(x,y,z,t)$ are the solutions for each mode. The characteristic amplititude factors $u_a(k,l,\sigma,z,n)$, $v_a(k,l,\sigma,z,n)$, $w_a(k,l,\sigma,z,n)$, $\rho_a(k,l,\sigma,z,n)$ and $\theta_a(k,l,\sigma,z,n)$ are defined in equations (2.72)–(2.75) and (2.85), and $g_a(k,l,\sigma,n)$ is a common random factor which is related to the total energy of each wave and hasn't been specified so far.

Chapter 3

Spectra and coherence of the model

In chapter 2, we derived the solutions to the model equations. In this chapter, we will obtain the model frequency and wavenumber spectra of kinetic energy and temperature for each mode based on the solutions obtained in chapter 2. We will also obtain the frequency spectrum for the range–averaged temperature from tomographic data. The frequency and horizontal wavenumber spectra we will derive in this chapter are for **each mode**. In chapter 5, we will compare the model spectrum with the corresponding observation by adding up the contributions from the first few important modes.

3.1 Covariance

In this section, we will derive the covariance of the normalized solutions obtained in chapter 2, from which various model spectra can be found.

Let $h(x, y, z, t, n)$ represent the normalized solution to the model equations (2.9)–(2.13) for each mode, where $h(x, y, z, t, n)$ could be any of the following variables $\ddot{u}_n(x, y, z, t)$, $\ddot{v}_n(x, y, z, t)$, $\ddot{w}_n(x, y, z, t)$, $\ddot{\rho}_n(x, y, z, t)$ or $\ddot{\theta}_n(x, y, z, t)$. According to the

normalized solutions for each mode (2.68)–(2.71), $h(x,y,z,t,n)$ can be written as

$$h(x,y,z,t,n) = \int\int\int g_a(k^{'},l^{'},\sigma^{'},n)h_a(k^{'},l^{'},\sigma^{'},z,n)e^{i(k^{'}x+l^{'}y-\sigma^{'}t)}dk^{'}dl^{'}d\sigma^{'}, \quad (3.1)$$

where $g_a(k^{'},l^{'},\sigma^{'},n)$ is a common random factor of the normalized solutions $\ddot{u}_n(x,y,z,t)$, $\ddot{v}_n(x,y,z,t)$, $\ddot{w}_n(x,y,z,t)$, $\ddot{\rho}_n(x,y,z,t)$ and $\ddot{\theta}_n(x,y,z,t)$. If $h(x,y,z,t,n)$ represents $\ddot{u}_n(x,y,z,t)$, $h_a(k^{'},l^{'},\sigma^{'},z,n)$ represents the deterministic amplitude factor, $u_a(k^{'},l^{'},\sigma^{'},z,n)$, and so forth.

Taking a shift of r_x in x, r_y in y and τ in t, the above equation (3.1) yields

$$h(x+r_x,y+r_y,z,t+\tau,n) = \int\int\int g_a(k,l,\sigma,n)h_a(k,l,\sigma,z,n)e^{i[k(x+r_x)+l(y+r_y)-\sigma(t+\tau)]}dkdld\sigma, \quad (3.2)$$

and

$$h^*(x+r_x,y+r_y,z,t+\tau,n) = \int\int\int g_a^*(k,l,\sigma,n)h_a^*(k,l,\sigma,z,n)e^{-i[k(x+r_x)+l(y+r_y)-\sigma(t+\tau)]}dkdld\sigma, \quad (3.3)$$

where * denotes the complex conjugate.

By definition, the covariance function of $h(x,y,z,t,n)$ is

$$R(x,y,z,t,r_x,r_y,\tau,n) =< h(x,y,z,t,n)h^*(x+r_x,y+r_y,z,t+\tau,n) >, \quad (3.4)$$

where the brackets denote a hypothetical ensemble average.

Substitution of equations (3.1) and (3.3) into the equation (3.4) gives

$$R(x,y,z,t,r_x,r_y,\tau,n) = \int\int\int\int\int\int < g_a(k^{'},l^{'},\sigma^{'},n)g_a^*(k,l,\sigma,n) >$$
$$h_a(k^{'},l^{'},\sigma^{'},z,n)h_a^*(k,l,\sigma,z,n)e^{i[(k^{'}-k)x+(l^{'}-l)y-(\sigma^{'}-\sigma)t]}e^{-i(kr_x+lr_y-\sigma\tau)}dk^{'}dl^{'}d\sigma^{'}dkdld\sigma \quad (3.5)$$

If the oceanic process is considered to be both **homogeneous** in horizontal space and **stationary** in time, then the covariance $R(x,y,z,t,r_x,r_y,\tau,n)$ will be independent of the spatial base point x and y and temporal base point t and be a function only

of the horizontal space lag r_x and r_y, time lag τ, depth z and mode number n. Because the function $h_a(k,l,\sigma,z,n)$ has been specified, in order for the right–hand side of equation (3.5) to be independent of x, y and t, the product $< g_a(k^{'},l^{'},\sigma^{'},n)g_a^*(k,l,\sigma,n) >$ in the right–hand side of equation (3.5) must be in the form of Dirac delta functions with the only contribution to the integral occurring at $k^{'}=k$, $l^{'}=l$ and $\sigma^{'}=\sigma$.

So for the homogeneous and stationary process, we have the orthogonality relations,

$$< g_a(k^{'},l^{'},\sigma^{'},n)g_a^*(k,l,\sigma,n) >= \delta(k^{'}-k)\delta(l^{'}-l)\delta(\sigma^{'}-\sigma) < |g_a(k,l,\sigma,n)|^2 > . \quad (3.6)$$

Define the energy density spectrum as

$$\Psi(k,l,\sigma,n) =< |g_a(k,l,\sigma,n)|^2 > . \quad (3.7)$$

Substitution of equation (2.63) into (3.7) yields the relationship between the energy density spectrum and the energy of a single wave

$$\Psi(k,l,\sigma,n) =< E(k,l,\sigma,n) >, \quad (3.8)$$

meaning that the energy density spectrum $\Psi(k,l,\sigma,n)$, which is characteristic of the random process as a whole, equals to the average of the energy distribution of the individual realization $E(k,l,\sigma,n)$.

Substitution of equations (3.6) and (3.7) into (3.5) yields the covariance function of each mode for the homogeneous and stationary process

$$R(r_x,r_y,\tau,z,n) = \int\int\int h_a(k,l,\sigma,z,n)h_a^*(k,l,\sigma,z,n)\Psi(k,l,\sigma,n)e^{-i(kr_x+lr_y-\sigma\tau)}dkdld\sigma. \quad (3.9)$$

Various spectra will be derived in next sections from this covariance function. In the following, we will find the relationship between the total energy per unit surface

area of each mode and the energy density $\Psi(k,l,\sigma,n)$.

If $r_x = r_y = \tau = 0$, the covariance function (3.9) becomes simply the mean-square quantity of each mode

$$R(0,0,0,z,n) =< |h(x,y,z,t,n|^2 >= \int\int\int h_a(k,l,\sigma,z,n)h_a^*(k,l,\sigma,z,n)\Psi(k,l,\sigma,n)dkdld\sigma. \tag{3.10}$$

Substitution of $\ddot{u}$, $\ddot{v}$, $\ddot{\rho}$ and $\ddot{\theta}$ for h into the above equation gives the mean-square quantities of $\ddot{u}$, $\ddot{v}$, $\ddot{\rho}$ and $\ddot{\theta}$ for each mode

$$[< |\ddot{u}|^2 >, < |\ddot{v}|^2 >, < |\ddot{\rho}|^2 >, < |\ddot{\theta}|^2 >] = \int\int\int [|u_a|^2, |v_a|^2, |\rho_a|^2, |\theta_a|^2]\Psi(k,l,\sigma,n)dkdld\sigma. \tag{3.11}$$

Let $\rho_0\hat{E}_n$ designate the dimensional total energy per unit surface area for each mode, so that

$$\begin{aligned}\rho_0\hat{E}_n &= \int_{-H}^{0} \frac{\rho_0}{2}[< |\ddot{\hat{u}}|^2 > + < |\ddot{\hat{v}}|^2 > + \frac{g^2 < |\ddot{\hat{\rho}}|^2 >}{2\hat{N}^2\rho_0}]d\hat{z} \\ &= \rho_0 U^2 H \int_{-1}^{0} \frac{1}{2}[< |\ddot{u}|^2 > + < |\ddot{v}|^2 > + \frac{f_0^2 L^2}{\hat{N}^2 H^2} < |\ddot{\rho}|^2 >]dz. \end{aligned} \tag{3.12}$$

Substitution of equation (3.11) into equation (3.12) yields

$$\hat{E}_n = U^2 H \int\int\int [\frac{1}{2}\int_{-1}^{0}(|u_a|^2 + |v_a|^2 + \frac{f_0^2 L^2}{\hat{N}^2 H^2}|\rho_a|^2)dz]\Psi(k,l,\sigma,n)dkdld\sigma. \tag{3.13}$$

Substitution of equations (2.72), (2.73) and (2.75) into equation (3.13) gives

$$\hat{E}_n = U^2 H \int\int\int \Psi(k,l,\sigma,n)dkdld\sigma. \tag{3.14}$$

Define E_n as the corresponding dimensionless total energy for each mode, then

$$\hat{E}_n = U^2 H E_n, \tag{3.15}$$

and

$$E_n = \int\int\int \Psi(k,l,\sigma,n)dkdld\sigma. \tag{3.16}$$

It is relation (3.16) that gives validity to the interpretation of $\Psi(k,l,\sigma,n)$ as an energy density for each mode.

For horizontal isotropy, we may introduce the two-dimensional energy density for each mode

$$\Phi(K,\sigma,n) = \int_{-\pi}^{\pi} \Psi(k,l,\sigma,n)Kd\phi = 2\pi K\Psi(k,l,\sigma,n) \tag{3.17}$$

where $K = \sqrt{k^2+l^2}$ is the horizontal wavenumber amplitude.

Now the dimensionless total energy per unit surface area of each mode can be written as

$$E_n = \int_{-\infty}^{+\infty}\int_{-\infty}^{+\infty} \Phi(K,\sigma,n)dKd\sigma \tag{3.18}$$

3.2 Spectra and coherence

Propagating signals have spatial as well as temporal spectra. Data at a fixed spatial point can yield a frequency spectra, whereas data along a certain spatial line at a fixed time can yield a wavenumber spectrum. In the following, we will derive the model frequency and wavenumber spectra of each mode for kinetic energy and temperature and we will see that various spectra are related to each other through the energy density spectrum $\Psi(k,l,\sigma,n)$. The corresponding observational frequency and wavenumber spectra of temperature and kinetic energy will be described in chapter 4. Then, in chapter 5 we will find out if we can find a universal form of $\Psi(k,l,\sigma,n)$ so that each model spectrum can fit the corresponding observation.

3.2.1 Frequency spectra

In (3.9) let the horizontal space lags $r_x = 0$ and $r_y = 0$, i.e., we consider the time series data at a fixed spatial point. Then covariance function (3.9) reduces to a one

dimesional temporal autocovariance function

$$R(\tau, z, n) = \int\int\int h_a h_a^* \Psi(k, l, \sigma, n) e^{i\sigma\tau} dk dl d\sigma. \tag{3.19}$$

By definition, we can find the frequency spectra of each mode from (3.19):

$$F(\omega, n, z) = \frac{1}{2\pi} \int_{-\infty}^{+\infty} R(\tau, z, n) e^{-i\omega\tau} d\tau = \int_k \int_l h_a h_a^* \Psi(k, l, \omega, n) dk dl. \tag{3.20}$$

Here we have used the following fundamental Fourier identity

$$\int_{-\infty}^{+\infty} e^{i(\omega-\sigma)\tau} d\tau = 2\pi\delta(\omega - \sigma). \tag{3.21}$$

Substitution of u_a, v_a, ρ_a and θ_a for h_a into equation (3.20) gives the frequency spectrum of $\ddot{u}$, $\ddot{v}$, $\ddot{\rho}$, and $\ddot{\theta}$ for each mode:

$$F_{u,v,\rho,\theta}(\omega, n, z) = \int_k \int_l [|u_a|^2, |v_a|^2, |\rho_a|^2, |\theta_a|^2] \Psi(k, l, \omega, n) dk dl. \tag{3.22}$$

Therefore, the nondimensional kinetic energy frequency spectrum for each mode is

$$F_k(\omega, n, z) = \frac{1}{2} \int_k \int_l (|u_a|^2 + |v_a|^2) \Psi(k, l, \omega, n) dk dl = \frac{1}{2} \int_K (|u_a|^2 + |v_a|^2) \Phi(K, \omega, n) dK, \tag{3.23}$$

and the nondimensional total kinetic energy for each mode at depth z is

$$E_k(n, z) = \int F_k(\omega, n, z) d\omega = \frac{1}{2} \int\int (|u_a|^2 + |v_a|^2) \Phi(K, \omega, n) dK d\omega. \tag{3.24}$$

We can get the total kinetic energy per unit surface area for each mode from the above equation (3.24)

$$K_h(n) = \int_{-1}^{0} E_k(n, z) dz = \frac{1}{2} \int\int\int (|u_a|^2 + |v_a|^2) \Phi(K, \omega, n) dK d\omega dz. \tag{3.25}$$

For horizontal isotropy, the temperature frequency spectrum in equation (3.22)

can be simplified as

$$F_\theta(\omega, n, z) = \int_K |\theta_a|^2 \Phi(K, \omega, n) dK. \tag{3.26}$$

3.2.2 Horizontal wavenumber spectra

If we let $\tau = 0$ in (3.9), i.e., we shall consider only instantaneous pictures of the oceanic variability in a horizontal plane. Then the covariance function reduces to

$$R(r_x, r_y, z, n) = \int\int\int h_a h_a^* \Psi(k, l, \sigma, n) e^{-i(kr_x + lr_y)} dk dl d\sigma. \tag{3.27}$$

From equation (3.27), we get the two dimensional spectra of $\ddot{u}$, $\ddot{v}$, $\ddot{\rho}$ and $\ddot{\theta}$ for each mode

$$F_{u,v,\rho,\theta}(k, l, z, n) = \int_\omega [|u_a|^2, |v_a|^2, |\rho_a|^2, |\theta_a|^2] \Psi(k, l, \omega, n) d\omega, \tag{3.28}$$

Therefore, the two dimensional kinetic energy wavenumber spectrum for each mode is

$$F_k(k, l, z, n) = \frac{1}{2} \int_{-\infty}^{+\infty} (|u_a|^2 + |v_a|^2) \Psi(k, l, \omega, n) d\omega. \tag{3.29}$$

Studies of two dimensional spectrum of ocean waves are very important in determining the directions of the wave motions and in clarifying the fundamental process of wave generation. However, in contrast to a great many studies of the one dimensional spectrum, few attempts have been made to study the two dimensional spectrum of ocean waves. Wunsch and Hendry [1972] analyzed the two dimensional velocity wavenumber spectra to determine both the directions and the wavelengths of internal waves. Richman [1976] studied the two dimensional temperature wavenumber spectrum of low frequency variability. However, the data he used were too short to assess the isotropy of the temperature field.

To put it simply, we first try to reduce the two dimensional problem into a one dimensional one by trying to see how the kinetic energy and potential energy depend on the total horizontal wavenumber. Eventually we will study how they depend on k

and l.

For horizontal isotropy, we may introduce the one dimensional kinetic energy wavenumber spectrum $F_k(K,n,z)$, so that

$$E_k(n,z) = \int_k \int_l F_k(k,l,n,z)dkdl = \int_K F_k(K,n,z)dK \tag{3.30}$$

Substitution of (3.29) into (3.30) yields the kinetic energy wavenumber spectrum

$$F_k(K,n,z) = \frac{1}{2}\int_{-\infty}^{+\infty}(|u_a|^2 + |v_a|^2)\Phi(K,\omega,n)d\omega. \tag{3.31}$$

The corresponding wavenumber spectrum for temperature is

$$F_\theta(K,n,z) = \int |\theta_a|^2\Phi(K,\omega,n)d\omega. \tag{3.32}$$

3.2.3 Horizontal coherence

For two points at the same depth separated horizontally by a vector:

$$\vec{R} = \vec{X}_j - \vec{X}_i = (r_x, r_y), \tag{3.33}$$

the cross spectrum of the variable $h(x,y,z,t,n)$ at these two points is

$$C_{ij}(\omega,z,n) = \int_k \int_l h_a h_a^* \Psi(k,l,\omega,n)e^{-i(kr_x+lr_y)}dkdl, \tag{3.34}$$

from which we obtain the coherence of the variable $h(x,y,z,t,n)$ at these two points:

$$R_{ij}(\omega,z,n) = \frac{C_{ij}}{\sqrt{C_{ii}C_{jj}}} = \frac{\int_k\int_l h_a h_a^*\Psi(k,l,\omega,n)e^{-i(kr_x+lr_y)}dkdl}{\int_k\int_l h_a h_a^*\Psi(k,l,\omega,n)dkdl}. \tag{3.35}$$

Substitution of u_a, v_a and θ_a for h_a in the above equation yields the coherence of $\ddot{u}$, $\ddot{v}$ and $\ddot{\theta}$ for each mode at these two points.

3.3 The frequency spectrum and coherence of the acoustic tomographic data

A key attribute of tomographic measurements is that they are spatially integrating. The ability of forming horizontal averages over large ranges is an attractive tool. The integration suppresses small scales and the suppressed scales are dependent on the length of acoustic path. Transmissions over a few hundred kilometers subdue the internal wave "noise" and transmissions over a few thousand kilometers subdue the mesoscale noise [Munk et al. 1995]. In this section, we will show analytically that the integration has the same effect as a low-pass filter, which will filter out the energy at large wavenumbers. The filtering effect depends on the length of the acoustic ray path.

Suppose two acoustic ray paths AB and CD are parallel and both are in the direction of the x-axis [Figure 3.1]. The lengths of the paths AB and CD are L_1 and L_2, respectively, and AB and CD are separated by a distance Y in the y direction. Assume d_1 and d_2 represent the range-averaged temperature along the paths AB and CD for each mode:

$$d_1(L_1, y, z, t, n) = \frac{1}{L_1}\int_A^B \ddot{\theta}_1(x, y, z, t, n)dx \tag{3.36}$$

$$d_2(L_2, y^{'}, z, t, n) = \frac{1}{L_2}\int_C^D \ddot{\theta}_2(x^{'}, y^{'}, z, t, n)dx^{'}. \tag{3.37}$$

In the following, we will derive the frequency spectrum and coherence of the range–averaged temperature of each mode.

3.3.1 Tomographic frequency spectrum

By definition, the covariance of d_1 and d_2 for each mode is

$$R_{d12}(\tau, z, n) =< d_1(L_1, y, z, t, n)d_2^*(L_2, y^{'}, z, t+\tau, n) > . \tag{3.38}$$

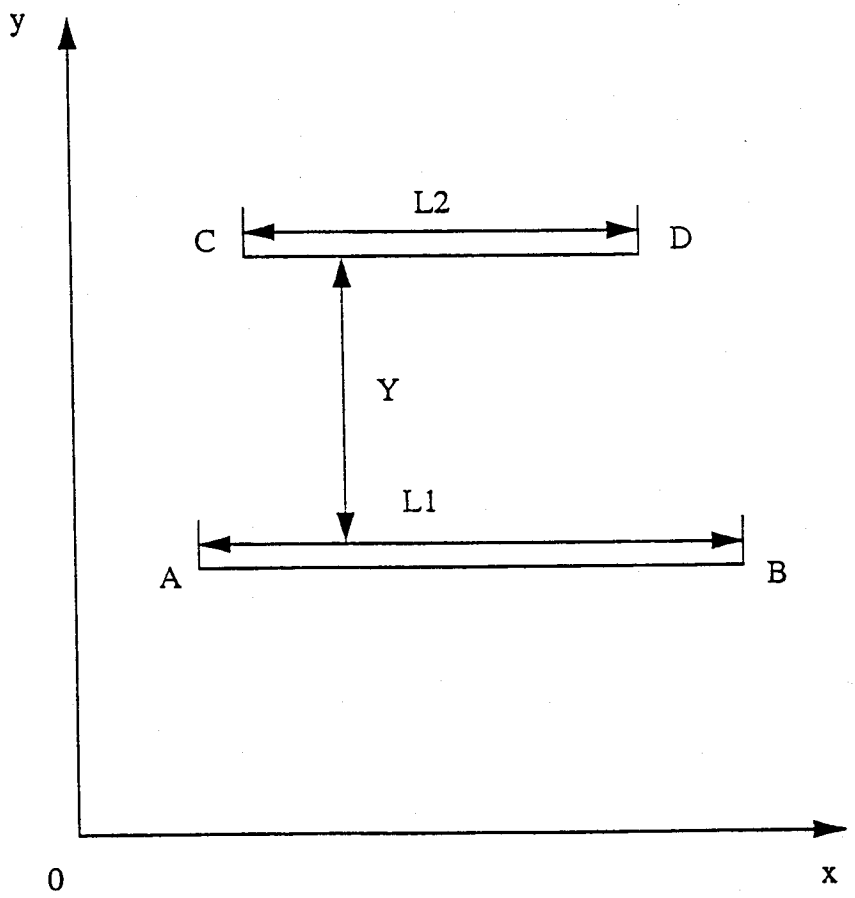

Figure 3-1: Sketch of the ray paths AB and CD.

We can relate the covariance of d_1 and d_2 to that of $\ddot{\theta}_1$ and $\ddot{\theta}_2$ by substituting equations (3.36) and (3.37) into (3.38):

$$R_{d12}(\tau, z, n) = \frac{1}{L_1 L_2} \int_A^B \int_C^D < \ddot{\theta}_1(x, y, z, t, n) \ddot{\theta}_2^*(x', y', z, t+\tau, n) > dx dx'. \quad (3.39)$$

Recalling from section 3.1 that the covariance of $\ddot{\theta}_1$ and $\ddot{\theta}_2$ for each mode is

$$\begin{aligned} R_{\theta 12}(\tau, z, n) &=< \ddot{\theta}_1(x, y, z, t, n) \ddot{\theta}_2^*(x', y', z, t+\tau, n) > \\ &= \int\int\int \theta_a \theta_a^* \Psi(k, l, \sigma, n) e^{-i[k(x'-x)+l(y'-y)-\sigma\tau]} dk dl d\sigma. \end{aligned} \quad (3.40)$$

Substitution of equation (3.40) into (3.39) gives

$$R_{d12}(\tau, z, n) = \frac{1}{L_1 L_2} \int_A^B \int_C^D [\int\int\int \theta_a \theta_a^* \Psi(k, l, \sigma, n) e^{-i[k(x'-x)+l(y'-y)-\sigma\tau]} dk dl d\sigma] dx dx'. \quad (3.41)$$

Changing the sequence of the integration, we find

$$R_{d12}(\tau, z, n) = \int_k \int_l \int_\sigma \theta_a \theta_a^* \Psi(k, l, \sigma, n) e^{-i[l(y'-y)-\sigma\tau]} [\frac{1}{L_1 L_2} \int_A^B \int_C^D e^{-ik(x'-x)} dx dx'] dk dl d\sigma. \quad (3.42)$$

If the path AB and CD are coincident, then $L_1 = L_2 = L_a$, $y' = y$ and the covariance function (3.42) reduces to the autocovariance

$$R_d(\tau, z, n) = \int_k \int_l \int_\sigma \theta_a \theta_a^* \Psi(k, l, \sigma, n) e^{i\sigma\tau} [\int_A^B \int_A^B \frac{e^{-ik(x'-x)}}{L_a^2} dx dx'] dk dl d\sigma. \quad (3.43)$$

If we define the effect due to spatial averaging as

$$W(k, L_a) = \frac{1}{L_a^2} \int_A^B \int_A^B e^{-ik(x'-x)} dx dx' = \frac{sin^2(kL_a/2)}{(kL_a/2)^2}, \quad (3.44)$$

then the equation (3.43) can be written as

$$R_d(\tau, z, n) = \int_k \int_l \int_\sigma \theta_a \theta_a^* \Psi(k, l, \sigma, n) W(k, L_a) e^{-i\sigma\tau} dk dl. \quad (3.45)$$

Finally, from the autocovariance function (3.45), we obtain the tomographic frequency spectrum of each mode

$$F_d(\omega, z, n) = \int_k \int_l \theta_a \theta_a^* \Psi(k, l, \omega, n) W(k, L_a) dk dl. \tag{3.46}$$

Recall that the temperature frequency spectrum of each mode for point measurements is given by equation (3.22). Comparing the frequency spectra of tomographic data, equation (3.46), with the frequency spectra of point measurements, equation (3.22), we note that there is an additional factor (3.44) in the spectrum of the range-averaged data. The additional factor $W(k, L_a)$ is due to the spatial average.

The function $W(k, L_a)$ has the following properties [Figure 3.2]:

(1) It filters out the high wavenumber components along the acoustic ray path. The function $|W(k, L_a)| \leq 1$ and obtains its maximum of 1 at $k = 0$. For a fixed ray path length L_a, as $|k|$ increases, $W(k, L_a)$ first drops very rapidly to zero, then oscillates with decaying amplitude.

(2) The passband width of the filter depends only on the length of the ray path. The longer the acoustic ray path, the more rapidly $W(k, L_a)$ decays. This implies that longer acoustic ray paths can filter out more small scale motions. So the longer the acoustic ray path, the smaller the energy level of the range-averaged spectra.

(3) We will see in the next chapter that most of the potential energy is distributed at smaller wavenumbers, so that the effect of filtering due to the spatial average is very small, even negligible.

(4) The frequency spectral shape of the tomographic data is the same as that of point measurements, the only difference between them is the energy level.

3.3.2 Tomographic coherence

Let the pathes AB and CD be parallel, both in the direction of the x-axis with $x_A = x_C, x_B = x_D$. Both lengths of AB and CD are L_a, and AB and CD are separated by a distance Y in the y direction [Figure 3.3]. Under the above conditions,

the cross-covariance equation (3.42) becomes

$$R_{d12}(\tau, z, n) = \int_k \int_l \int_\sigma \theta_a \theta_a^* \Psi(k, l, \sigma, n) \frac{sin^2(kL_a/2)}{(kL_a/2)^2} e^{-i(lY - \sigma\tau)} dk dl d\sigma. \tag{3.47}$$

The corresponding cross spectrum between the range–averaged temperature along the path AB and the range–averaged temperature along the path CD is

$$C_{d12}(\omega, z, n) = \int_k \int_l \theta_a \theta_a^* \Psi(k, l, \omega, n) \frac{sin^2(kL_a/2)}{(kL_a/2)^2} e^{-ilY} dk dl, \tag{3.48}$$

then the coherence function is

$$R_{d12}(\omega, z, n) = \frac{\int_k \int_l \theta_a \theta_a^* \Psi(k, l, \omega, n) W(k, L_a) e^{-ilY} dk dl}{\int_k \int_l \theta_a \theta_a^* \Psi(k, l, \omega, n) W(k, L_a) dk dl}, \tag{3.49}$$

where

$$W(k, L_a) = \frac{sin^2(kL_a/2)}{(kL_a/2)^2}. \tag{3.50}$$

3.4 Summary

Under the assumption of statistical spatial homogeneity, temporal stationarity and isotropy, we have derived the following relations for **each mode**:

(1) the nondimensional kinetic energy frequency spectrum

$$F_k(\omega, n, z) = P_n^2(z) \int_0^{+\infty} \frac{K^2}{K^2 + f^2 r_n^2} \Phi(K, \omega, n) dK, \tag{3.51}$$

(2) the nondimensional kinetic energy wavenumber spectrum

$$F_k(K, n, z) = P_n^2(z) \int_{-\infty}^{+\infty} \frac{K^2}{K^2 + f^2 r_n^2} \Phi(K, \omega, n) d\omega, \tag{3.52}$$

(3) the nondimensional temperature frequency spectrum

$$F_\theta(\omega, n, z) = \mu^2 Q_n^2(z) \int_0^{+\infty} \frac{2 f^2 r_n^2}{K^2 + f^2 r_n^2} \Phi(K, \omega, n) dK, \tag{3.53}$$

(4) the nondimensional temperature wavenumber spectrum

$$F_\theta(K,n,z) = \mu^2 Q_n^2(z) \int_{-\infty}^{+\infty} \frac{2f^2 r_n^2}{K^2 + f^2 r_n^2} \Phi(K,\omega,n) d\omega. \tag{3.54}$$

(5) the nondimensional frequency spectrum for range–averaged temperature (tomography)

$$\begin{aligned} F_d(\omega,n,z) &= \mu^2 Q_n^2(z) \int_{-\infty}^{+\infty} \int_{-\infty}^{+\infty} \frac{2f^2 r_n^2}{K^2 + f^2 r_n^2} \Psi(k,l,\omega,n) W(k,L_a) dk dl \\ &= \mu^2 Q_n^2(z) \int_{-\infty}^{+\infty} \int_{-\infty}^{+\infty} \frac{2f^2 r_n^2}{(K^2 + f^2 r_n^2)} \frac{\Phi(K,\omega,n)}{2\pi K} W(k,L_a) dk dl, \end{aligned} \tag{3.55}$$

(6) the nondimensional kinetic energy at an arbitrary depth z

$$E_k(n,z) = P_n^2(z) \int_{-\infty}^{+\infty} \int_0^{+\infty} \frac{K^2}{K^2 + f^2 r_n^2} \Phi(K,\omega,n) dK d\omega, \tag{3.56}$$

(7) the nondimensional total kinetic energy per unit surface area

$$K_h(n) = \int_{-1}^{0} E_k(n,z) dz = \int_{-\infty}^{+\infty} \int_0^{+\infty} \frac{K^2}{K^2 + f^2 r_n^2} \Phi(K,\omega,n) dK d\omega, \tag{3.57}$$

where $P_n(z)$, $Q_n(z)$, μ and $W(k,L_a)$ are defined in (2.76), (2.77), (2.83) and (3.44), respectively.

From equation (3.51) to (3.57), we note that the wavenumber and frequency spectra of kinetic energy and temperature, the frequency spectra of range–averaged temperature and the kinetic energy are related to each other through the energy density $\Phi(K,\omega,n)$.

In the following chapters, we will review the observed spectral properties of low frequency oceanic variability and we will see whether we can find a universal form of the energy density $\Phi(K,\omega,n)$ so that all the model spectra can fit the corresponding observations.

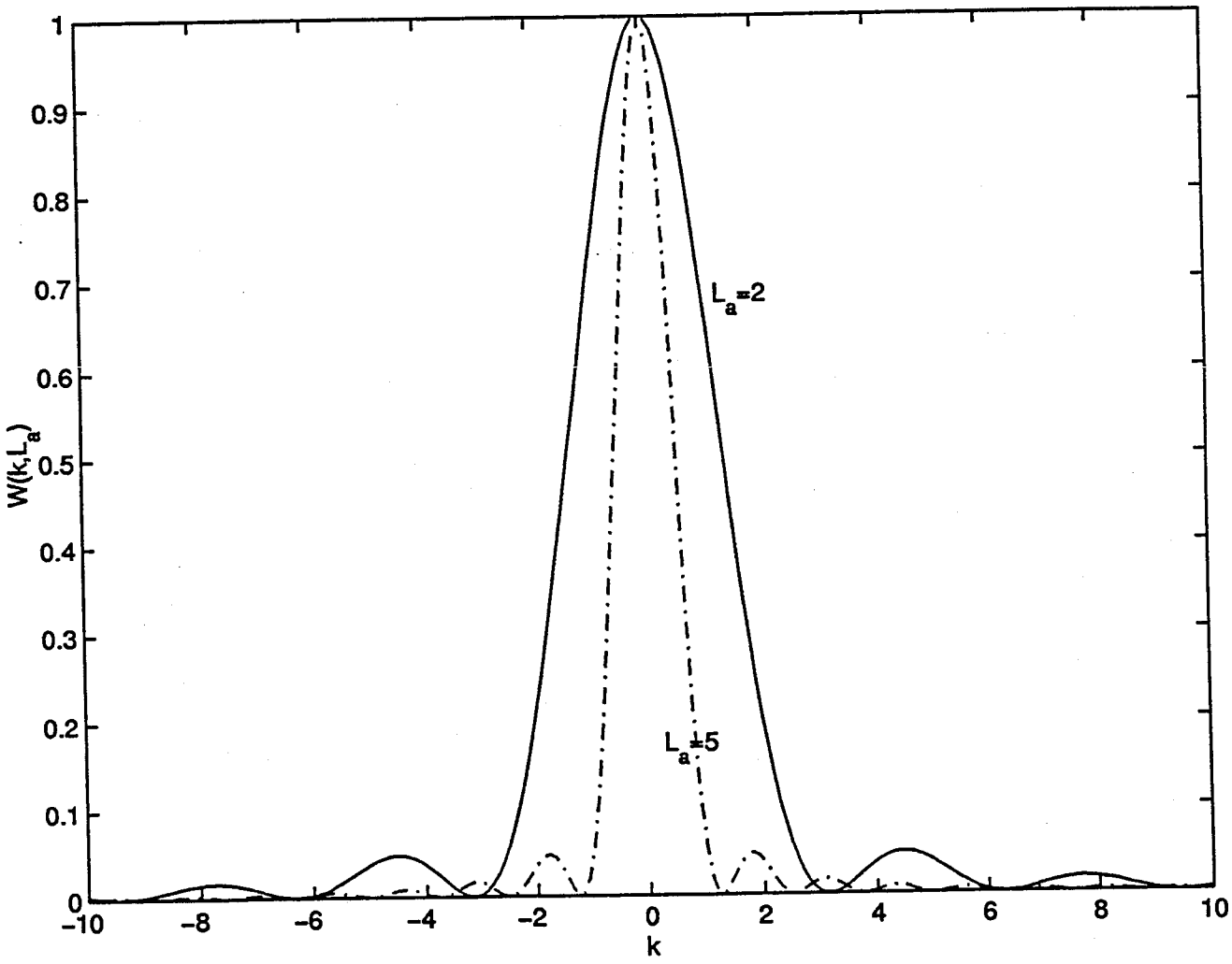

Figure 3-2: The filtering function $W(k, L_a)$.

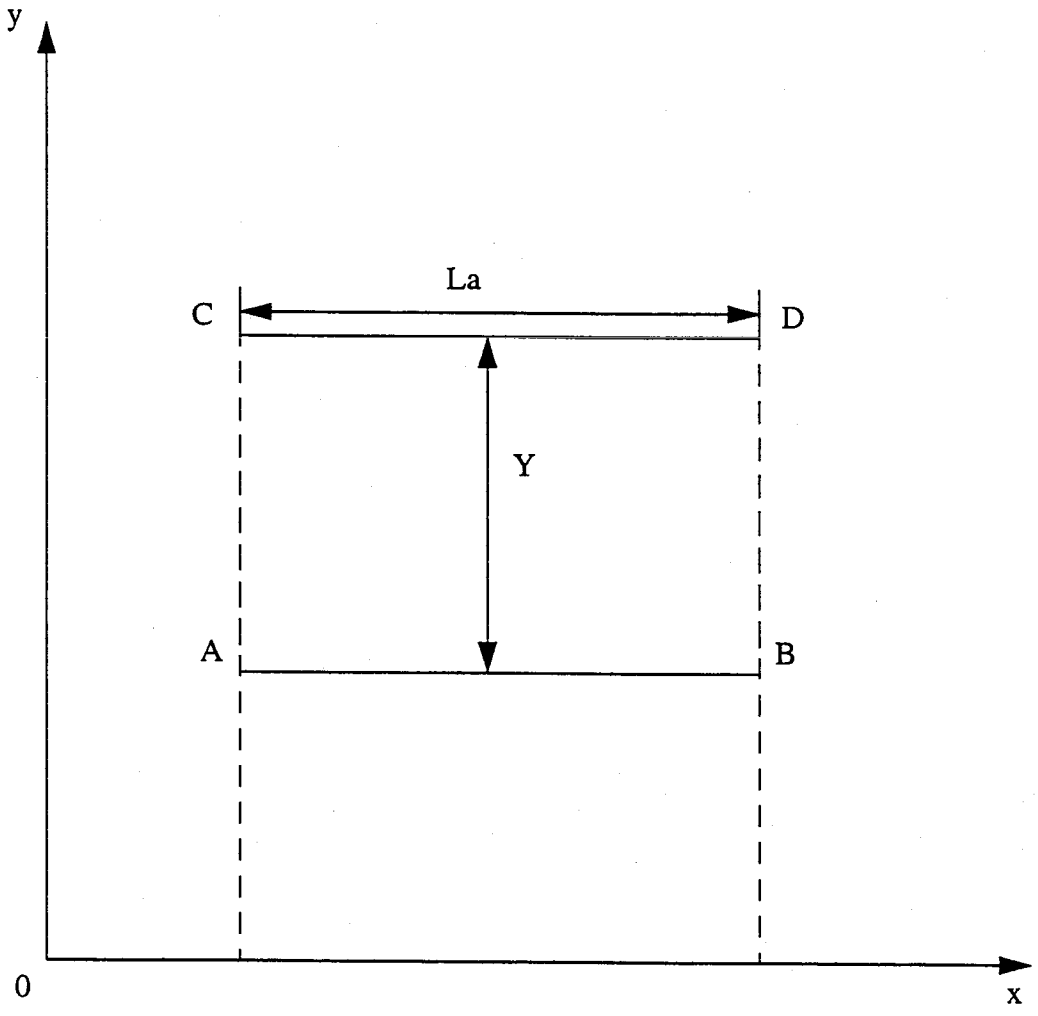

Figure 3-3: Sketch of the ray paths AB and CD in a special case.

Chapter 4

Spectral description of low frequency oceanic variability

The oceanic variability is a function of (x, y, z, t) in physical space and a function of horizontal wavenumber, vertical mode and frequency (k, l, n, ω) in Fourier space. Wunsch [1981] gave a review of frequency spectra of temperature and velocity based on data obtained before 1981. During the past decades, because of the advance of measurements and the emergence of two new measurement techniques, acoustic tomography and satellite altimetry, a three–dimensional description of oceanic variability has become possible. In this chapter, we review the low frequency oceanic variability based on the more recent results. We will also analyze some new data ourselves. Emphases are put on answering the following questions: how the kinetic energy and temperature variability depends on horizontal wavenumber, frequency and vertical mode? which characteristic features of low frequency variability are independent of geography? which ones are geography–dependent? and how do they depend on geography? We will summarize the various observations and give a zero order description of the low frequency oceanic variability.

4.1 Frequency spectra

Frequency spectra of oceanic variability have previously been computed from time series of moored current meters and thermistors. A review of earlier results is given by Wunsch [1981]. According to his findings, almost everywhere the frequency spectra of velocity show an isotropic high-frequency with a spectral slope of about ω^{-2} followed by an energy containing band towards longer periods. At the longest periods, observed motions become anisotropic with a tendency towards zonality. Overall, the temperature frequency spectral shape is independent of geography also and is similar to that of velocity. In the regions away from the main topography, the frequency spectral shape of the horizontal velocities and temperature is independent of depth, and the energy level of the temperature frequency spectra drops more rapidly with depth than that of horizontal velocities. One important property of the frequency spectra is that the energy level depends on geography and the energy level increases toward the western boundary. Recently, Wunsch and Stammer[1995] calculated the frequency spectra of sea surface height and sea surface slope from TOPEX/POSEIDON altimetry data. The global averaged frequency spectrum of sea surface slope is shown in figure 4.1. On time scales shorter than 60 days the spectra approximately follow an ω^{-2} power law, with an almost "white" long–period plateau and an intermediate $\omega^{-1/2}$ regime. The peak near a period of 60 days is a tidal alias [Wunsch and Stammer, 1995].

According to Stammer [1997], the regional frequency spectra from T/P altimetry can be summarized by three basic types representing: (i) the energetic boundary currents, (ii) the bulk of the extratropical basins, and (iii) the tropical interior oceans. There exists pronounced similarity in the shape of all the spectra from each dynamical category. In the interior ocean the general shape of the sea surface height and sea surface slope spectra basically agrees with that of the global average but with less energy [Figure 4.2]. In general, the slope spectral characteristic, with a flat low–frequency part and a steeper decay at higher frequencies appears qualitatively consistent with results from moored current meter data.

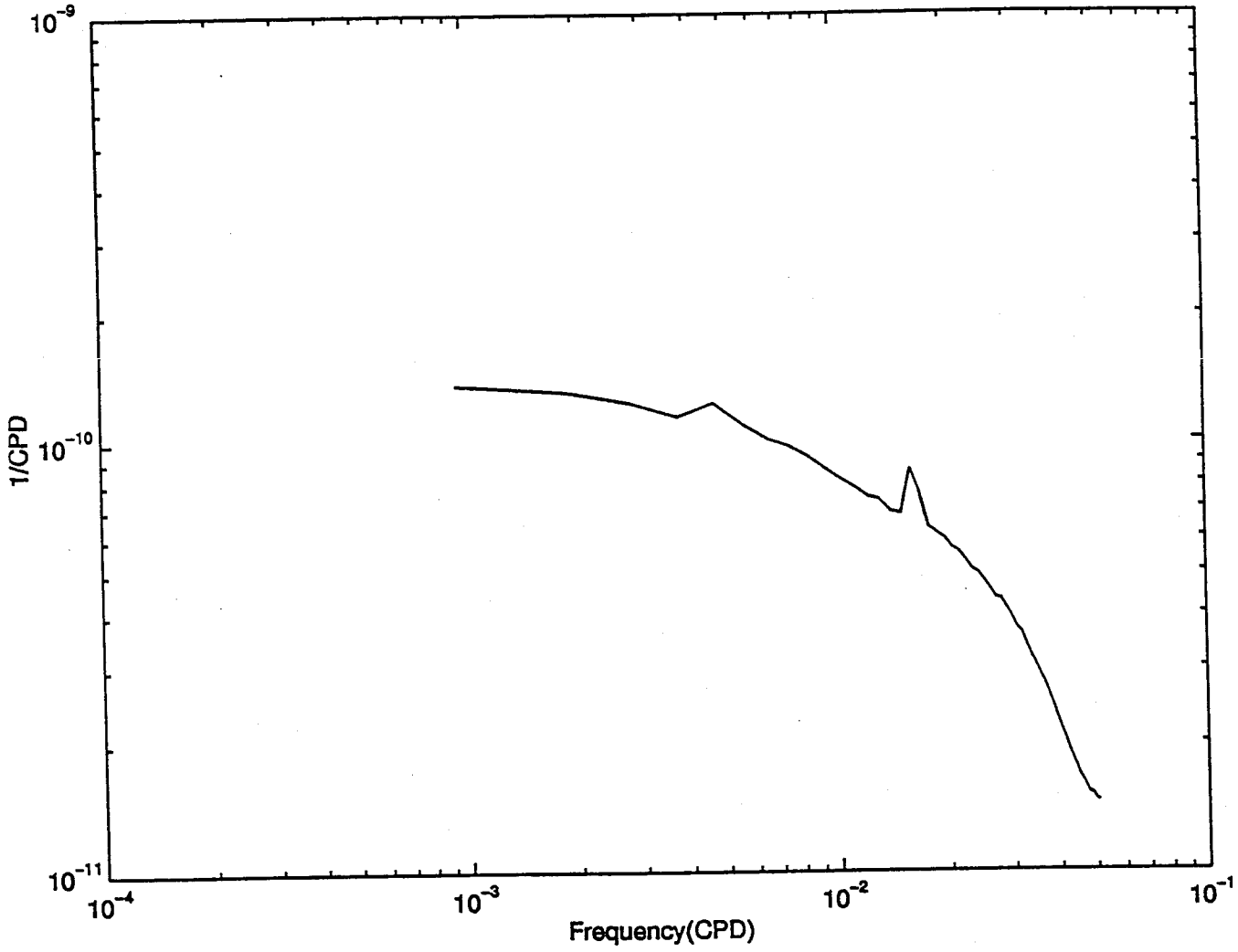

Figure 4-1: The global averaged frequency spectrum of sea surface slope (Stammer 1997).

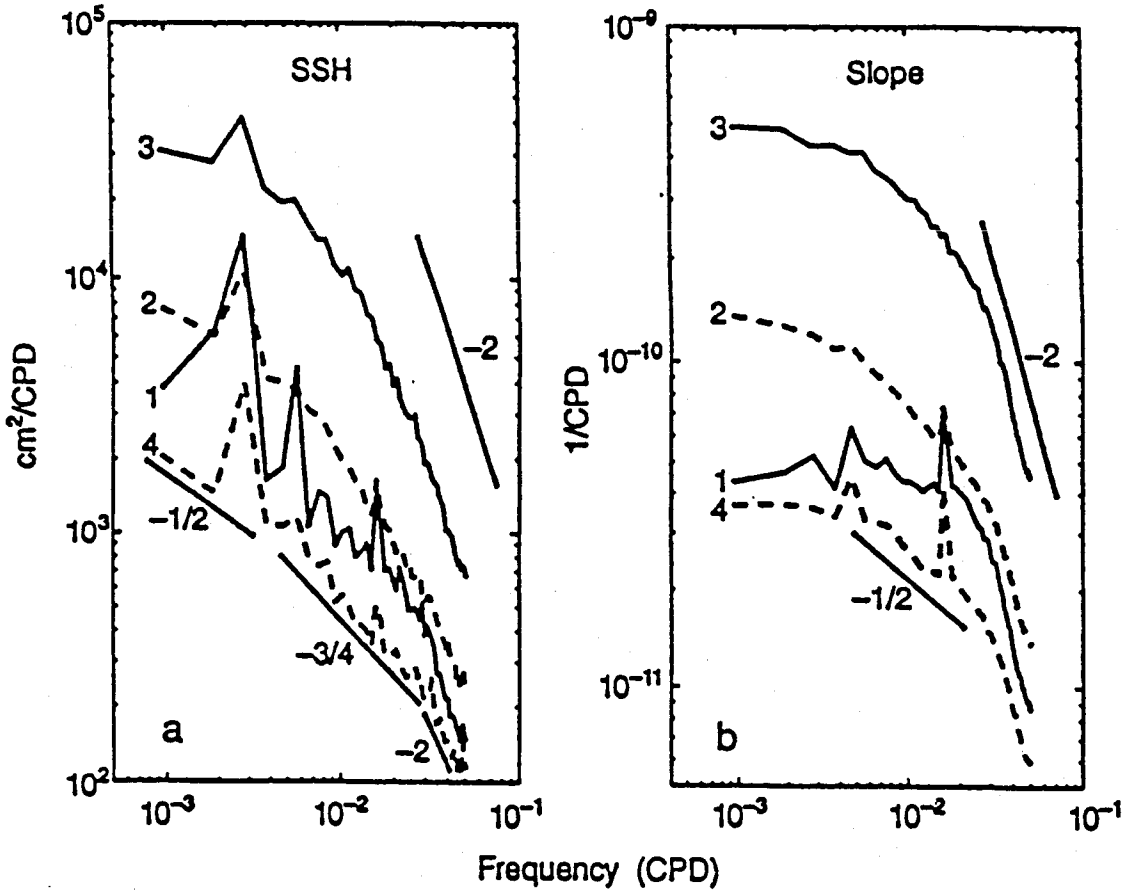

Figure 4-2: (a) Averaged frequency spectra from 1) the Tropics, 2) the bulk of the global ocean, 3) the high energy areas, and 4) the very low energy areas, respectively. (b) As in (a) but for the alongtrack slope component (Stammer 1997).

4.2 Kinetic energy wavenumber spectra

Compared with the frequency spectra, the wavenumber spectra of low frequency oceanic variability are much more difficult to obtain by conventional measurements. The time series from repeated expendable bathythermograph (XBT) lines yield some regional temperature wavenumber spectra. Due to satellite altimetry, the wavenumber spectra for whole ocean basin have been obtained. The first global wavenumber spectra for sea surface height and sea surface slope were constructed by Wunsch and Stammer [1995]. Stammer [1997] studied how the frequency and wavenumber spectra of the sea surface height and sea surface slope depend on geography. Basically the global averaged wavenumber spectrum of sea surface slope has a maximum at about 400 km wavelength. The spectrum follows a $k^{+3/2}$ relation at wavelengths greater than 400 km, a k^{-1} relation between 400 km and 150 km wavelength, and a k^{-2} relation at shorter wavelengths [Figure 4.3]. The "blue" wavenumber energy spectral shape at wavelengths shorter than 60 km in figure 4.3 is dominated by noise rather than oceanic signal and the possible reasons for this include residual aliasing of high frequency motions and the break down of the geostrophic assumption [Wunsch and Stammer, 1995].

The examples of regional wavenumber spectra are shown in figure 4.4 from several 10° by 10° area in the latitude band spanning 30° to 40° across the North Atlantic. In general the regional wavenumber spectral shape is consistent with the global averaged one. However, there exists striking geographical variation in the energy level. The energy level for the sea surface height and cross–track velocity for wavelengths longer than about 100 km increases greatly from the low energy area in the eastern and central subtropical gyre toward the energetic western boundary.

Besides the energy level, the cutoff wavenumber k_0 where the slope wavenumber spectrum obtains its maximum exhibits a latitudinal dependency, decreasing from high latitudes toward the equator [Figure 4.5]. Stammer [1997] found a close relationship between k_0 and the first baroclinic Rossby radius.

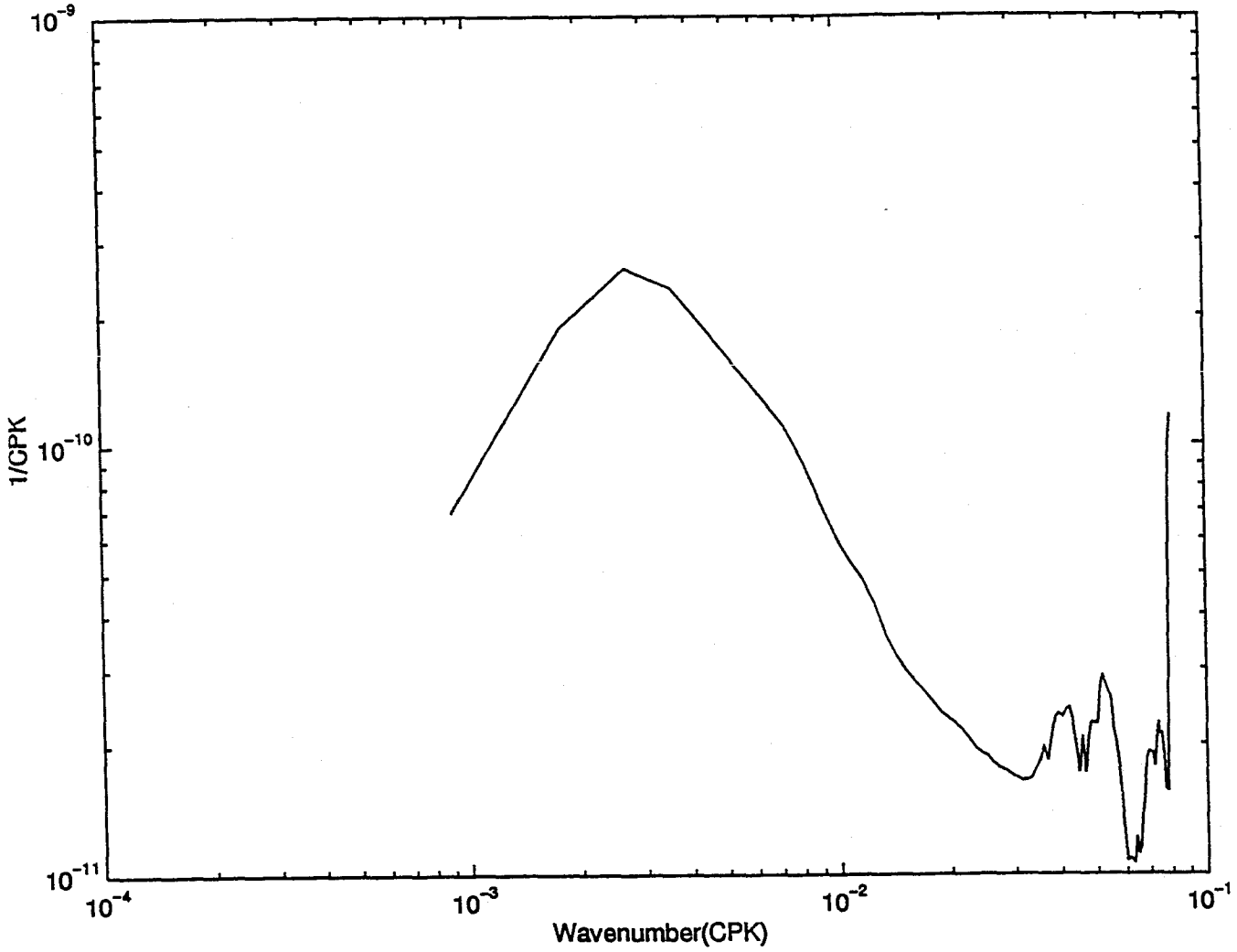

Figure 4-3: The global averaged wavenumber spectrum of sea surface slope (Stammer 1997).

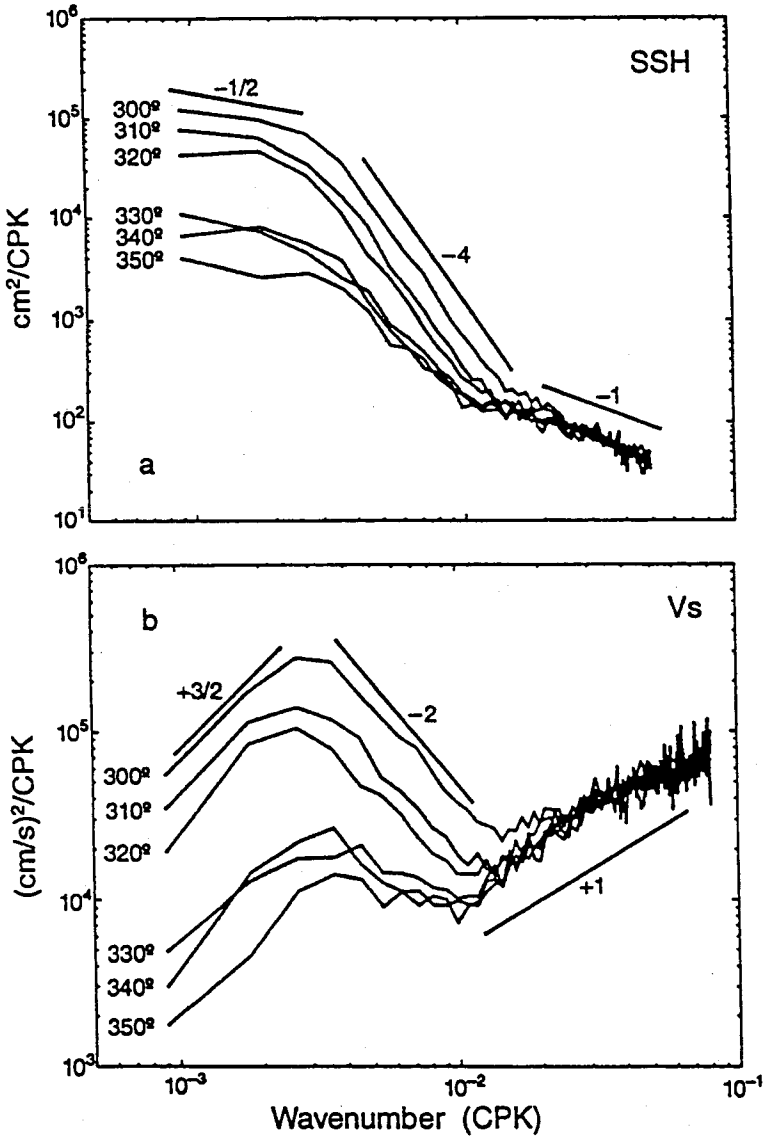

Figure 4-4: TOPEX/POSEIDON mean alongtrack wavenumber spectra for (a) sea surface height and (b) cross-track velocity from various 10° × 10° areas between 30° and 40°N with longitudes indicated in the figure (Stammer 1997).

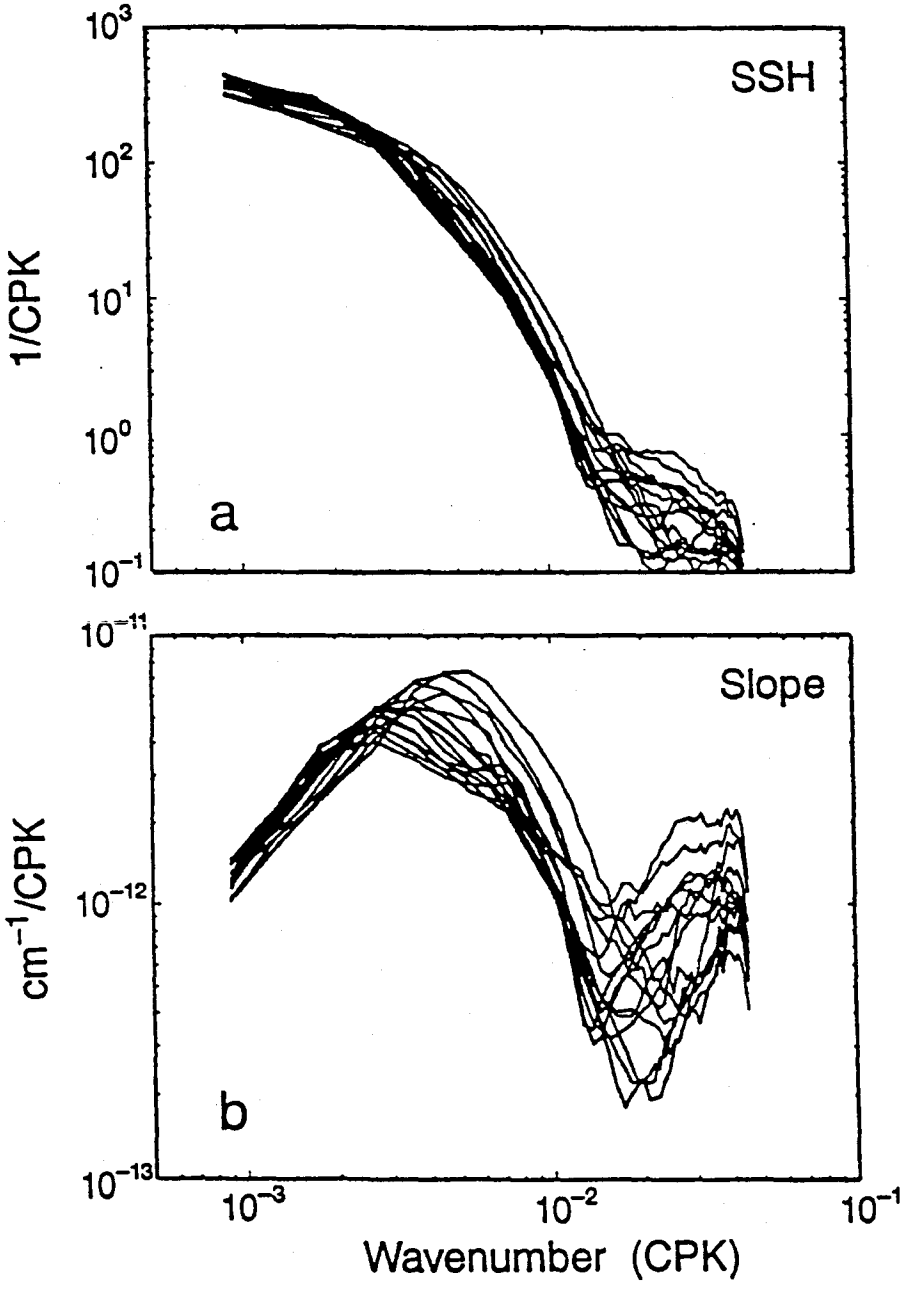

Figure 4-5: Zonally averaged sea surface height (a) and sea surface slope (b) wavenumber spectra shown for latitudes poleward of 20°(Stammer 1997).

4.3 Temperature wavenumber spectra

Review of previous results

Roemmich and Cornuelle [1990] investigated the temperature horizontal wavenumber spectrum from a time series of expendable bathythermograph (XBT) sections between New Zealand and Fiji. Figure 4.6 shows horizontal wavenumber spectra of temperature at 400 m depth. The solid line is the wavenumber spectrum of the mean temperature. The dashed line in figure 4.6 is the averaged spectrum of the fluctuations. At a wavelength of about 2000 km, the spectra of the mean and fluctuations have equal energy. The energy level of the mean field is higher at wavelengths longer than 2000 km and it drops off very sharply at wavelengths near 2000 km. At wavelengths shorter than 2000 km, the energy level of the fluctuations is higher. Energy in the fluctuations slopes off at a rate of about $k^{-1/2}$ out to a wavelength of about 300-500 km. At that point there is an increase in the slope, which becomes about k^{-3}.

Results from new data

The data used in the following come from the repeated XBT lines in the North Pacific between San Francisco and Hawaii. The data provide many "snapshots" of a slice across the low energy area in the eastern and central subtropical gyre. The data are unique since the horizontal resolution is sufficiently fine so that mesoscale eddies can be resolved. The details of the XBT data are listed in table 4.1. The data have been mapped on a regular grid using an objective mapping technique by Cornuelle. The objectively mapped data were then averaged in time at each grid point over all 20 transects of the region. The sample mean and standard deviation are shown in figure 4.7. The gyre–scale slopes of isotherms are obvious in the figure of the sample mean. The large–scale slope of isotherms is upward towards the south. The vertical gradient of the mean temperature at a certain depth changes strongly along the XBT line. The standard deviation map shows a pronounced surface maximum. In the main thermocline, there are some distinct maxima and the position of the maxima in the figure of standard deviation corresponds to the maximum vertical temperature

gradients in the mean temperature field.

The wavenumber spectra for the mean temperature and perturbations are shown in figure 4.8. In general, the spectral shape in figure 4.8 is similar to that in figure 4.6. For the averaged spectrum of the fluctuations, the slope is about $k^{-1/2}$ at wavelengths longer than 400 km. There is a transitional point at wavelengths between 300 km and 500 km. At wavelengths shorter than 300 km, the spectral slope of the fluctuations in figure 4.8 becomes about k^{-3}. One interesting fact is that the transitional point in figure 4.8 corresponds to the cutoff wavenumber in the wavenumber spectrum of sea surface slope in figure 4.3. By comparing figure 4.3 with 4.8, we find that the ratio of temperature fluctuation horizontal wavenumber spectrum to the kinetic energy horizontal wavenumber spectrum is proportional to k^{-2} at the wavelengths longer than 100 km. These imply that there is a relation between the temperature wavenumber and velocity wavenumber spectrum and we will discuss this in detail in next section. There are two obvious differences between figures 4.6 and 4.8. First, the energy level in figure 4.8 is about one order of magnitude lower than that in figure 4.6. We must be aware of the different scales used in figures 4.6 and 4.8. The data for figure 4.8 is taken from the low energy area in the eastern and central North Pacific, while the data for figure 4.6 is from the area near the western boundary in the South Pacific where there is strong variability. Second, at wavenumbers greater than 0.008 CPK, the spectral slope in figure 4.8 is steeper than that in figure 4.6. One possible reason for this is that the ship track between New Zealand and Fiji was precisely repeated and from one voyage to the next the ship did not deviate by more than a few kilometers. In contrast, between San Francisco and Hawaii the deviation of the ship track from one voyage to the next is greater, on the order of tens kilometers. This deviation of the ship track might contribute to the spectral difference between figures 4.6 and 4.8 at wavenumbers higher than 0.008 CPK. Just as the frequency spectra of temperature and horizontal velocities, the wavenumber spectral shape of the temperature is approximately independent of depth and the energy level drops with depth [Figure 4.9].

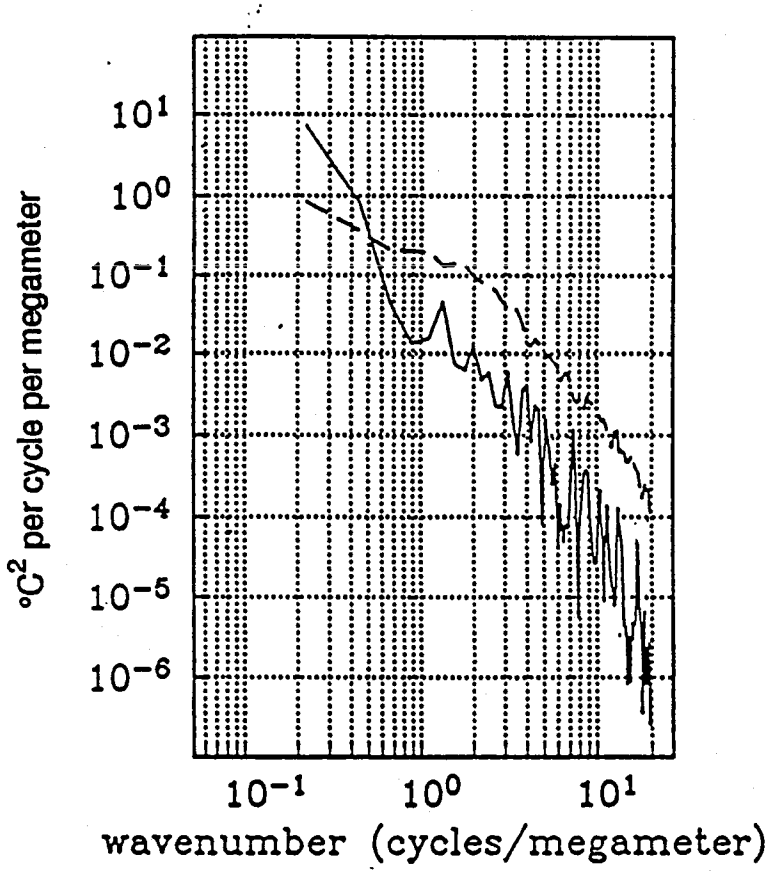

Figure 4-6: Horizontal wavenumber spectrum of temperature at 400 m. The solid line is the spectrum of the mean temperature field. The dashed line is the average of the spectra of the time varying temperature (Roemmich and Cornuelle 1990).

Cruise designation	Dates	Shallowest depth	Deepest depth
1	19–23 Sep 1991	0	850 (m)
2	16–20 Apr 1992	0	850 (m)
3	12–16 Nov 1992	0	850 (m)
4	8—12 Apr 1993	0	850 (m)
5	22–26 Jul 1993	0	850 (m)
6	4— 8 Nov 1993	0	850 (m)
7	17–21 Feb 1994	0	850 (m)
8	2— 6 Jun 1994	0	850 (m)
9	11–15 Aug 1994	0	850 (m)
10	24–28 Nov 1994	0	850 (m)
11	2— 6 Feb 1995	0	850 (m)
12	18–22 May 1995	0	850 (m)
13	27–31 Jul 1995	0	850 (m)
14	9—13 Nov 1995	0	850 (m)
15	1— 6 Feb 1996	0	850 (m)
16	16–20 May 1996	0	850 (m)
17	25–29 Jul 1996	0	850 (m)
18	3— 7 Oct 1996	0	850 (m)
19	16–20 Jan 1997	0	850 (m)
20	27–31 Mar 1997	0	850 (m)

Table 4.1: List of XBT cruises

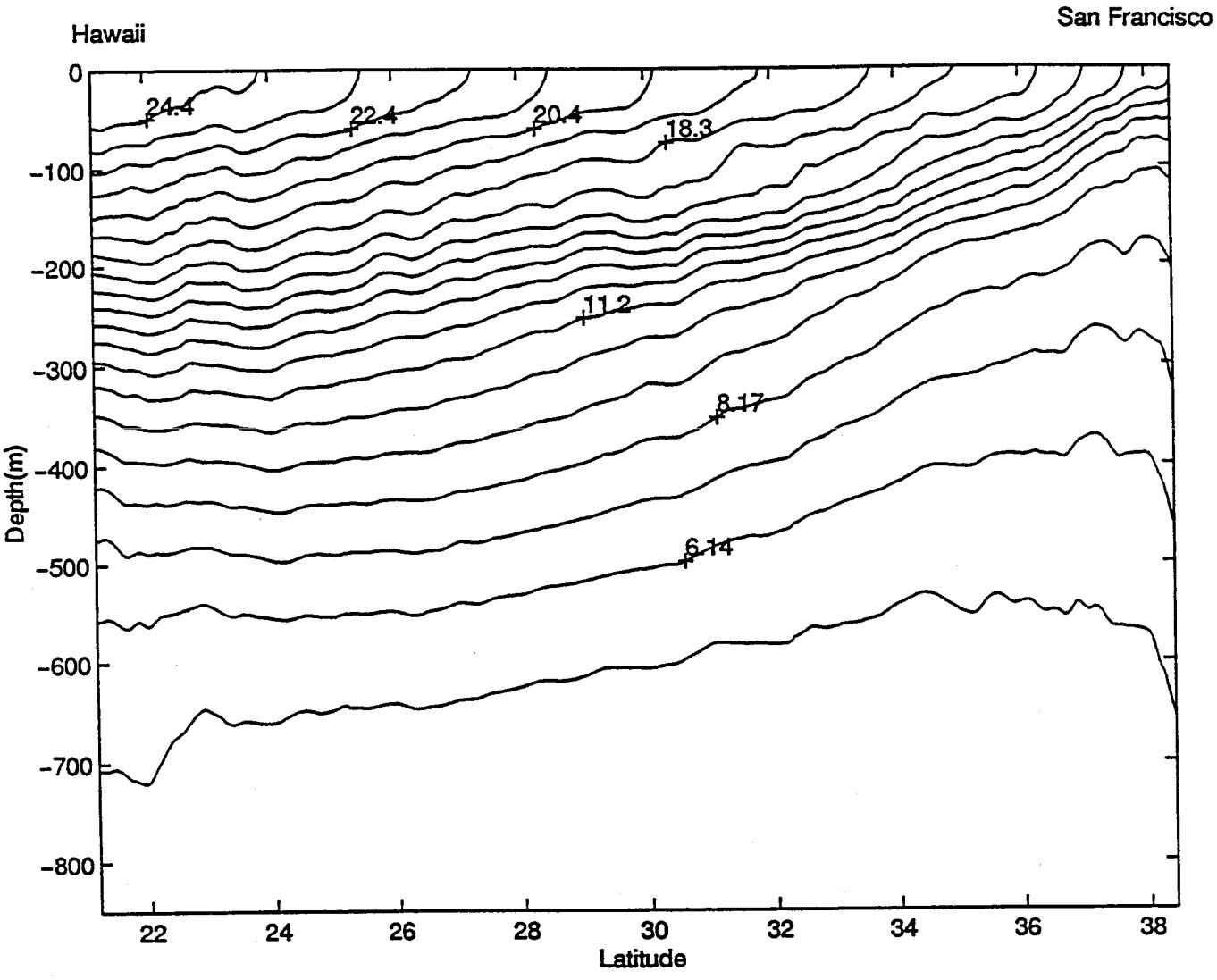
Hawaii
San Francisco
0
-100
-200
-300
-400
-500
-600
-700
-800
Depth(m)
24.4
22.4
20.4
18.3
11.2
8.17
6.14
22
24
26
28
30
32
34
36
38
Latitude

(a)

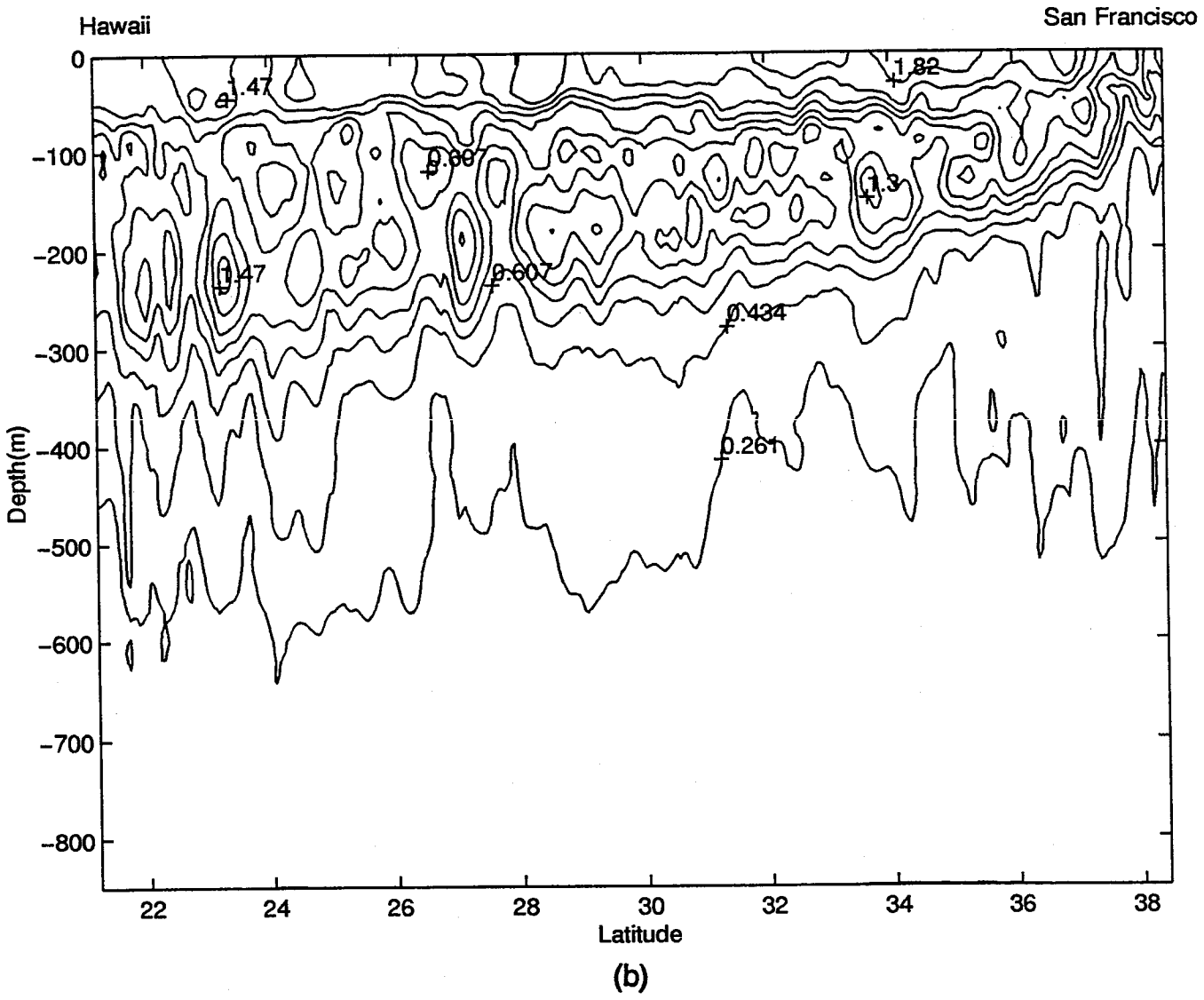

Figure 4-7: (a) Mean temperature field formed by time-averaging of gridded (objectively mapped) data from all cruises. (b) Standard deviation of temperature.

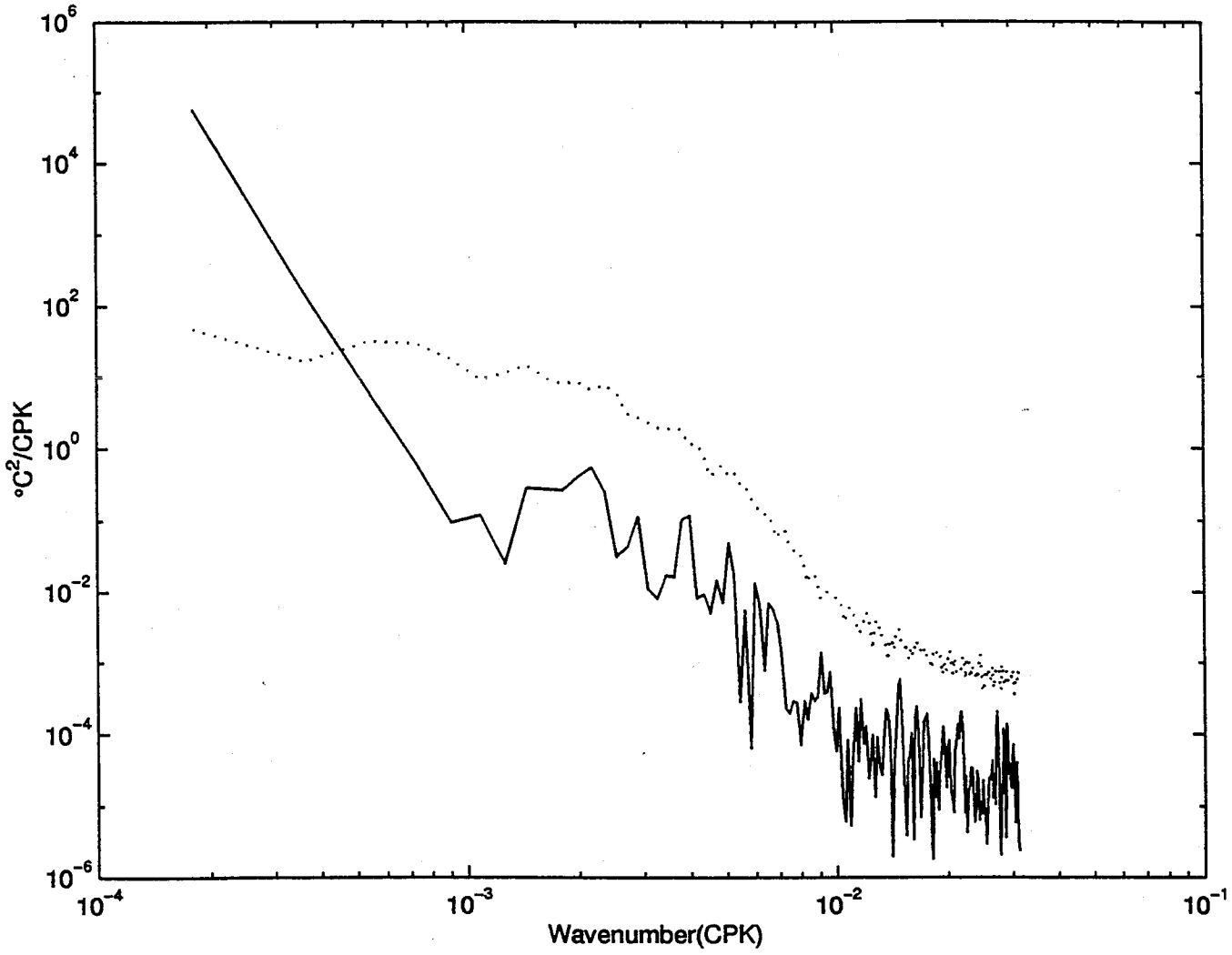

Figure 4-8: Horizontal wavenumber spectrum of temperature at 400 m. The solid line is the spectrum of the mean temperature field. The dashed line is the average of the spectra of the time varying temperature.

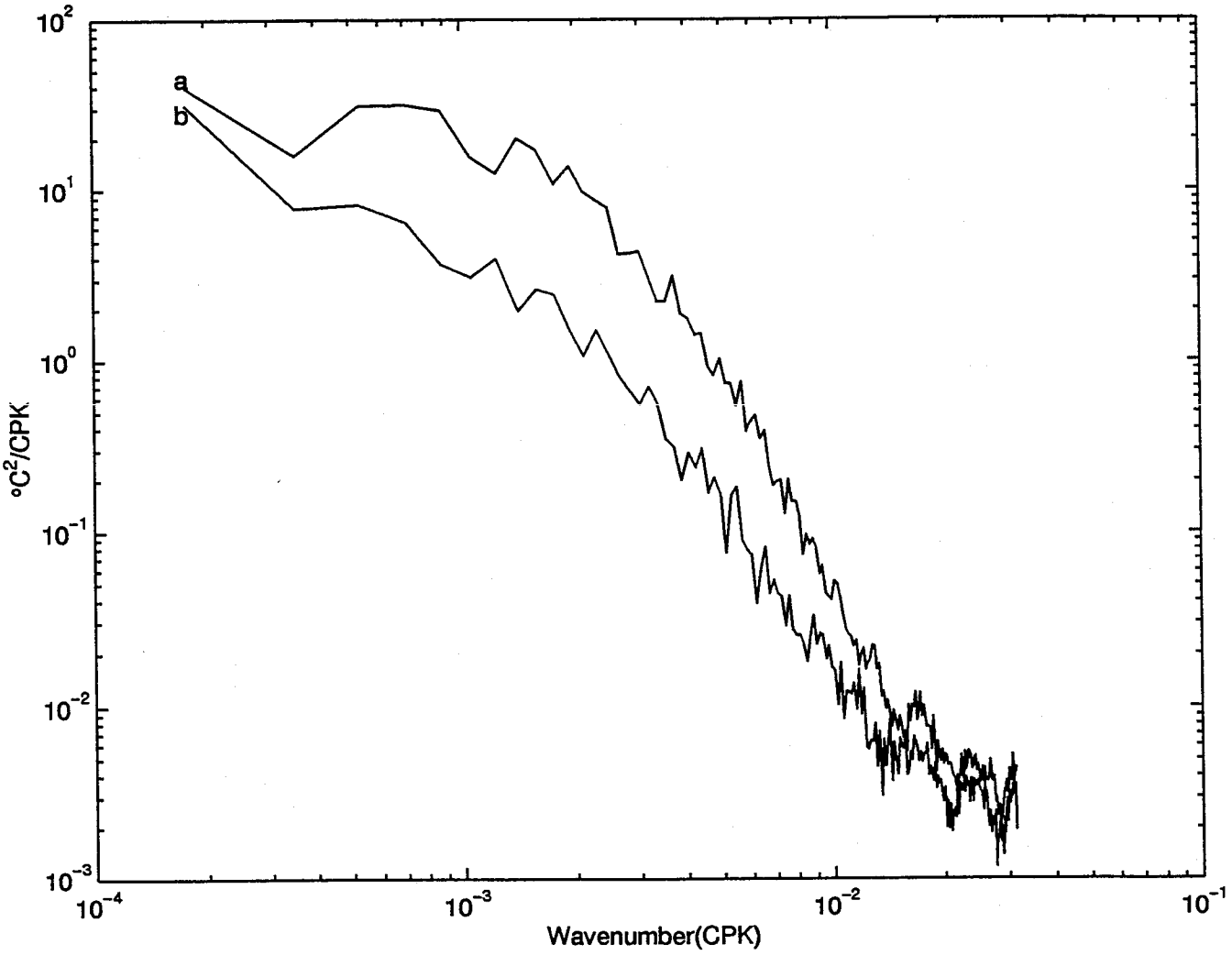

Figure 4-9: Horizontal wavenumber spectra of temperature fluctuations (a) at 400 m and (b) at 800 m.

4.4 Consistency relation between kinetic energy and temperature wavenumber spectra

The astute reader might have noticed a superficial relationship between the kinetic energy horizontal wavenumber spectrum and temperature horizontal wavenumber spectrum. First, both the kinetic energy horizontal wavenumber spectrum and the temperature horizontal wavenumber spectrum have a transitional point at the wavelength of about 400 km. Second, the ratio of temperature horizontal wavenumber spectrum to the kinetic energy horizontal wavenumber spectrum at wavelengths longer than 100 km is proportional to K^{-2}. Because the observed horizontal wavenumber spectral shape is independent of depth, we can infer that the spectral shape of each mode is identical, just like the spectral shape of the obsevations, and that the vertical modes only contribute to the energy level, not the spectral shape. Therefore, the ratio of temperature horizontal wavenumber spectrum to the kinetic energy horizontal wavenumber spectrum of each baroclinic mode is proportional to K^{-2} (For the barotropic mode, the temperature perturbation is zero). These are not mere coincidences. On the other hand, these imply some dynamical relationships between the temperature and the velocity. In chapter 3, we derived the model wavenumber spectra of the kinetic energy and the temperature. As shown by the equations (3.52) and (3.54), the model wavenumber spectra of the kinetic energy and the temperature of each mode are indirectly related to each other through the intermediate variable: the energy density $\Phi(K, \omega, n)$. The ratio of the model temperature horizontal wavenumber spectrum to the model kinetic energy horizontal wavenumber spectrum of each baroclinic mode is proportional to K^{-2} as well. So the model result is consistent with the observations.

In some cases, it's possible to derive direct relationships among different variables from a theoretical model that may be tested directly against the same relationships evaluated from observations so that the implied dynamics between different variables will be more obvious to us. In the following, we will derive a direct relationship

between the velocity horizontal wavenumber spectrum and the temperature horizontal wavenumber spectrum from a simple theoretical model.

As we have mentioned in chapter 2, away from the immediate vicinity of the sea surface and the equator, the low frquency and large scale oceanic general circulation is dominated by the geostrophic balance relations in the horizontal direction:

$$fv = \frac{1}{\rho_0}\frac{\partial p}{\partial x}, \tag{4.1}$$

$$fu = -\frac{1}{\rho_0}\frac{\partial p}{\partial y}, \tag{4.2}$$

and the vertical momentum equation is dominated by hydrostatic balance:

$$\frac{\partial p}{\partial z} = -\rho g. \tag{4.3}$$

Here u and v are the perturbation horizontal velocities, p is the perturbation pressure, ρ is the perturbation density, f is the Coriolis parameter and ρ_0 is the density of the rest ocean.

From equations (4.1), (4.2) and (4.3), one can get the thermal wind relation:

$$f\frac{\partial v}{\partial z} = -\frac{g}{\rho_0}\frac{\partial \rho}{\partial x}, \tag{4.4}$$

$$f\frac{\partial u}{\partial z} = \frac{g}{\rho_0}\frac{\partial \rho}{\partial y}. \tag{4.5}$$

The density ρ is a function of temperature T and salinity S (for fixed pressure p), and the effect of salinity is relatively small. An equation for ρ in terms of T and S is a complicated function but to zero order can be linearized as:

$$\rho = \gamma T, \tag{4.6}$$

where γ is a constant coefficient.

Substitution of equation (4.6) into equations (4.4) and (4.5) yields the relationship

between the horizontal velocities and temperature

$$f\frac{\partial v}{\partial z} = -\gamma\frac{g}{\rho_0}\frac{\partial T}{\partial x}, \tag{4.7}$$

$$f\frac{\partial u}{\partial z} = \gamma\frac{g}{\rho_0}\frac{\partial T}{\partial y}. \tag{4.8}$$

Define the Fourier transform of $f(x)$ as $\hat{f}(k)$:

$$\tilde{f}(k) = \mathcal{F}(f(x)) = \frac{1}{2\pi}\int_{-\infty}^{+\infty} f(x)e^{ikx}dx. \tag{4.9}$$

The derivative theorem gives:

$$\mathcal{F}(f^{'}(x)) = ik\tilde{f}(k). \tag{4.10}$$

Because the horizontal wavenumber spectral shape is independent of depth and we are only interested in the spectral shape here, we don't need to worry about the vertical dependent factors in equation (4.7) and (4.8) which only contribute to the energy level of horizontal wavenumber spectrum.

Using the property of Fourier Transform (4.10) and taking the Fourier transform of equation (4.7) with respect to x, one get

$$\tilde{f}_v(k) \propto k\tilde{f}_T(k). \tag{4.11}$$

Similarly, equation (4.8) yields

$$\tilde{f}_u(l) \propto l\tilde{f}_T(l). \tag{4.12}$$

From these above two equations, it is readily shown that the relationship between the velocity horizontal wavenumber spectrum and the temperature horizontal wavenumber spectrum is:

$$\frac{F_v(k)}{F_T(k)} = \frac{|\tilde{f}_v(k)|^2}{|\tilde{f}_T(k)|^2} \propto k^2, \tag{4.13}$$

$$\frac{F_u(l)}{F_T(l)} = \frac{|\tilde{f}_u(l)|^2}{|\tilde{f}_T(l)|^2} \propto l^2, \tag{4.14}$$

where k and l are the horizontal wavenumber along x–axis and y–axis, respectively.

By assuming isotropy, one could heuristically get the following relationship between kinetic energy horizontal wavenumber spectrum and temperature horizontal wavenumber spectrum:

$$\frac{F_k(K)}{F_T(K)} \propto K^2, \tag{4.15}$$

where K is the horizontal wavenumber amplitude.

So the relationship between observed kinetic energy horizontal wavenumber spectrum and temperature horizontal wavenumber spectrum suggests that the dynamics between them is governed by the thermal wind relation.

4.5 Spectra of acoustic tomographic data

Several experiments have demonstrated the success of acoustic tomography in monitoring the oceanic temperature field, current velocities, and vorticity field [Munk et al. 1995]. In section 3.3, we have shown analytically that the the spatial integration of the tomographic data can filter out small scale motions. In the following, we will use the tomographic data to investigate the low frequency variability of the ocean.

4.5.1 RTE87 Data

From May to September 1987, three acoustic transceivers were deployed north of Hawaii between the subtropical and subarctic fronts [Figure 4.10]. This experiment, called the 1987 Reciprocal Tomography Experiment (RTE87), has been described in detail by Dushaw et al [1993a,b, 1994]. During RTE87, transmissions were made bihourly on every fourth day. The data collected consisted of the travel times of acoustic pulses associated with identified ray paths. The travel times are first inverted to give the sound speed fields between the transceivers. These are then converted to temperature. Dushaw et al [1993a,b] described the inversion procedure in detail. After

inversion, Dushaw et al [1993b] obtained the range– and depth–averaged temperature

$$\overline{\overline{T}} = \frac{1}{hL}\int_{-h}^{0}\int_{0}^{L} T dl dz, \tag{4.16}$$

where L is the length of acoustic ray along the horizontal direction. The depth interval of the integral is from $-h$ to 0, where $h = 2000$ m. The lengths of the three acoustic rays are East $L_e = 995$ km, West $L_w = 1275$ km, and North $L_n = 745$ km. Figure 4.11 shows the range– and depth–averaged temperature perturbations of the three legs. Because the tomographic data in figure 4.11 are range– and depth–averaged, the small-scale variations have been filtered out. Thus, the temperatures change relatively smooth over time in figure 4.11. The most noticeable point in figure 4.11 is the seasonal variability of temperature. The temperatures of the three legs all increase from May to September and three legs have nearly the same magnitude of temperature perturbations.

Spectral description of RTE87 data

The spectra of the three different legs are displayed in figure 4.12. In figure 4.12, a line with slope -2 is drawn on the log–log form of plots to make it easy to compare the spectral shapes of different data. The spectral shape of the entire group is similar. The spectral slopes of the three different legs are indistinguishable from -2. Wunsch [1981] reported that almost all the spectra of the point measurements have a similar shape with a slope not far from -2, independent of geography. So the spectral shape of the range-averaged tomographic data is the same as that of point measurements just as we predicted from theory in section 3.3. The energy level of the three legs is nearly identical. Given the form of $\Phi(K, \omega, n)$, the filtering effect of tomographic data can be calculated quantitatively from equation (3.55). In chapter 5, first we will find the form for $\Phi(K, \omega, n)$ from diverse measurements such as altimetry, XBT, etc., then we will calculate quantitatively the filtering effect due to range–averaging. The temperature wavenumber spectrum in section 4.3 shows that most of the potential energy is concentrated in low wavenumbers. So, roughly speaking, the filtering effects of these three legs are very small.

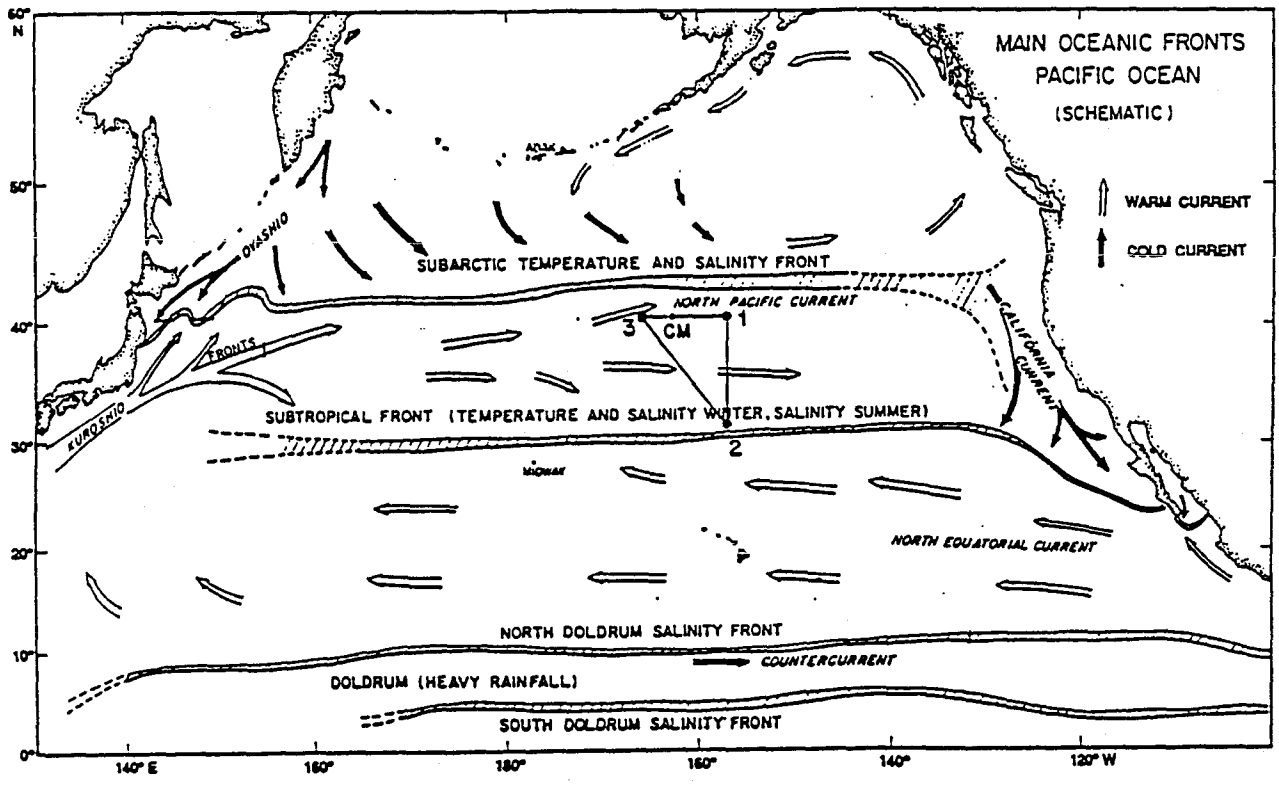

Figure 4-10: Geometry of the 1987 gyre-scale reciprocal acoustic transmission experiment, with acoustic transceivers at locations 1, 2, 3. A current meter mooring with temperature sensors is on the northern of the acoustic triangle at location CM. Reproduced from Worcester et al (1990), as modified from Roden (1975).

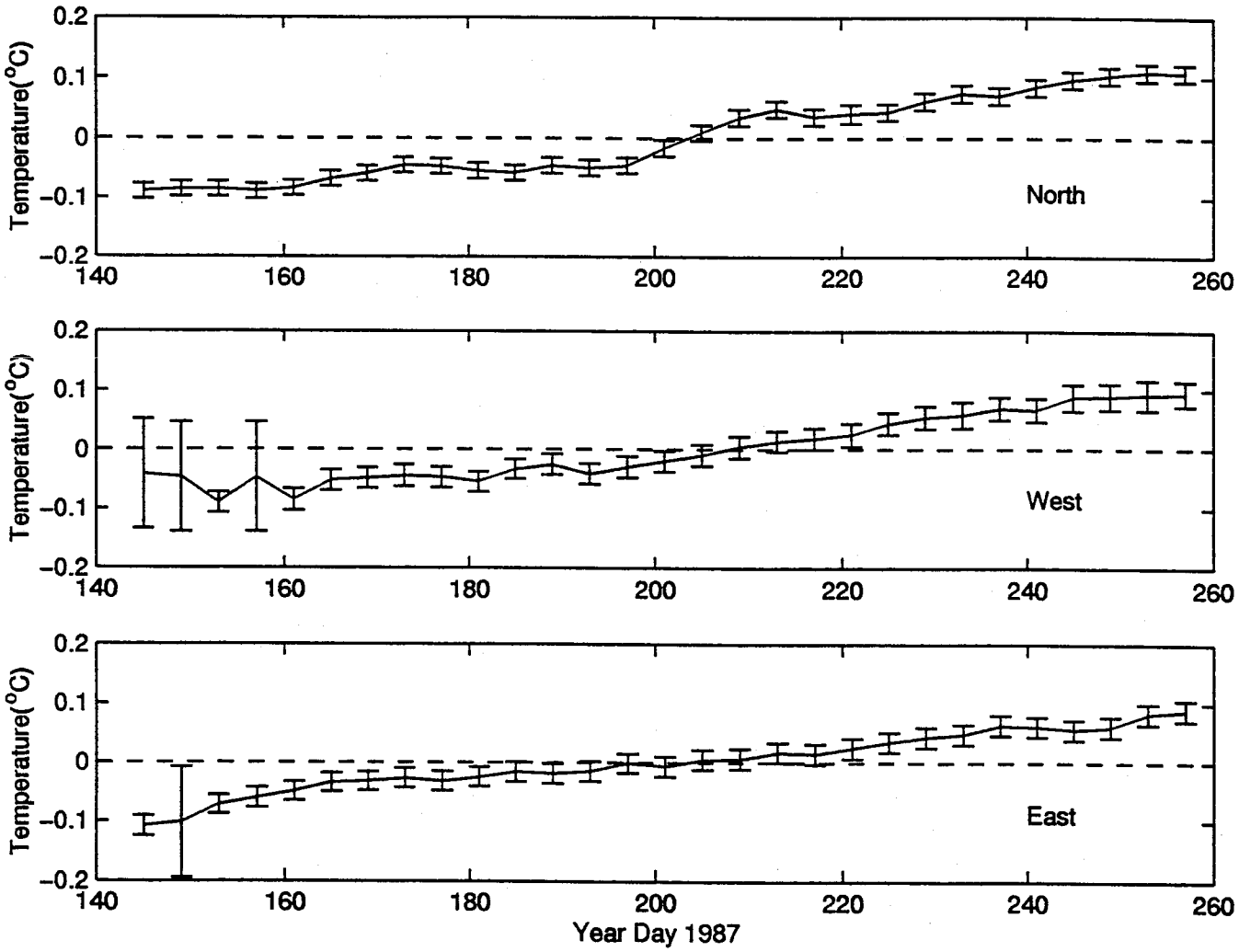

Figure 4-11: Range– and depth–averaged temperature time series for the three legs during RTE87.

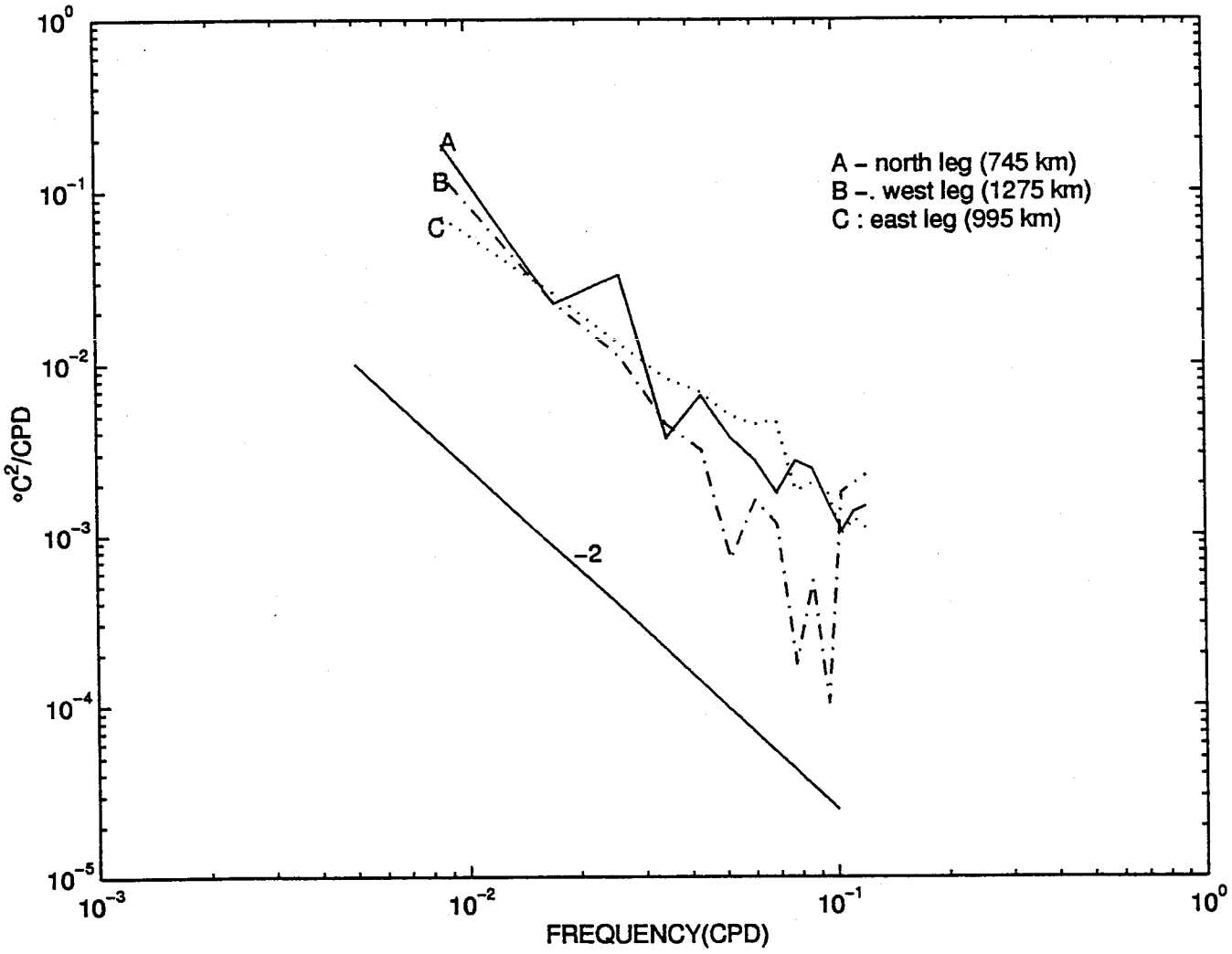

Figure 4-12: Frequency spectra of the range– and depth–averaged temperature for the three legs during RTE87.

4.5.2 ATOC data

The experiment

Acoustic transmission from the Acoustic Thermometry of Ocean Climate (ATOC) source on Pioneer Seamount off California began 28 December 1995. The precise schedule is determined by the sampling requirements of the Marine Mammal Research Project, but typically consists of 4-day periods two to four times a month and the data are irregularly spaced [Dushaw et al 1996]. Figure 4.13 indicates acoustic propagation paths for the ATOC experiment. Dushaw et al [1996] elaborated on obtaining ray travel time time series from the raw data, identification of measured ray arrivals, inversion of travel times for sound speed, and the derivation of temperature and heat content. Here we use the range- and depth-averaged temperature $\overline{\overline{T}}$ obtained by Dushaw from the inversions to investigate the low frequency variability of the ocean. Note that

$$\overline{\overline{T}} = \frac{1}{hL}\int_{-h}^{0}\int_{0}^{L} T dl dz, \tag{4.17}$$

where $h = 1000$ m. The length of the acoustic rays **k** and **l** is about 6000 km and the length of the acoustic rays **n** and **o** is about 2000 km.

Low frequency variability of ATOC data

The low-frequency temperature perturbations [Figure 4.14] are inferred from the travel times averaged over each 2– or 4–day period [Dushaw et al. 1996].

We have shown that the range–averaged temperature has filtered out certain small length–scale variations and thus is most sensitive to large-scale variations. The range and depth averaged temperature time series for rays **k**, **l** and **n** show the general overall trend [Figure 4.14]. The most conspicuous point in figure (4.14) is that the temperature perturbations for rays **k**, **l**, **n** and **o** are dominated by very low frequency variability. The temperature decreased for the first two months and then increased. The decreased temperatures are consistent with cooling during the winter season. In addition to these general trends, higher–frequency variations are also evident in these time series, perhaps indicating the influence of advection or the movement

of sharp features such as ocean fronts. The temperature perturbations for ray **k** have the largest amplitude. The temperature time series for ray **o** is coolest in late winter and early spring, about two months later than that of **k, l,** and **n**. These differences are related to the geography of each ray. Ray **k** is roughly located within the subarctic front where the variability is very strong. The receivers of **k** and **l** are quite close together and ray **l** is located north of ray **k**. The difference of temperature perturbations between **k** and **l** is very small. Ray **l** and **o** cross the subarctic and subtropical front, respectively. The receiver of ray **o** is located south of the subtropical front. The Northern part of it is within the cool California Current. The delayed cooling of ray **o** is related to the seasonal variability of the California Current. Ray **n** is situated between the subarctic and subtropical fronts where the low frequency variability is relatively smaller.

Because the ATOC data are irregularly spaced, we use a special spectral analysis method (the Lomb–Scargle algorithm) to calculate the frequency spectra. The frequency spectra of range– and depth-averaged temperature for rays **k, l, n, and o** are displayed in figure 4.15. The spectral slope of the entire group is indistinguishable from -2. According to the theory, we have shown the longer the ray path, the lower the energy level, and so the energy level for rays **k** and **l** should be lower than that of rays **n** and **o**. However, in figure 4.15 the energy level for ray **k** is relatively higher which contradicts the result predicted by the theory. Two possible reasons exist for explaining the difference between the theory and observation. First, if the energy is concentrated in large scales (very small wavenumbers), then the difference among the rays **k, l, n, and o** due to the range-averaged filtering effect is negligible, even if the length of rays **k** and **l** is about two times longer than that of **n** and **o**. Second, the theoretical result is based on the assumption that the statistical properties are homogeneous in space. However, we will see in section 4.8 that the energy level of ocean variability and the vertical gradient of mean temperature vary strongly with geography. This horizontal inhomogeneity makes it very difficult to explain the difference among spectral energy levels of different acoustic paths.

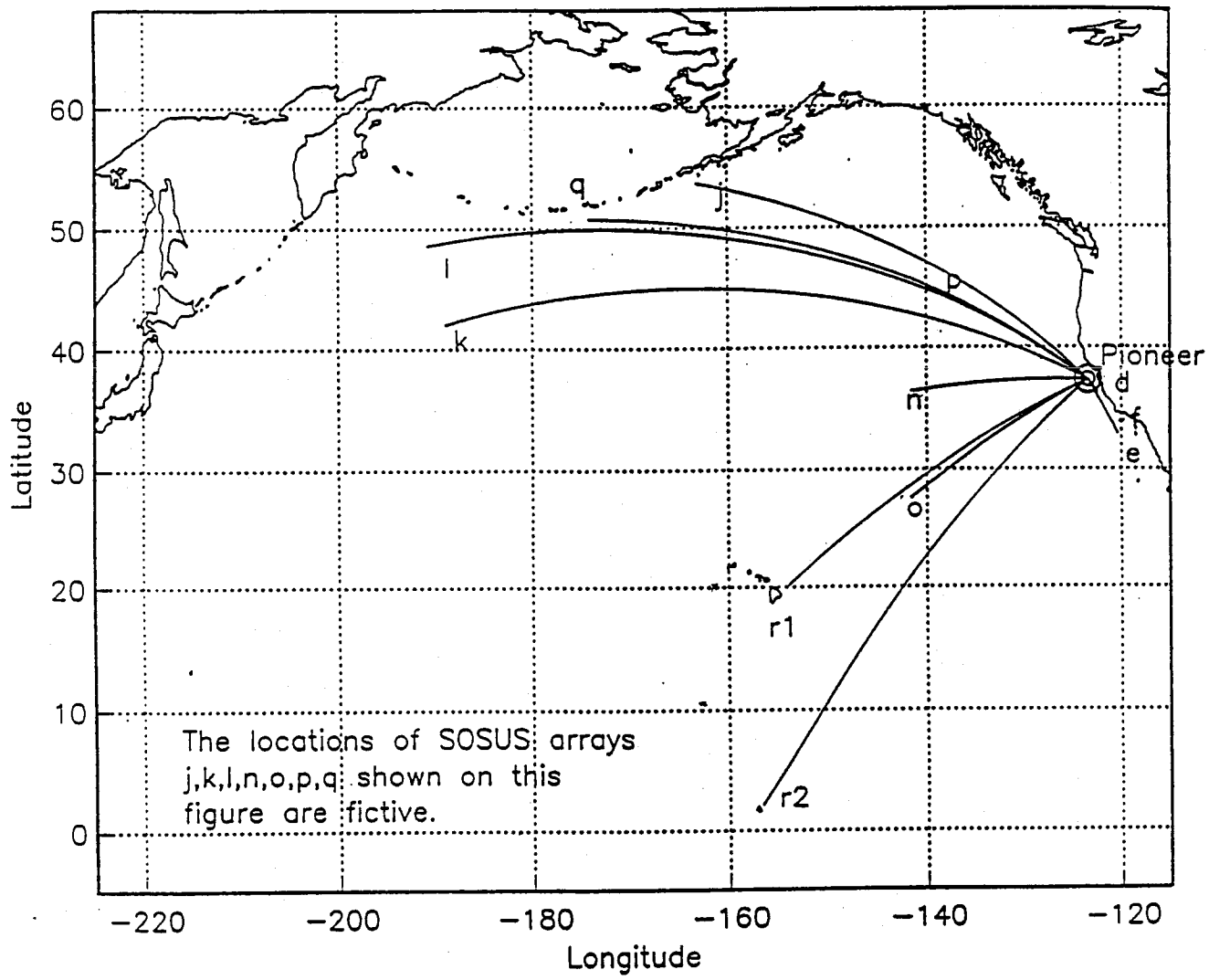

Figure 4-13: Map showing the ATOC acoustic source on Pioneer Seamount, the various receiving arrays, and the paths connecting them.

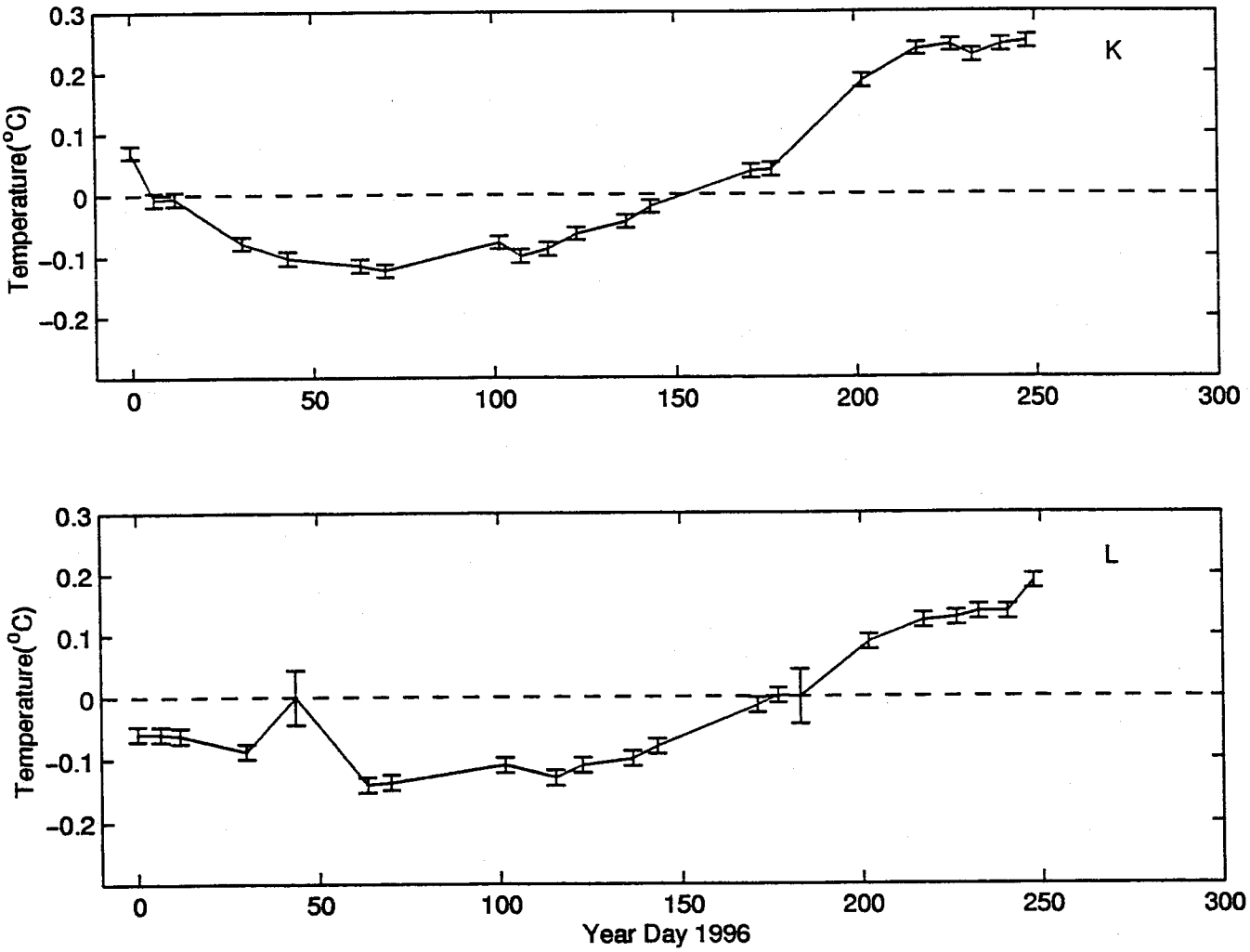
K
L
Temperature(°C)
0.3
0.2
0.1
0
-0.1
-0.2
0
50
100
150
200
250
300
Year Day 1996

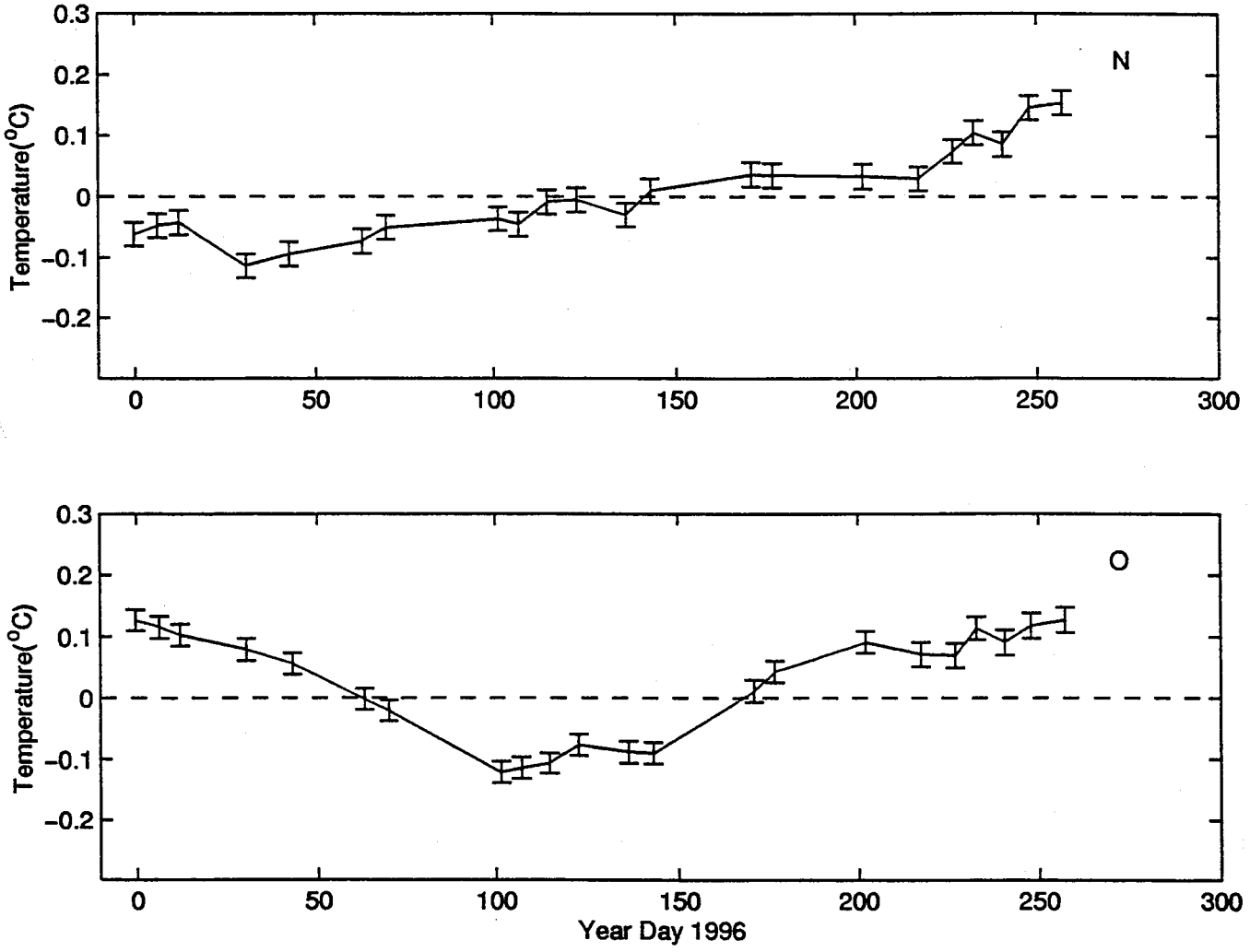

Figure 4-14: Range- and depth-averaged temperature time series for rays **k**, **l**, **n**, and **o**.

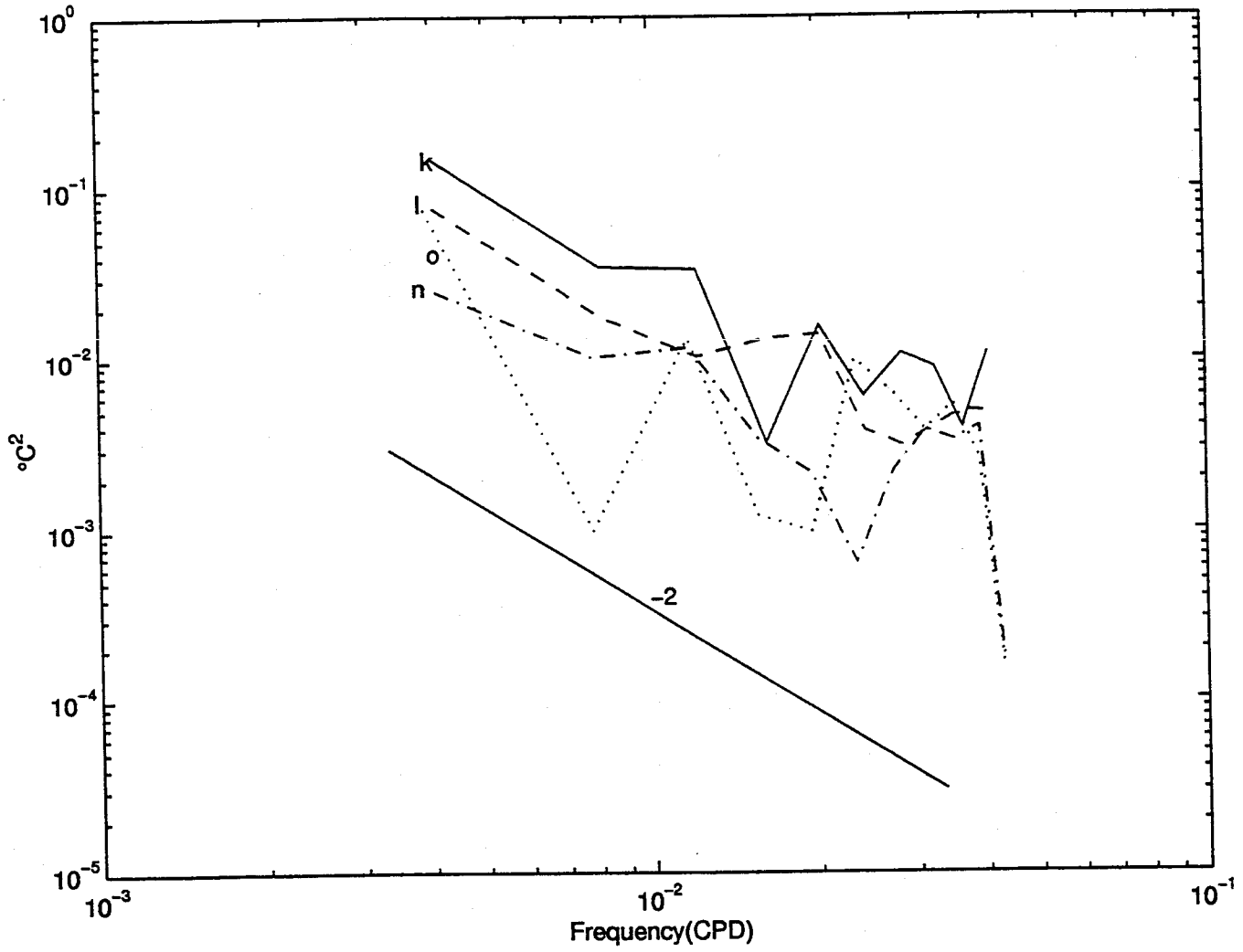

Figure 4-15: Frequency periodogram of rays **k**, **l**, **n**, and **o**.

4.6 Coherence

The coherency spectrum is useful in practice because it provides a nondimensional measure of the correlation between two time series as a function of frequency. From the calculation of spatial coherence at a particular frequency ω, we can derive the coherence scale, which is defined as the separation distance at which the coherence drops to one half.

Using current meter data, Richman [1976] found that the horizontal coherence is a function of frequency and depth. At low frequencies, the horizontal scale in the thermocline is 50–70 km, while the scale in relatively higher frequencies is too small to be determined from the observations. In the deep water the coherence is lower than in the thermocline with an apparent scale of 35 km.

4.7 Anisotropy

The ocean variability is filled with time–varying features with all space and time scales. The ocean variability exhibits different properties at different frequency bands and wavenumber bands, one of which is anisotropy.

Richman et al. [1977] studied the difference between the zonal and meridional kinetic energies in different frequency bands. They concluded that the low frequency band has a distinct tendency for zonality, especially in the thermocline. At shorter periods, the horizontal kinetic energies are isotropic and energy is partitioned equally between potential energy and the two kinetic energy components.

Due to the limitations of oceanographic data, it is still beyond our capability to distinguish the wavenumber spectrum of zonal velocity from that of meridional velocity. Physical oceanography is to some extent a mirror of meteorology, so meteorological results might give us some hints about the ocean. Figure 4.16 shows the wavenumber spectrum of $(g/N)(T-\overline{T})/\overline{T}$ for the winter and summer of 1964. The corresponding

wavenumber spectra of u and v are superimposed as dashed and dotted lines, respectively. It can be seen that there is approximate equipartition among the components of kinetic energy and available potential energy for hemispheric wavenumbers $k > 6$. However, below $k < 5$ or so, there is considerably more energy in the zonal winds. The spectral slope for both u and $(g/N)(T - \overline{T})/\overline{T}$ is about $-1/2$ at hemispheric wavenumbers $k < 5$. On the other hand for v, the wavenumber spectral slope is about $+2$ at hemispheric wavenumbers $k < 5$.

As a starting point, we won't take into account the anistropy in our model for simplicity, we will study the spectra of the horizontal kinetic energy instead of the spectra of zonal and meridional velocity.

4.8 Horizontal inhomogeneity

The ocean variability is not only a function of frequency, horizontal wavenumber and vertical mode but also a function of geography. The statistical properties of the ocean variability (energy level, degree of baroclinicity, ...) change strongly with geographical position [Wunsch 1981, 1997]. This horizontal inhomogeneity is a very important part of the oceanic dynamics. However, this horizontal inhomogeneity makes much of the utility of the wavenumber spectral description invalid. The traditional method to deal with inhomogeneous or nonstationary processes is to try to transform the process into a homogeneous or stationary form. If there is a general trend in the data, one might find the form of the trend and then subtract the function for the trend from the data. Another method is that one can divide the data into several regions in space or several periods in time where the statistical properties are relatively homogeneous or stationary in each region or period. Stammer [1997] made the first frequency/wavenumber analysis as a function of dynamical region.

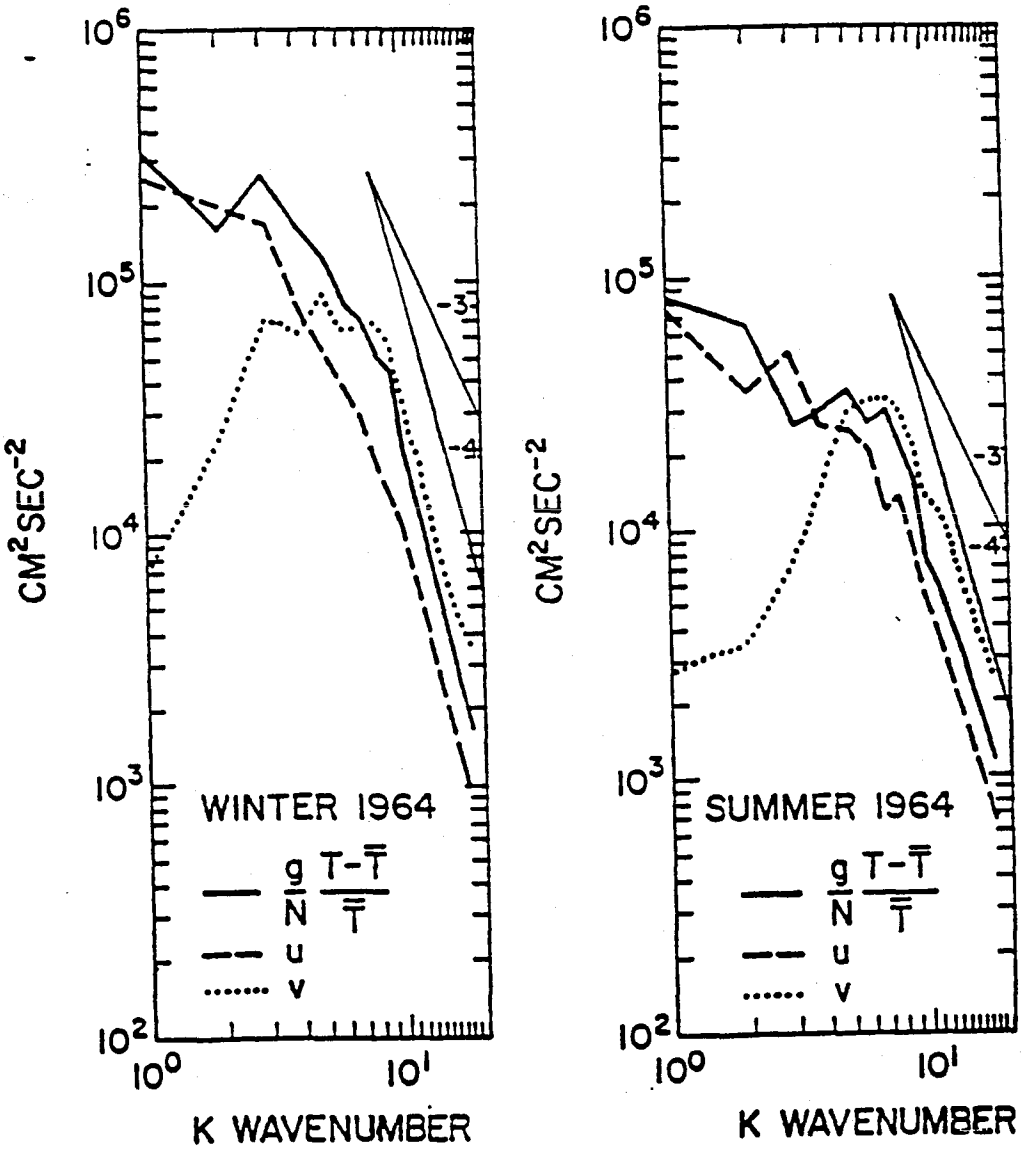

Figure 4-16: The observed wavenumber spectra of u, v and $(g/N)(T-\overline{T})/\overline{T}$ at 40°N and 500 mb for winter and summer 1964 as a function of the hemispheric wavenumber (Charney 1971).

4.8.1 Energy level

The most pronounced feature of horizontal inhomogeneity is the magnitude of the eddy energy. It is well known that the eddy kinetic energy varies strongly with geographical position and that this pattern of geographical inhomogeneity is connected to the pattern of the general ocean circulation. The most energetic eddies occur primarily in the vicinity of strong currents. This is related to the dominant energy source for the eddies. The possible physical parameters for the horizontal inhomogeneity include latitude, proximity to eastern and western boundaries, topography, fronts, etc. In this section, we try to use some mathematical formulations to quantify how the energy level depends on geography.

Figure 4.17.a [taken from Wunsch 1997] shows surface kinetic energy from the current meters in the North Pacific. Figure 4.17.b [taken from Stammer 1997] shows the surface kinetic energy from the altimeter in the North Pacific. Figure 4.17.c shows the surface kinetic energy from the empirical formula, equation 4.18. Figure 4.18 is the same as Figure 4.17 except in the North Atlantic. Altimeter results are from a uniform three–year coverage, spatially averaged over 2°, while the current meter results are of inhomogeneous duration, and are based on an extrapolation to the sea surface. Note the general agreement between them. The most conspicuous point in these figures is that the energy magnitude is inhomogeneous in the ocean. As shown in the figures 4.17.b and 4.18.b, amplitudes of background variability are of the order of 50 cm^2/s^2 in the eastern North Atlantic and as low as 20 cm^2/s^2 in the northern North Pacific. In middle and high latitudes, the maximum amplitudes of K_E are associated with the paths of energetic current systems. In the North Atlantic the maximum occurs in the Gulf Stream with a value of about 2500 cm^2/s^2 and in the North Pacific the maximum is near 4000 cm^2/s^2. Across the middle ocean, the surface eddy kinetic energy changes by roughly two orders of magnitude. In the tropics, the kinetic energy increases very rapidly toward the equator.

The zonal averages between 0° and 360°E of eddy kinetic energy K_E and sea

surface slope $K_{sl} = K_E \sin^2\phi$ are provided as a function of latitude in figure 4.19. The zonal averaged K_E decreases from maximum amplitude near the equator to minimum amplitude in high latitudes. In terms of K_{sl}, values remain almost constant in the low latitudes between $25°S$ and $25°N$, which implies equatorwards of 25° the zonally averaged K_E is proportional to $1/\sin^2\phi$.

According to the figure 4.17 (a) and (b), we can regard the surface eddy kinetic energy in the North Pacific as being composed of four parts: (1) the background part, (2) the low latitude part (south of the energetic currents) where $K_E \propto (1/\sin^2\theta)$, (3) the high energy source with a center around (35°N, 150°E), and (4) the low energy area in the north North Pacific. According to these, we can express the surface eddy kinetic energy in the North Pacific with the following empirical formula

$$\begin{aligned}\hat{E}_{kp}(\phi,\lambda,z=0) &= 30+\frac{32}{\sin^2\phi}+1000\exp\{-[\frac{(\lambda-50)^2}{900}+\frac{(\phi-35)^2}{50}]\} \\ &\quad -800\exp\{-[\frac{(\lambda-190)^2}{1600}+\frac{(\phi-42)^2}{200}]\}, \qquad (4.18)\end{aligned}$$

where λ is the longitude from 0 to 360° E, ϕ is the latitude from 10 to 60° N, and the units of $\hat{E}_{kp}$ are cm^2/s^2.

The pattern of the surface eddy kinetic energy in the North Atlantic is different from that of the North Pacific. There is a strong jet on the western side of the Atlantic ocean and there are two low energy areas in the eastern Atlantic. South of $25°N$ the energy increases toward the equator. Similarly we can express the surface eddy kinetic energy in the North Atlantic as

$$\begin{aligned}\hat{E}_{ka}(\phi,\lambda,z=0) &= 50+\frac{35}{\sin^2\phi}+1000\exp\{-[\frac{(\lambda-305)^2}{400}+\frac{(\phi-43)^2}{80}]\}- \\ 280\exp\{-[\frac{(\lambda-320)^2}{2000}+\frac{(\phi-16)^2}{200}]\} &- 160\exp\{-[\frac{(\lambda-320)^2}{900}+\frac{(\phi-16)^2}{50}]\} \qquad (4.19)\end{aligned}$$

where the units are cm^2/s^2.

The results from equations (4.18) and (4.19) are drawn in figure 4.17.c and 4.18.c,

respectively. As shown in figure 4.17 and 4.18, equations (4.18) and (4.19) are reasonable fits to the general pattern of the corresponding observations.

The reader is reminded that the observed frequency and wavenumber spectral shape is independent of location and depth, only the energy level of the frequency and wavenumber spectra depends on location and depth. If we integrate the surface kinetic energy frequency (wavenumber) spectrum of a relatively homogeneous region with respect to frequency (wavenumber), we will get the surface kinetic energy for that region. Therefore, the energy level of the frequency and wavenumber spectra is higher in the regions of higher kinetic energy. In chapter 5, we will relate the geography–dependent part of our energy density model to the empirical formulas (4.18) and (4.19). The vertical structure of horizontal kinetic energy will be discussed in section 4.9.

4.8.2 Others

In addition to the strong geographic variation of the magnitude of eddy kinetic energy, there are still many other factors depending on space, as we mentioned previously. First, the degree of baroclinicity is inhomogeneous in space. As we will discuss in detail in the next section, the percentage of the kinetic energy in the first three modes varies with geography. Second, the cutoff wavenumber k_0 in the slope wavenumber spectrum in figure 4.5 decreases from high latitude toward the equator. Third, the buoyancy frequency $N(z)$ changes with latitude and longitude especially above 1 km. If the interior $N(z)$ varies on spatial scales for which the WKBJ approximation is not valid, a host of complex scattering interactions become possible. Whether such processes are important in the ocean is still not clear [Wunsch and Stammer 1997]. Last but not least, the vertical gradient of mean temperature as well as the depth of the ocean can exhibit strong changes in space.

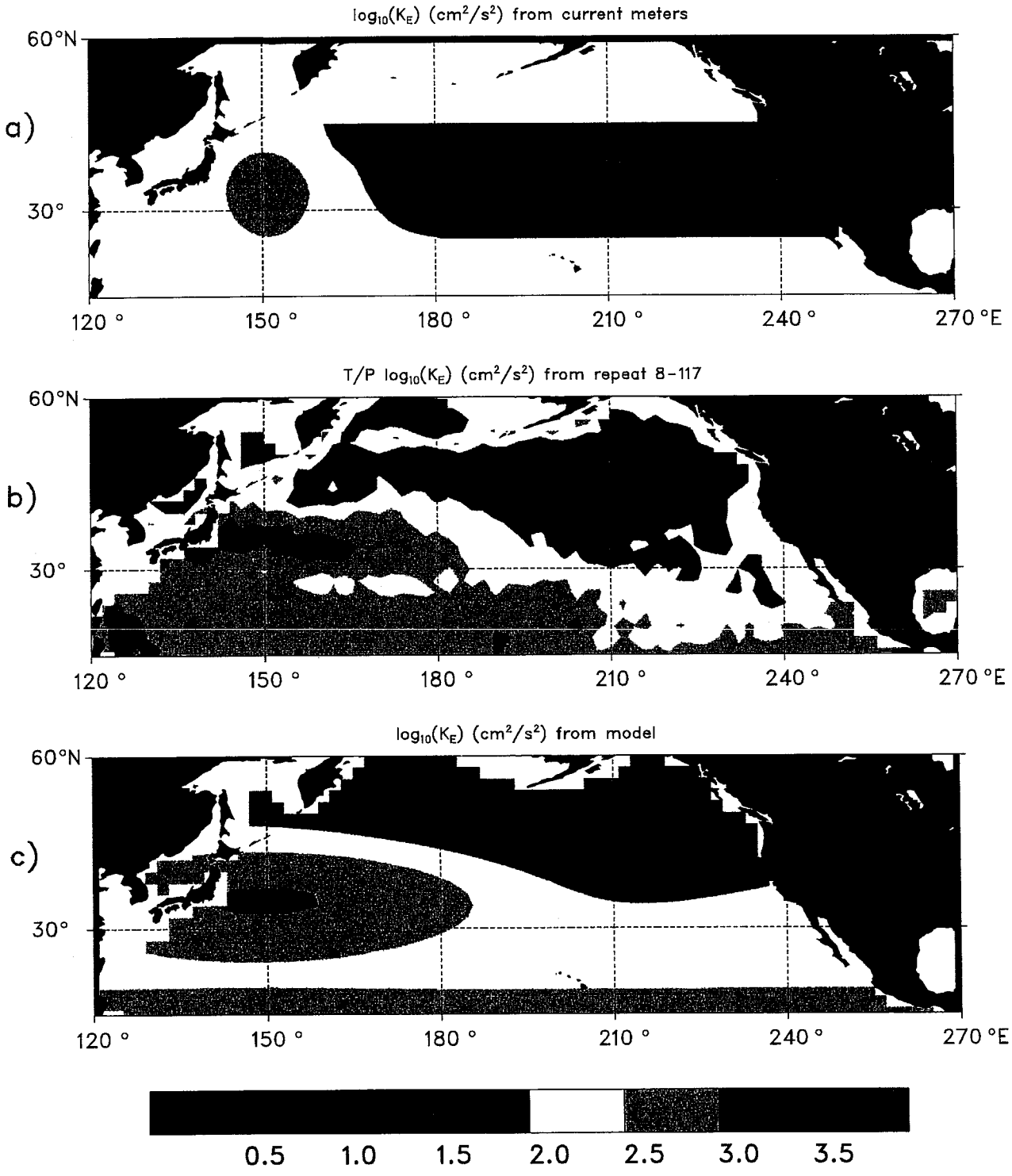

Figure 4-17: Surface eddy kinetic energy in the region of North Pacific. (a) from the current meters (Wunsch 1997) (b) from TOPEX/POSEIDON data (Stammer 1997) (c) from the empirical formula.

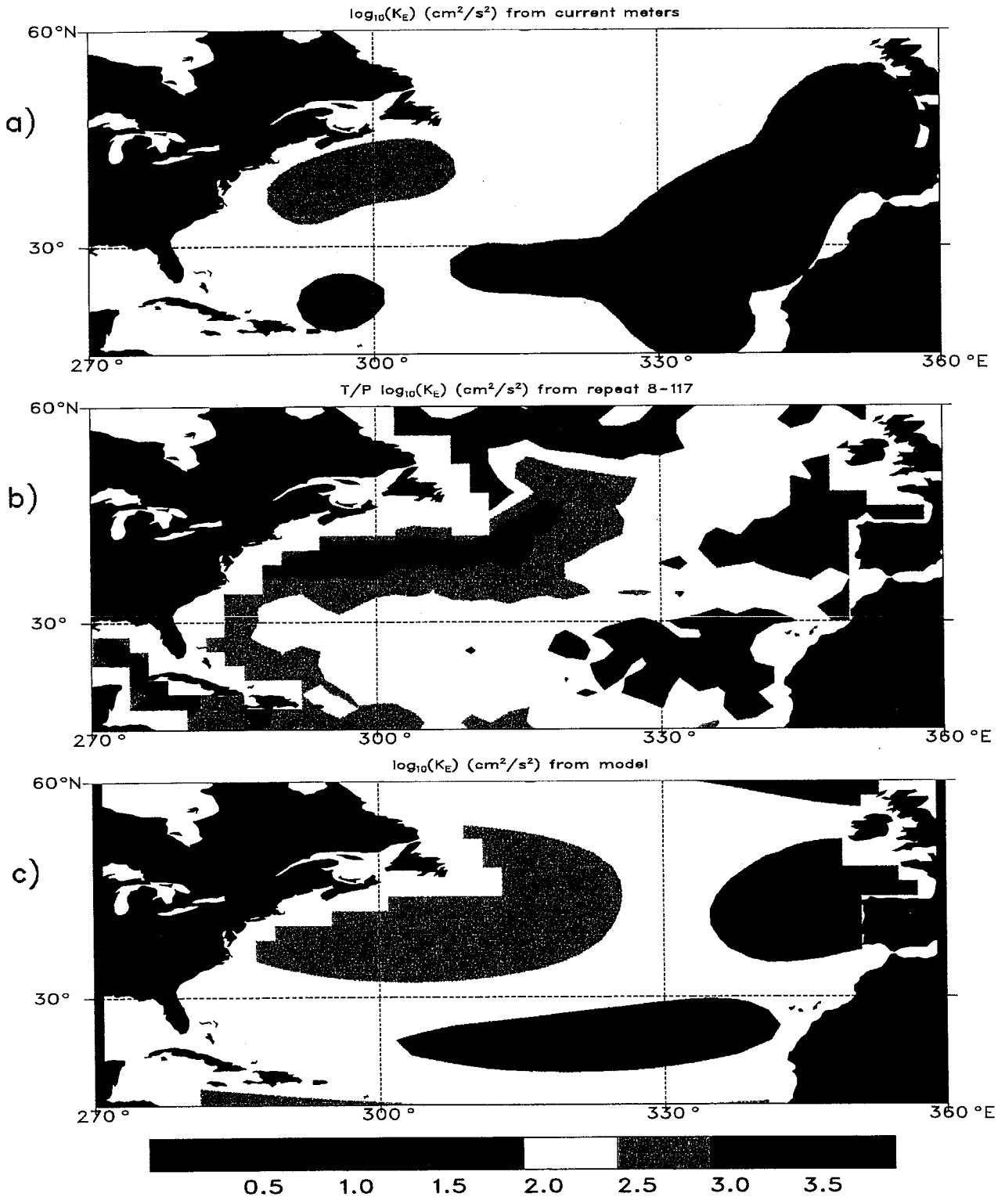

Figure 4-18: Same as in Figure 4-17 except for North Atlantic.

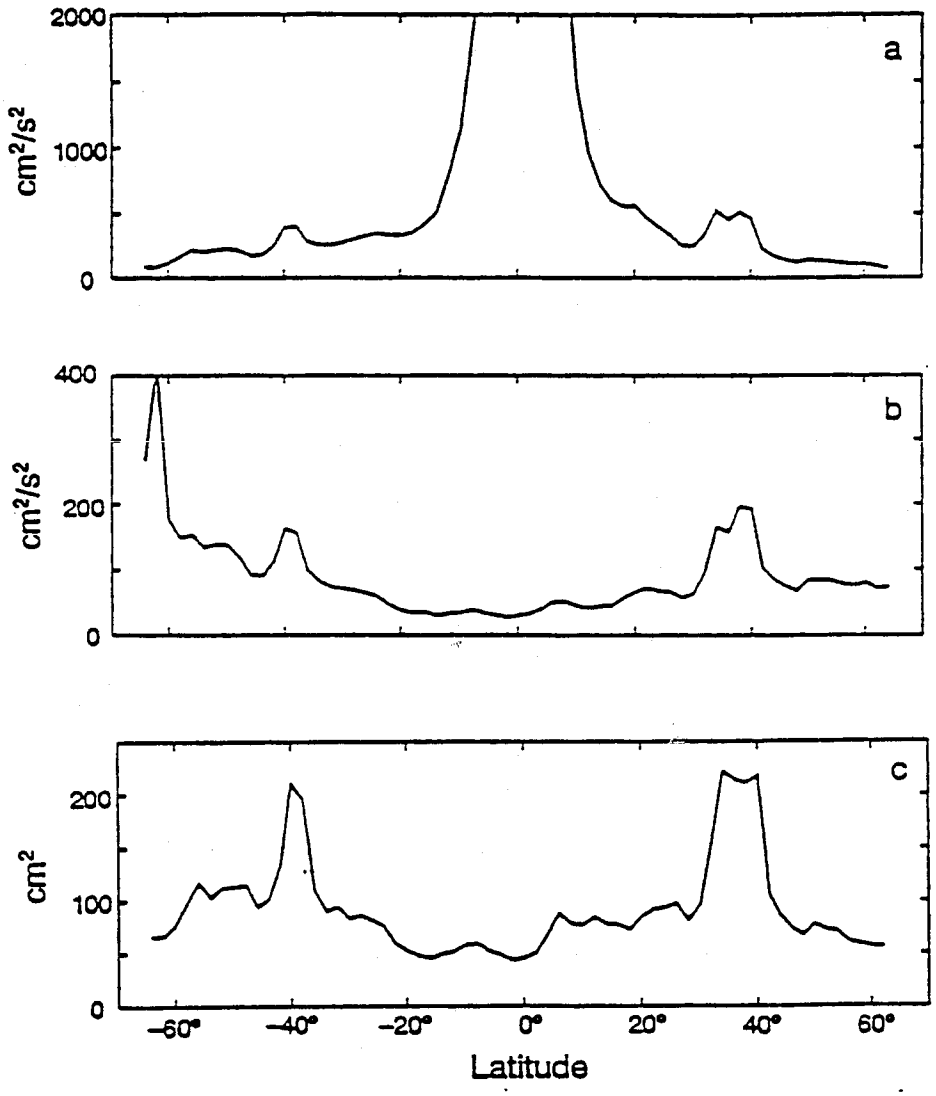

Figure 4-19: Zonal averages between 0° and 360°E of (a) K_E, (b) K_{sl} and (c) SSH variances, plotted against latitude (Stammer 1997).

4.9 Vertical structure of kinetic energy

Schmitz [1978, 1988, 1996] studied the vertical distribution of kinetic energy at different sites in the Atlantic and Pacific. He concluded that the vertical profile for kinetic energy is independent of geography as a first approximation across the entire mid-latitudes, with amplitudes generally decreasing eastward and away from the western boundary current. Figure 4.20 is an example of the vertical profile of kinetic energy at some key sites. The eddy kinetic energy K_E drops exponentially from the surface to the depth of 1.2 km, then remains almost constant within the deep water. Given the strong spatial inhomogeneity in properties of the eddy field, the observation that the relative vertical K_E distribution is nearly the same in widely varying locations might be especially significant. These similarities in vertical structure might imply similarities in origin and/or dynamics.

Wunsch [1997] systematically studied the question: what is the partition throughout the water column of the kinetic energy of time–varying motions amongst the dynamical modes? Figure 4.21 and 4.22 [taken from Wunsch 1997] show maps of the logarithm of the kinetic energy per unit depth and of the approximate percentage of the kinetic energy found in the barotropic and first two baroclinic modes in the North Pacific and the North Atlantic. In general, the barotropic and first baroclinic modes dominate the water column average kinetic energies except in the Tropics. Crudely speaking, the North Pacific kinetic energy is about 35% contained in the barotropic mode and about 55% in the first baroclinic mode. The North Atlantic is on average about 40% in the barotropic and 50% in the first baroclinic mode in the middle ocean. Near the Gulf stream, the motions are more barotropic in character than in the records obtained elsewhere. Just south of the Gulf Stream near 90% of the kinetic energy is contained in the barotropic mode. Near the equator the higher modes become important.

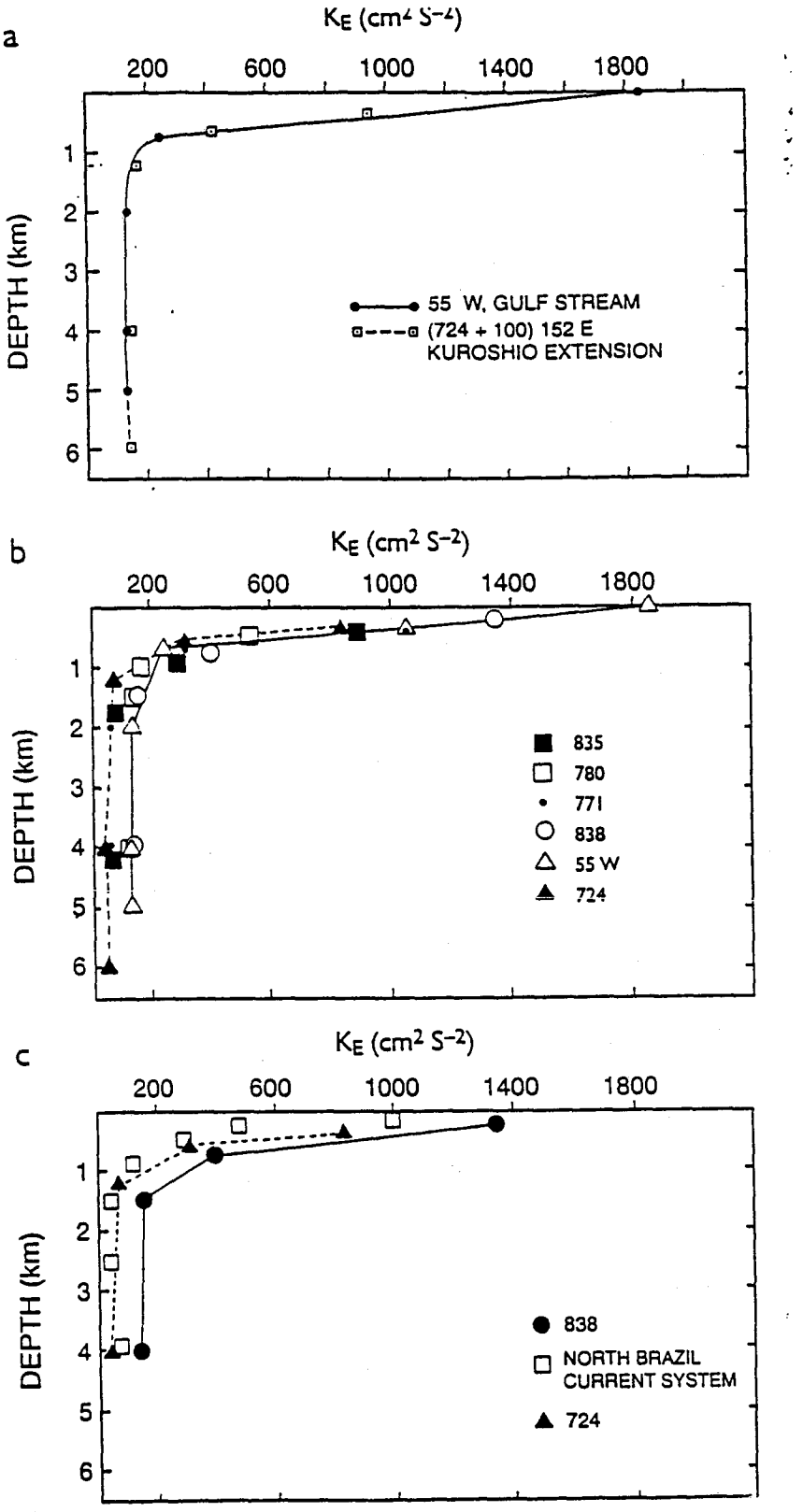

Figure 4-20: (a) The vertical distribution of K_E at key sites in the Gulf Stream (along 55 W) and in the Kuroshio(mooring 724), (b) at sites in the Gulf Stream (moorings 771 and 780 and near 55 W),Kuroshio, and Agulhas Retroflection(moorings 835and 838, and (c) including a site near the North Brazil Current (Schmitz 1996).

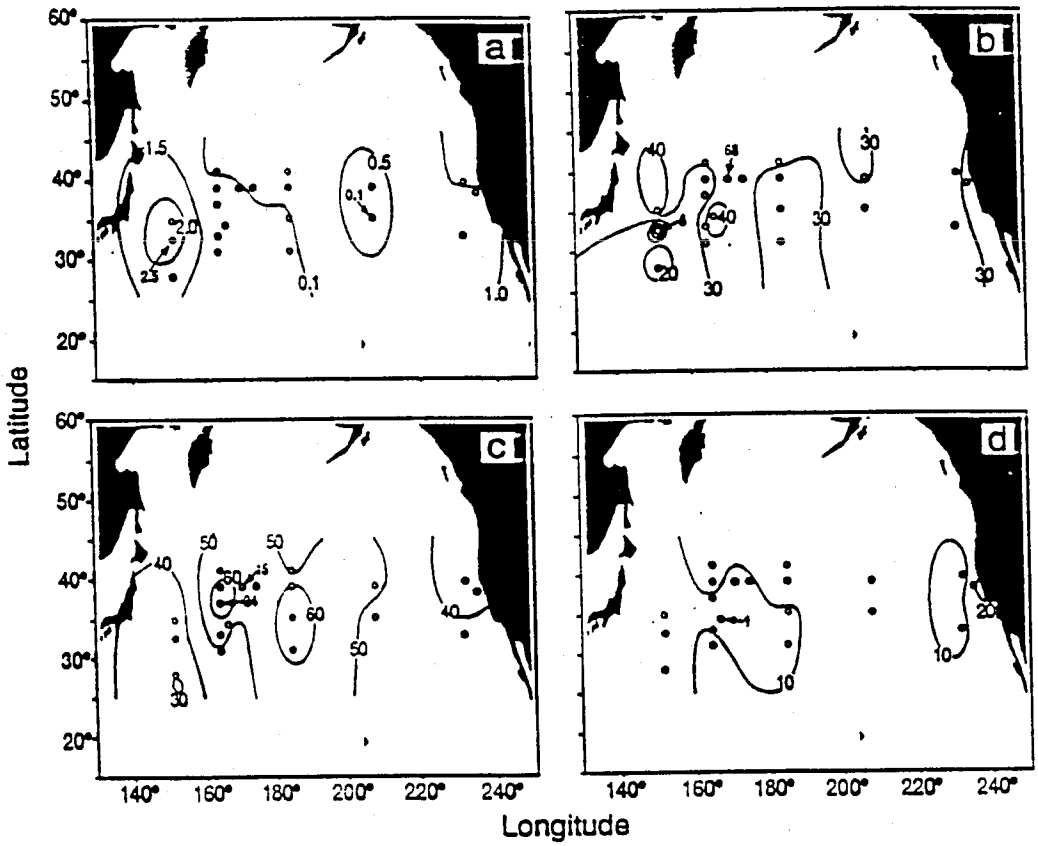

Figure 4-21: (a) Log_{10} of the water column average kinetic energy per unit mass in the North Pacific Ocean. (b) Percentage of water column average kinetic energy per unit mass found in the barotropic mode. (c) Percentage of water column average kinetic energy per unit mass found in the first baroclinic mode. (d) Percentage of water column average kinetic energy per unit mass found in the second baroclinic mode (Wunsch 1997).

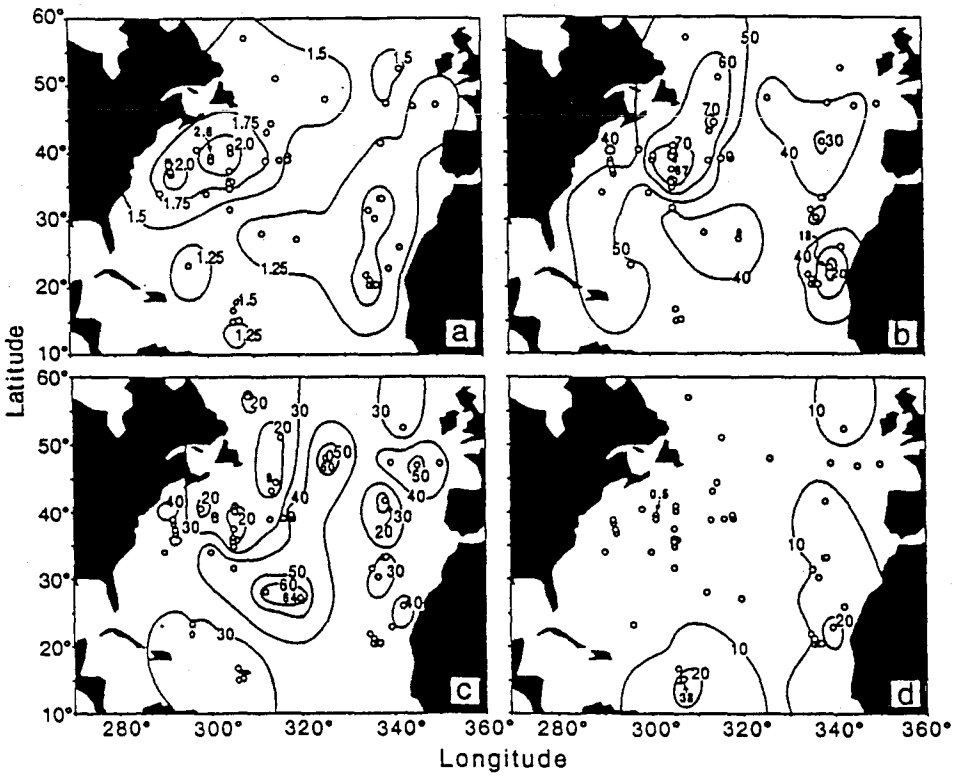

Figure 4-22: (a-d) same as in figure 4.19 except for the North Atlantic (Wunsch 1997).

4.10 Summary

The ocean variability is very complicated. It occurs at all time and space scales and it is spatially inhomogeneous as well as anisotropic. In spite of this complexity, the major outcome from this chapter is that over most of the ocean, the ocean variability shows strikingly universal characteristics. The frequency and wavenumber spectral shape of temperature and horizontal velocities is independent of location and depth. The largest variations in frequency and wavenumber spectra appear to be related to the geographic variation of the amplitude of the eddy energy. To zero order, the low frequency oceanic variability can be summarized as follows

(1) the frequency spectrum for temperature and velocity:

$$F(\omega) \propto \begin{cases} \omega^{-1/2} & \text{if } \omega < \omega_0 \\ \omega^{-2} & \text{if } \omega > \omega_0 \end{cases} \tag{4.20}$$

where ω_0 is about 0.01 cycles/day.

(2) the horizontal wavenumber spectrum for temperature and velocity:

Both the kinetic energy wavenumber spectrum and the temperature wavenumber spectrum have a transitional point at a wavelength of about 400 km. At wavelengths longer than 400 km, the wavenumber spectrum of kinetic energy and temperature follows a relation of $k^{+3/2}$ and a relation of $k^{-1/2}$, respectively. At wavelengths shorter than 400 km, the temperature wavenumber spectrum follows a relation of k^{-3}. The kinetic energy wavenumber spectrum follows a k^{-1} relation at wavelengths between 150 km and 400 km, and a k^{-2} relation at shorter wavelengths. The relationship between the observed kinetic energy wavenumber spectrum and temperature wavenumber spectrum implies that for large scale and low frequency varibility, the temperture and the velocity are related to each other through the thermal wind relation.

(3) the vertical structure of horizontal kinetic energy:

As discussed by Wunsch [1997], to a first good approximation the vertical structure of eddy kinetic energy can be simply represented by the barotropic and first baroclinic modes in the middle ocean. Roughly speaking, the vertical partitioning of the kinetic

energy in the barotropic and the first baroclinic modes is equal.

(4) the energy level:

The energy magnitude shows strong inhomogeneity in space and typically the energy level increases toward the western boundary and the equator. The general pattern of the surface eddy kinetic energy in the North Pacific and the North Atlantic can be represented empirically by the equations (4.18) and (4.19), respectively.

Chapter 5

Energy distribution in K, ω space

In previous chapters, we have derived the frequency and wavenumber spectra for the model and we have obtained a zero order description of low frequency oceanic variability based on various observations. Now, we come to answer the question we raised in the introduction: whether it is possible to find a single model $\Phi(K, \omega, n)$ for each mode so that each model spectrum can fit the corresponding observation. For the time being, we do not know whether $\Phi(K, \omega, n)$ really exists or not. In GM's model, $\Phi(K, \omega, n)$ does exist. Moreover, there is a surprising universality to the value of the energy level (mostly within a factor two) [Munk 1981]. However, the strong spatial variability of energy magnitude, buoyancy frequency and vertical gradient of mean temperature as indicated in chapter 4 suggests that the spectral representation in the wavenumber domain isn't appropriate. In order to overcome the difficulties associated with spatial inhomogeneity, we can break the global ocean into several regions where the statistical properties do not vary too much with geography. For example, in the open ocean far from intense currents the energy magnitude is quasi–homogeneous and the vertical gradient of mean temperature and buoyancy frequency at depth below 1000m are relatively uniform.

Because of the spatial inhomogeneity, we must modify the universal form $\Phi(K, \omega, n)$ to a regional form $\Phi(K, \omega, n, \phi, \lambda)$ so that the model spectrum can fit the corresponding observation. The reader is reminded that the definition of $\Phi(K, \omega, n)$ is given by equation (3.17). Here we don't take the direction of the spectrum into consideration.

The investigation of the directional property of the spectrum is in progress. We suppose that $\Phi(K, \omega, n, \phi, \lambda)$ exists and a convenient representation of $\Phi(K, \omega, n, \phi, \lambda)$ for each mode is

$$\Phi(K, \omega, n, \phi, \lambda) = C_n(K) D_n(\omega) E_0(n) I(\phi, \lambda). \tag{5.1}$$

Here $C_n(K)$ represents the wavenumber spectral shape, $D_n(\omega)$ stands for the frequency spectral shape, $E_0(n)$ is a constant associated with each mode which will determine how the energy is divided among vertical modes and $I(\phi, \lambda)$ is the spatial function which represents how the energy level depends on space. In this chapter, we will decide on the form of $C_n(K)$, $D_n(\omega)$, $E_0(n)$ and $I(\phi, \lambda)$ according to observations.

Because most of the region is dominated by the first few modes as seen in the last chapter, we just include the barotropic and first two baroclinic modes in our model: n=0, 1, 2. When we try to estimate the total energy spectrum from the individual modes at an arbitrary depth, we will face the problem of "modal coupling". Wunsch [1997] studied this problem in detail. Here we simply assume that each mode is independent of all other modes in our model.

It has become conventional to think of and to present frequency spectra only for positive frequency. Actually, the part on the negative side of the frequency axis also exists. The spectrum at the positive frequency and the negative frequency is symmetric about $\omega = 0$ so that the frequency spectrum at the positive frequency contains all the available information and the total variance is twice that of positive frequency. We will double the signal content for the positive frequency in both the model and observation, essentially folding over the negative frequencies onto the positive and adding. The wavenumber spectrum will be handled similarly.

5.1 Fitting $\Phi(K, \omega, n, \phi, \lambda)$ from observations

In this section, we will decide what the key parameters of $\Phi(K, \omega, n, \phi, \lambda)$ are needed so that the model spectrum can fit the corresponding observation. First of all, because

the observed frequency and wavenumber spectral shape is independent of depth, we infer that the frequency and wavenumber spectral shape of each mode is approximately identical. Therefore, we will decide on the form of $C_n(K)$ and $D_n(\omega)$ so that the model frequency and wavenumber spectral shape of each mode is the same as the observed frequency and wavenumber spectral shape.

Choosing the form of $C_n(K)$ to fit the observed wavenumber spectra

Substitution of equation (5.1) into (3.52) and the assumption that there is no modal coupling at each arbitrary depth gives the kinetic energy spectrum

$$F_k(K,z,\phi,\lambda) = I(\phi,\lambda)\sum_{n=0}^{n=3} P_n^2(z)E_0(n)[2\int_0^{+\infty} D_n(\omega)d\omega]\frac{K^2}{K^2+f^2r_n^2}C_n(K). \quad (5.2)$$

where the factor of 2 before $D_n(\omega)$ arises since we have folded over the negative frequencies onto the positive ones.

The corresponding dimensional form is

$$\hat{F}_k(K,z,\phi,\lambda) = U^2LF_k(K,z,\phi,\lambda) = 1\times 10^4 F_k(K,z,\phi,\lambda) \quad (5.3)$$

where the units are $\mathrm{cm}^2/\mathrm{s}^2/\mathrm{CPK}$.

Because the barotropic eigenvalue $r_0 = 0$, the wavenumber spectral shape of the barotropic mode is decided by $C_0(K)$. According to the observations, we choose a simple form:

$$C_0(K) = \begin{cases} C_0K^{3/2} & \text{if } K < K_0 \\ K^{-2} & \text{if } K > K_0\ , \end{cases} \quad (5.4)$$

where $K_0 = \hat{K}_0L = 0.33$ corresponds to the nondimensional wavenumber maximum energy. In order for $C_0(K)$ to be continuous at K_0, $C_0 = 48.44$. From (5.4), we get

$$\int_0^{\infty} C_0(K)dK = 4.24. \quad (5.5)$$

For the baroclinic modes, the shape of the wavenumber spectrum is determined by $C_n(K)K^2/(K^2+f^2r_n^2)$. To fit the observed wavenumber spectra, we choose for

both n=1 and n=2

$$C_n(K) = \begin{cases} 15.99K^{-1/2} & \text{if } K < K_0 \\ K^{-3} & \text{if } K > K_0 \ . \end{cases} \tag{5.6}$$

The above equation yields for the baroiclinic modes: n=1 and n=2

$$\int_0^\infty C_n(K)dK = 22.96. \tag{5.7}$$

Choosing the form of $D_n(\omega)$ to fit the observed frequency spectra

Substitution of (5.1) into (3.51) yields

$$F_k(\omega, z, \phi, \lambda) = I(\phi, \lambda) \sum_{n=0}^{n=2} P_n^2(z) E_0(n) [\int_0^\infty \frac{K^2}{K^2 + f^2 r_n^2} C_n(K)dK] 2D_n(\omega). \tag{5.8}$$

The corresponding dimensional form is

$$\hat{F}_k(\omega, z, \phi, \theta) = U^2 T F_k(\omega, z, \phi, \theta) = 16.5 F_k(\omega, z, \phi, \lambda), \tag{5.9}$$

where the units are $cm^2/s^2/CPD$.

According to the observation of the frequency spectra, we choose for n=0 to n=2

$$D_n(\omega) = \begin{cases} 14880\omega^{-1/2} & \text{if } \omega < \omega_0 \\ \omega^{-2} & \text{if } \omega > \omega_0 \end{cases} \tag{5.10}$$

where the nondimensional parameter $\omega_0 = \hat{\omega_0} T = 0.00165$.

The above equation gives for the three modes: n=0 to n=2

$$\int_0^\infty D_n(\omega)d\omega = 1816. \tag{5.11}$$

The energy level of each mode

The total kinetic energy per unit surface area for each mode is:

$$\begin{aligned} K_h(n,\phi,\lambda) &= \int\int F_k(K,n,z,\phi,\lambda)dKdz = \int\int F_k(\omega,n,z,\phi,\lambda)d\omega dz \\ &= I(\phi,\lambda)E_0(n)[\int_0^\infty \frac{K^2}{K^2+f^2r_n^2}C_n(K)dK][2\int_0^\infty D_n(\omega)d\omega] \end{aligned} \quad (5.12)$$

Substitution of (5.4), (5.6) and (5.10) into the above equation gives

$$K_h(n,\phi,\lambda) = \begin{cases} 15400E_0(0)I(\phi,\lambda); & \text{n=0} \\ 4800E_0(1)I(\phi,\lambda); & \text{n=1} \\ 1400E_0(2)I(\phi,\lambda); & \text{n=2} \end{cases} \quad (5.13)$$

As seen in chapter 4, the vertical structure of eddy kinetic energy can be simply represented by the barotropic and first two baroclinic modes in the middle ocean and roughly speaking, the kinetic energy of the three modes is in the ratio of $1:1:1/2$. Accordingly, if we choose $E_0(0)=1.0$, then $E_0(1)=3.2$ and $E_0(2)=5.4$.

Choosing $I(\phi,\lambda)$ to fit the observed surface kinetic energy

The surface kinetic energy for the model is

$$\begin{aligned} E_k(\phi,\lambda,z=0) &= I(\phi,\lambda)\sum_{n=0}^{n=2}P_n^2(z=0)E_0(n)[\int_0^\infty \frac{K^2}{K^2+f^2r_n^2}C_n(K)dK][2\int_0^\infty D_n(\omega)d\omega] \\ &= 5.4\times10^5 I(\phi,\lambda). \end{aligned} \quad (5.14)$$

The corresponding dimensional form is

$$\hat{E}_k(\phi,\lambda,z=0) = U^2E_k(\phi,\lambda,z=0) = 5.4\times10^7 I(\phi,\lambda), \quad (5.15)$$

where the units are cm^2/s^2.

The above equation yields

$$I(\phi,\lambda) = \frac{\hat{E}_k(\phi,\lambda,z=0)}{5.4\times10^7}. \quad (5.16)$$

In chapter 4, we derived an empirical formula for the surface kinetic energy

$\hat{E}_k(\phi, \lambda, z = 0)$. The empirical formulas for the surface kinetic energy in the North Pacific and the North Atlantic are given by equations (4.18) and (4.19), respectively.

The wavenumber spectrum of the temperature

Substitution of equation (5.1) into (3.54) gives

$$F_\theta(K, z, \phi, \lambda) = I(\phi, \lambda)\mu^2 \sum_{n=1}^{n=2} E_0(n) Q_n^2(z) [2 \int_0^\infty D_n(\omega) d\omega] \frac{2 f^2 r_n^2}{K^2 + f^2 r_n^2} C_n(K). \quad (5.17)$$

The corresponding dimensional formula is

$$\hat{F}_\theta(K, z, \phi, \lambda) = \Theta^2 L F_\theta(K, z, \phi, \lambda). \quad (5.18)$$

Substitution of equation (2.83) and (5.17) into the above equation gives

$$\begin{aligned} \hat{F}_\theta(K, z, \phi, \lambda) &= (TW)^2 L I(\phi, \lambda) (\frac{\partial \theta_0}{\partial \hat{z}})^2 \sum_{n=1}^{n=2} [2 \int_0^\infty D_n(\omega) d\omega] E_0(n) Q_n^2(z) \frac{2 f^2 r_n^2}{K^2 + f^2 r_n^2} C_n(K) \\ &= 1.5 \times 10^9 I(\phi, \lambda) (\frac{\partial \theta_0}{\partial \hat{z}})^2 \sum_{n=1}^{n=2} E_0(n) Q_n^2(z) \frac{2 f^2 r_n^2}{K^2 + f^2 r_n^2} C_n(K), \quad (5.19) \end{aligned}$$

where the units of $\partial \theta_0 / \partial \hat{z}$ are °C/m and the units of $\hat{F}_\theta(K, z, \phi, \lambda)$ are °C^2/CPK.

The frequency spectrum of the temperature

Substitution of (5.1) into (3.53) yields

$$F_\theta(\omega, z, \phi, \lambda) = I(\phi, \lambda)\mu^2 \sum_{n=1}^{n=2} E_0(n) Q_n^2(z) [\int_0^\infty \frac{2 f^2 r_n^2}{K^2 + f^2 r_n^2} C_n(K) dK] 2 D_n(\omega). \quad (5.20)$$

The corresponding dimensional formula is

$$\hat{F}_\theta(\omega, z, \phi, \lambda) = \Theta^2 T F_\theta(\omega, z, \phi, \lambda). \quad (5.21)$$

Substitution of equation (2.83) and (5.20) into the above equation gives

$$\hat{F}_\theta(\omega, z, \phi, \lambda) = (TW)^2 T I(\phi, \lambda) (\frac{\partial \theta_0}{\partial \hat{z}})^2 \sum_{n=1}^{n=2} E_0(n) Q_n^2(z) [\int_0^\infty \frac{2 f^2 r_n^2}{K^2 + f^2 r_n^2} C_n(K)] 2 D_n(\omega)$$

$$= 683I(\phi,\lambda)(\frac{\partial\theta_0}{\partial\hat{z}})^2\sum_{n=1}^{n=2}E_0(n)Q_n^2(z)[\int_0^\infty \frac{2f^2r_n^2}{K^2+f^2r_n^2}C_n(K)]2D_n(\omega) \quad (5.22)$$

where the units of $\partial\theta_0/\partial\hat{z}$ are °C/m and the units of $\hat{F}_\theta(\omega,z,\phi,\lambda)$ are °C^2/CPD.

The frequency spectrum for tomographic data

In chapter 3, we derived the frequency spectrum for the range–averaged temperature in equation (3.55). However, the real tomographic data is depth–averaging as well as the range–averaged, so we need to modify (3.55) to take into account the depth–averaged effect. The ATOC data were depth averaged from 0 to 1000m. The corresponding spectrum is

$$F_{atoc}(\omega) = I(\phi,\lambda)\sum_{n=1}^{n=2}E_0(n)[\frac{1}{h}\int_{-h}^{0}\mu Q_n(z)dz]^2][\int\int\frac{2f^2r_n^2}{K^2+f^2r_n^2}\frac{C_n(K)}{2\pi K}W(k,L_a)dkdl]2D_n(\omega) \quad (5.23)$$

where h=1000m/4500m=0.222 is the nondimensional depth and $K=\sqrt{k^2+l^2}$.

The corresponding dimensional frequency spectral formula is:

$$\hat{F}_{atoc}(\omega) = \Theta^2 T F_{atoc}(\omega). \quad (5.24)$$

Substitution of equation (2.83) and (5.23) into the above equation yields

$$\hat{F}_{atoc}(\omega) = 683I(\phi,\lambda)\sum_{n=1}^{n=2}E_0(n)[\frac{1}{h}\int_{-h}^{0}\frac{\partial\theta_0}{\partial\hat{z}}Q_n(z)dz]^2[\int\int\frac{2f^2r_n^2C_n(K)}{(K^2+f^2r_n^2)2\pi K}\frac{sin^2(kL_a/2)}{(kL_a/2)^2}dkdl]2D_n \quad (5.25)$$

where the units of $\partial\theta_0/\partial\hat{z}$ are °C/m and the units of $\hat{F}_\theta(\omega,z,\phi,\lambda)$ are °C^2/CPD.

We must be aware that

(1) The kinetic energy wavenumber spectrum (5.2) is useful only in the regions where the energy magnitude is relatively homogeneous.

(2) The conditions for the temperature wavenumber spectrum (5.19) holding are more strict. There are two parameters in equation (5.19): the energy level and the vertical gradient of mean temperature, both of which change strongly in space in the global ocean. So the equation (5.19) is appropriate only in areas where both

the energy magnitude and the vertical gradient of mean temperature are relatively uniform.

(3) The conditions for the frequency spectrum of tomographic measurements are the same as those for the temperature wavenumber spectrum.

5.2 Model and data comparison

In the above section, we have specified the formula for each component of $\Phi(K, \omega, n, \phi, \lambda)$: $C_n(K)$, $D_n(\omega)$, $E_0(n)$ and $I(\phi, \lambda)$, based on different observations. There might, however, be some incompatibilities among different observations. For example, in our model we specify the vertical structure according to the vertical structure of the kinetic energy of the observations. However, we don't know whether the vertical stucture of the temperature is consistent with that of the kinetic energy. In this section, we will make model/data comparisons to see whether each model spectrum can fit the corresponding observation with our specified regional energy density $\Phi(K, \omega, n, \phi, \lambda)$.

Kinetic energy wavenumber spectrum

The model and observed surface kinetic energy wavenumber spectra are plotted in figure 5.1. The observed spectrum is from 10° × 10° areas between 30° and 40° N with a center longitude at 330° E. The energy level in this area is relatively uniform. According to the equation (4.19), the average value $\hat{E}_k(\phi, \lambda, z = 0)$ in this area is about 250 cm^2/s^2. As shown in figure 5.1, the model spectrum fits the observation quite well except at wavenumbers higher than 0.01 CPK. The high wavenumber tail with a k^{+1} relation in the observed wavenumber spectrum is dominated by noise rather than ocean signal [Wunsch and Stammer 1995]. The model and observed spectrum in figure 5.1 both have a maximum in energy at the cutoff wavelength of about 400 km, with roughly $k^{3/2}$ and k^{-2} relations toward longer and shorter wavelengths.

Temperature wavenumber spectrum

The observed temperature wavenumber spectrum in figure 5.2 is from the XBT data in the eastern North Pacific described in section 4.3.2. The surface eddy kinetic

energy along this XBT line is relatively homogeneous. The mean value of surface kinetic energy from equation (4.18) is about 150 cm^2/s^2. As shown in figure 4.7.(a), the vertical gradient of mean temperature changes strongly in space especially in the upper ocean. Because the depth of this XBT data is limited to 850 m, we will compare the model spectrum with that of observations at the depth of 800m. The vertical gradient of mean temperature along the XBT line at this depth changes relatively less sharply. The mean value of $\partial\theta_0/\partial\hat{z}$ is about 0.0028 °C/m, and the corresponding standard deviation is 0.0005 °C/m. With this choice of energy level and vertical gradient of mean temperature, we plot the model temperature wavenumber spectrum in figure 5.2. In general, the model spectrum fits the observed spectrum quite well. The obvious deviation is that at wavenumbers larger than 0.008 CPK, where the slope of the observed spectrum is steeper than that of the model. As we have mentioned in section 4.3, the steeper slope at wavenumbers higher than 0.008 CPK in this observed wavenumber spectrum between San Francisco and Hawaii might be due to deviations in the ship track.

Frequency spectrum of kinetic energy and temperature

Here we analyze one set of current meter data which is located at (33.2° N, 338.1° E) inside the low energy area in the eastern North Atlantic. It has current and temperature meters at nominal depths of 560, 1160 and 3050 (m). From equation (4.19), $\hat{E}_k(33.2°N, 338.1°E, z = 0) = 108 cm^2/s^2$. Equation (5.16) yields $I(33.2°N, 338.1°E) = 2 \times 10^{-6}$. The vertical gradients of the mean temperature at depths of 560, 1160 and 3050 (m) are 0.0127, 0.0064 and 0.0007 °C/m, respectively. We plot the model and observed spectra in figure 5.3. The vertical profile of the kinetic energy is shown in figure 5.4. The general agreement between the model and the observed spectra is quite pleasing. The most conspicuous lack of agreement between the model and the observation is in figure 5.3.1, the energy level of model temperature spectrum at 560 m is about 2 times higher than that of the corresponding observed spectrum. Several possibilities exist for rationalizing this difference. One of which is that we have assumed the idealized exponential profile for the buoyancy frequency N(z) However, in the real ocean the buoyancy frequency changes in space especially

in the upper ocean. The buoyancy frequency determines the vertical structure of the velocity, hence influences the spectral energy level. A second possibility is that the idealized and universal modal partitioning in the model is invalid. A third possibility is that there are also some errors on the vertical gradient of mean temperature, and the energy level of the spectrum is proportional to the square of the the vertical gradient of mean temperature. The vertical profile of the kinetic energy–exponential decay in the upper ocean and almost constant below 1000 m–agrees quite well with those observed by Schmitz.

Frequency spectrum of tomographic data

As discussed in section 3.5, the tomographic data acts as a low–pass filter and the path-band width of the filter is related to the length of the acoustic ray path. Because we have specified the form of $\Phi(K, \omega, n, \phi, \lambda)$ in section 5.1, we can calculate the filtering effect quantitatively. Define $\epsilon(n)$ as the ratio of equation (3.57) to (3.55):

$$\epsilon(n) = \frac{F_d(\omega, n, z)}{F_\theta(\omega, n, z)} = \frac{\int\int \frac{2f^2 r_n^2}{(K^2 + f^2 r_n^2)} \frac{\Phi(K, \omega, n)}{2\pi K} W(k, L_a) dk dl}{\int \frac{2f^2 r_n^2}{(K^2 + f^2 r_n^2)} \Phi(K, \omega, n) dK}, \tag{5.26}$$

$\epsilon(n)$ represents the filtering effect for each mode due to the range average. If $L_a = 0$, then $W(k, L_a) = 1$, $\epsilon(n) = 1$ which means no filtering at all. Substitution of equation (5.1) into the above equation yields

$$\epsilon(n) = \frac{\int\int \frac{2f^2 r_n^2}{(K^2 + f^2 r_n^2)} \frac{C_n(K)}{2\pi K} W(k, L_a) dk dl}{\int \frac{2f^2 r_n^2}{(K^2 + f^2 r_n^2)} C_n(K) dK}. \tag{5.27}$$

Because the form of $C_n(K)$ has been specified by equation (5.6), given the nondimensional length of acoustic ray L_a, we can calculate $\epsilon(n)$ through equation (5.27). Table 5.1 gives $\epsilon(n)$ of the first two baroclinic modes: n=1 and n=2, for three different values of L_a.

	n=1	n=2
$L_a = 0$	1	1
$L_a = 10$	0.85	0.84
$L_a = 20$	0.7	0.67
$L_a = 60$	0.46	0.44

Table 5.1 $\epsilon(n)$: the filtering effect due to range average.

Because the dimensional length of the ray path is $\hat{L}_a = L_a L$, the dimensional value of $L_a = 10$ is 1000 km. Table 5.1 shows that when the length of the acoustic ray path is 6000 km, the energy level will drop by one half. As we have mentioned in section 3.6, the above results are based on the assumption spatial homogeneity and isotropy. Because the energy level in the real data changes by several orders of magnitude across the ocean basin, it's very hard to extract the filtering effect due to range–average form the real data.

The observed temperature frequency spectra for rays **k** and **n** from ATOC and the corresponding model spectra are plotted in figures 5.5 and 5.6. For the model spectrum, we use the mean value of the surface eddy kinetic energy along the path as the energy level and the mean value of the vertical gradient of mean temperature along the ray path as the vertical gradient of mean temperature of the model. Figure 5.6 shows that the model spectrum fails here. The energy level of the model spectrum is about 3 times higher than that the corresponding observed spectrum. The reason is that the ray path for **n** is longer than 2000 km and that it starts from a point near the eastern boundary and passes through the California Current, so in addition to the energy level, the vertical gradient of mean temperature changes strongly above 1000 m along the ray path. Just as we mentioned in the previous section, the equation (5.23) is inappropriate along the path where the vertical gradient of mean temperature and energy level change rapidly along the acoustic ray path.

5.3 Summary

In this chapter, we find a regional model for the energy density $\Phi(K, \omega, n, \phi, \lambda)$ of the low frequency variability in the ocean. Only the first three modes are included in our model: the barotropic and first two baroclinic modes. For each mode we choose

$$\Phi(K, \omega, n, \phi, \lambda) = C_n(K) D_n(\omega) E_0(n) I(\phi, \lambda), \tag{5.28}$$

and based on various observations, we get:

(1) the wavenumber spectral shape:

For the batropic mode: n=0

$$C_0(K) = \begin{cases} 48K^{3/2} & \text{if } K < K_0 \\ K^{-2} & \text{if } K > K_0 \ , \end{cases} \tag{5.29}$$

where $K_0 = 0.33$ is the nondimensional transitional wavenumber and the corresponding dimensional one is $\hat{K} = K/L = 3.3 \times 10^{-3}$ CPK.

For the baroclinic modes: n=1 and n=2

$$C_n(K) = \begin{cases} 16K^{-1/2} & \text{if } K < K_0 \\ K^{-3} & \text{if } K > K_0 \ . \end{cases} \tag{5.30}$$

(2) the frequency spectral shape:

For the three modes: n=0 to n=2

$$D_n(\omega) = \begin{cases} 1.5 \times 10^4 \omega^{-1/2} & \text{if } \omega < \omega_0 \\ \omega^{-2} & \text{if } \omega > \omega_0 \ , \end{cases} \tag{5.31}$$

where $\omega_0 = 0.00165$ is the nondimensional transitional frequency and the corresponding dimensional one is $\hat{\omega_0} = \omega_0/T = 0.01$ CPD.

(3) the partition among vertical modes:

$$E_0(0) = 1; \ E_0(1) = 3.2; \ E_0(2) = 5.4. \tag{5.32}$$

(4) the energy magnitude:

$$I(\phi,\lambda)=\frac{\hat{E}_k(\phi,\lambda,z=0)}{5.4\times10^7}. \tag{5.33}$$

The empirical formula for the surface kinetic energy in the North Pacific is

$$\begin{aligned}\hat{E}_k(\phi,\lambda,z=0) &= 30+\frac{32}{\sin^2\phi}+1000\exp\{-[\frac{(\lambda-50)^2}{900}+\frac{(\phi-35)^2}{50}]\}\\ &\quad -800\exp\{-[\frac{(\lambda-190)^2}{1600}+\frac{(\phi-42)^2}{200}]\},\end{aligned} \tag{5.34}$$

where λ is the longitude , ϕ is the latitude and the units of $\hat{E}_k$ are cm^2/s^2.

The empirical formula for the surface kinetic energy in the North Atlantic is

$$\begin{aligned}\hat{E}_k(\phi,\lambda,z=0) &= 50+\frac{35}{\sin^2\phi}+1000\exp\{-[\frac{(\lambda-305)^2}{400}+\frac{(\phi-43)^2}{80}]\}-\\ &280\exp\{-[\frac{(\lambda-320)^2}{2000}+\frac{(\phi-16)^2}{200}]\}-160\exp\{-[\frac{(\lambda-320)^2}{900}+\frac{(\phi-16)^2}{50}]\}\end{aligned} \tag{5.35}$$

where the units of $\hat{E}_k$ are cm^2/s^2.

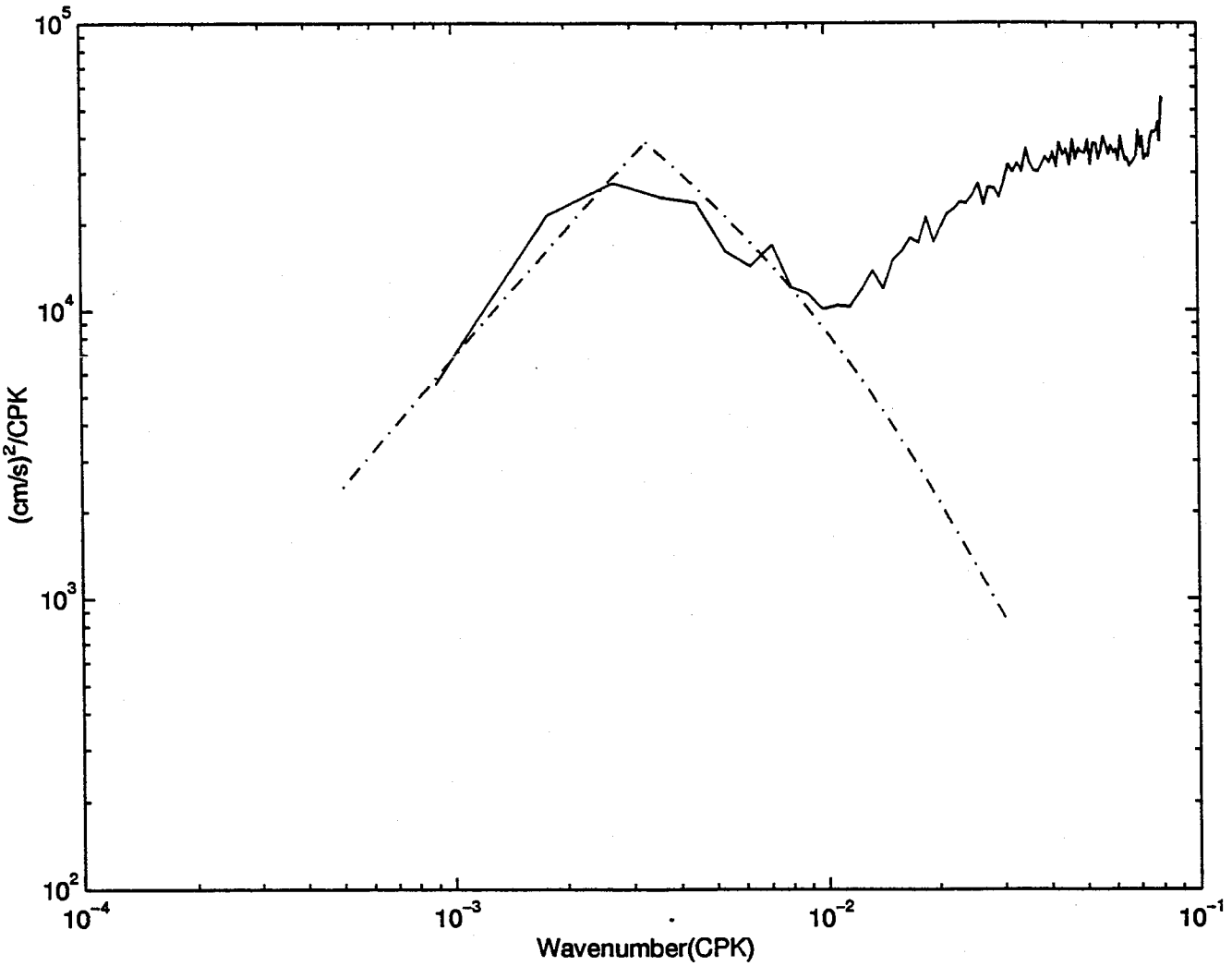

Figure 5-1: Kinetic energy wavenumber spectrum. Solid line is the observed spectrum from 10° × 10° areas between 30° and 40°N with center longitude at 330°E. Dashed line is the corresponding model spectrum.

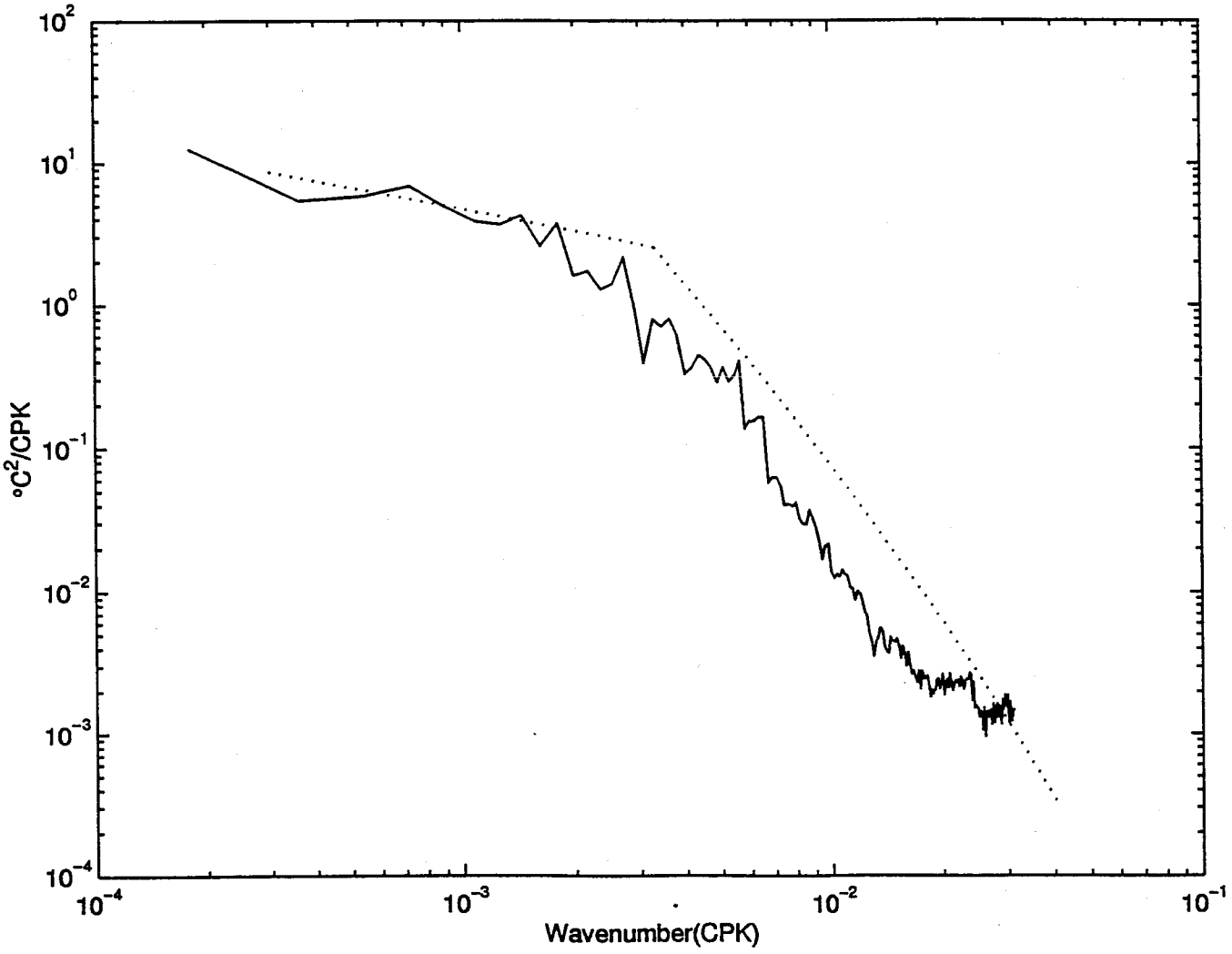

Figure 5-2: Temperature wavenumber spectrum. Solid line is the observed spectrum at depth of 800m from XBT data between San Francisco and Hawaii. Dashed line is the model spectrum.

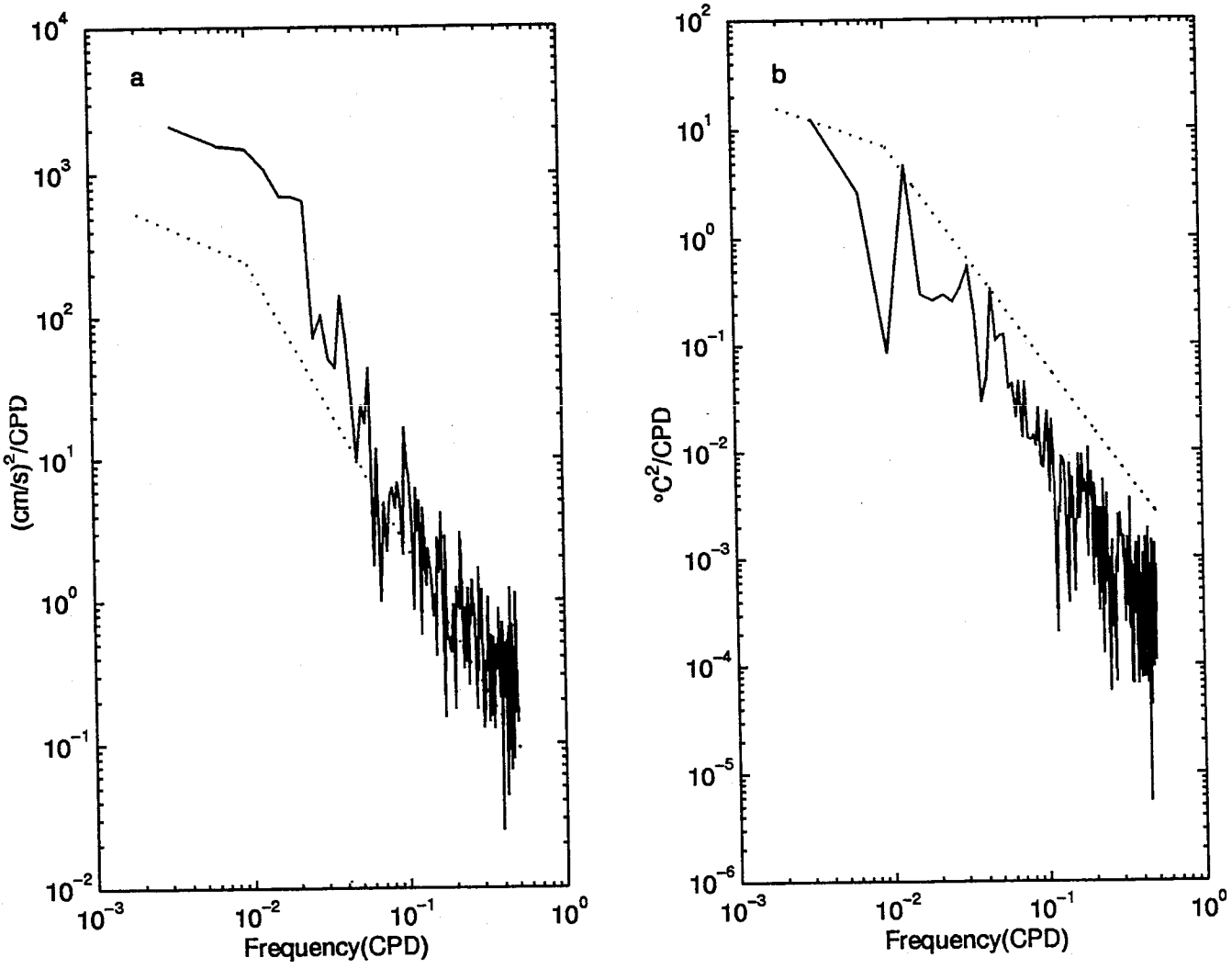

(i)

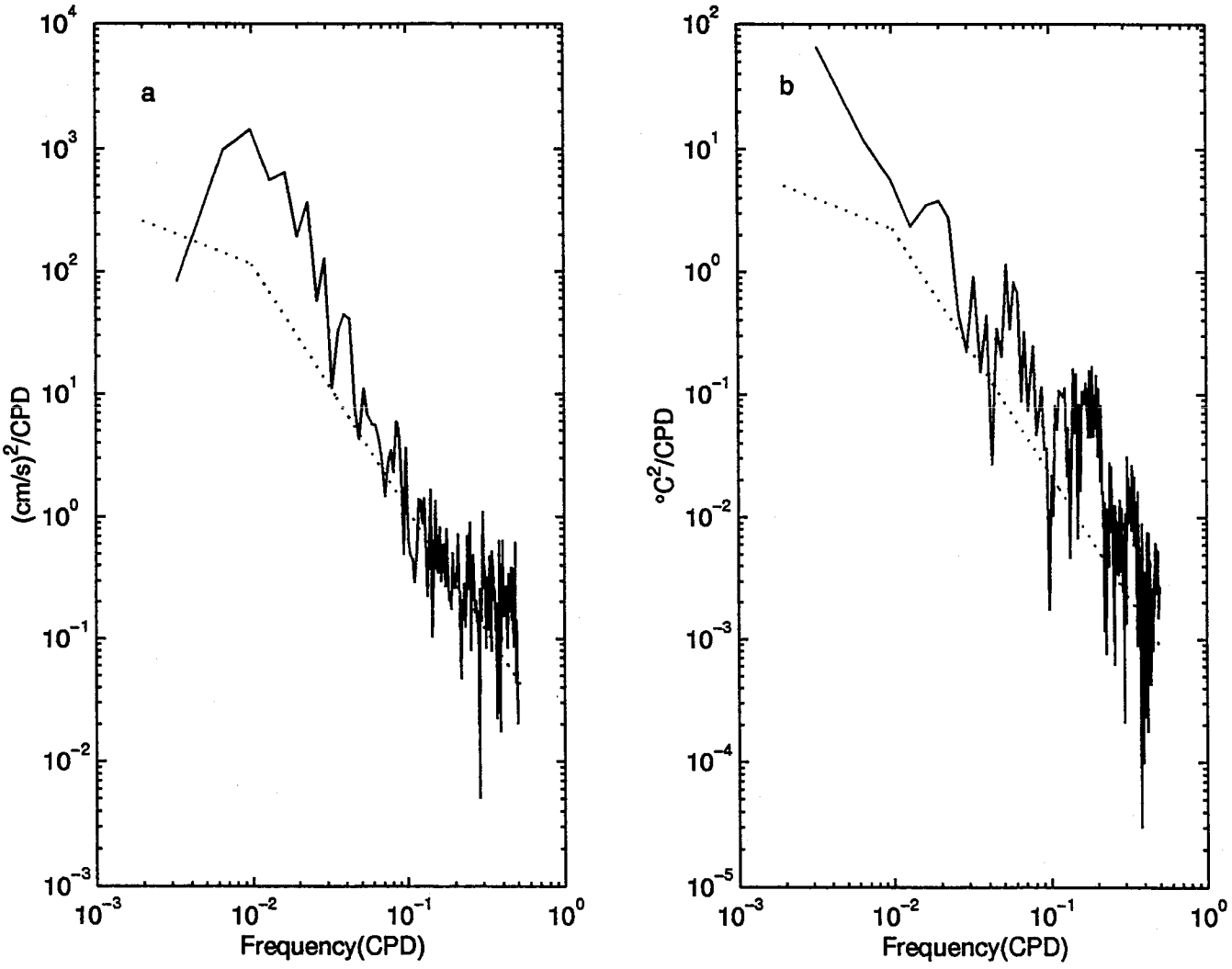

(ii)

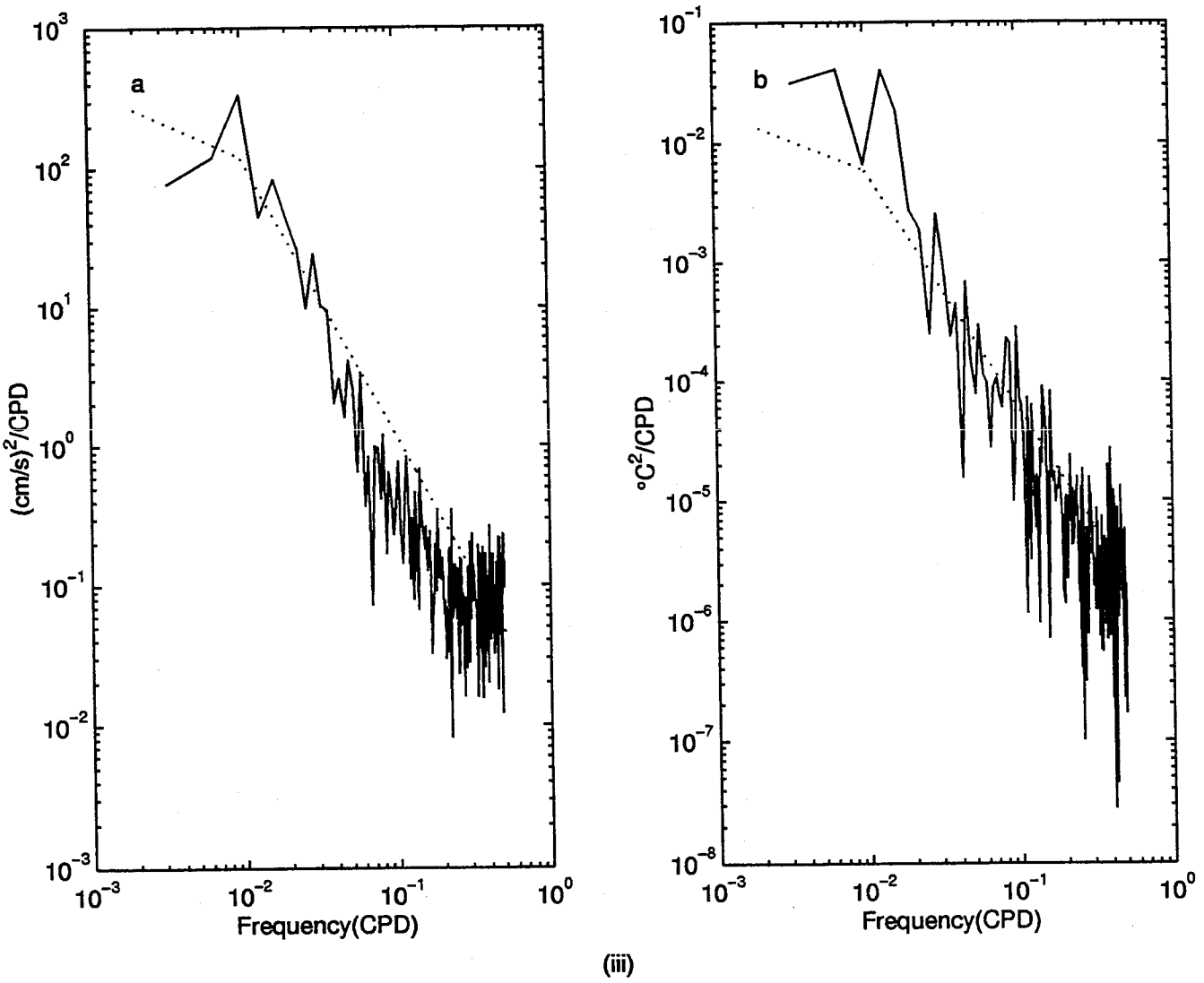

Figure 5-3: Frequency spectra of kinetic energy (a) and temperature (b) at depths of 560m (i), 1160m (ii) and 3050m (iii) at (33.2°N,338.1 °E). Solid line is the observed spectrum and dashed line is the model spectrum.

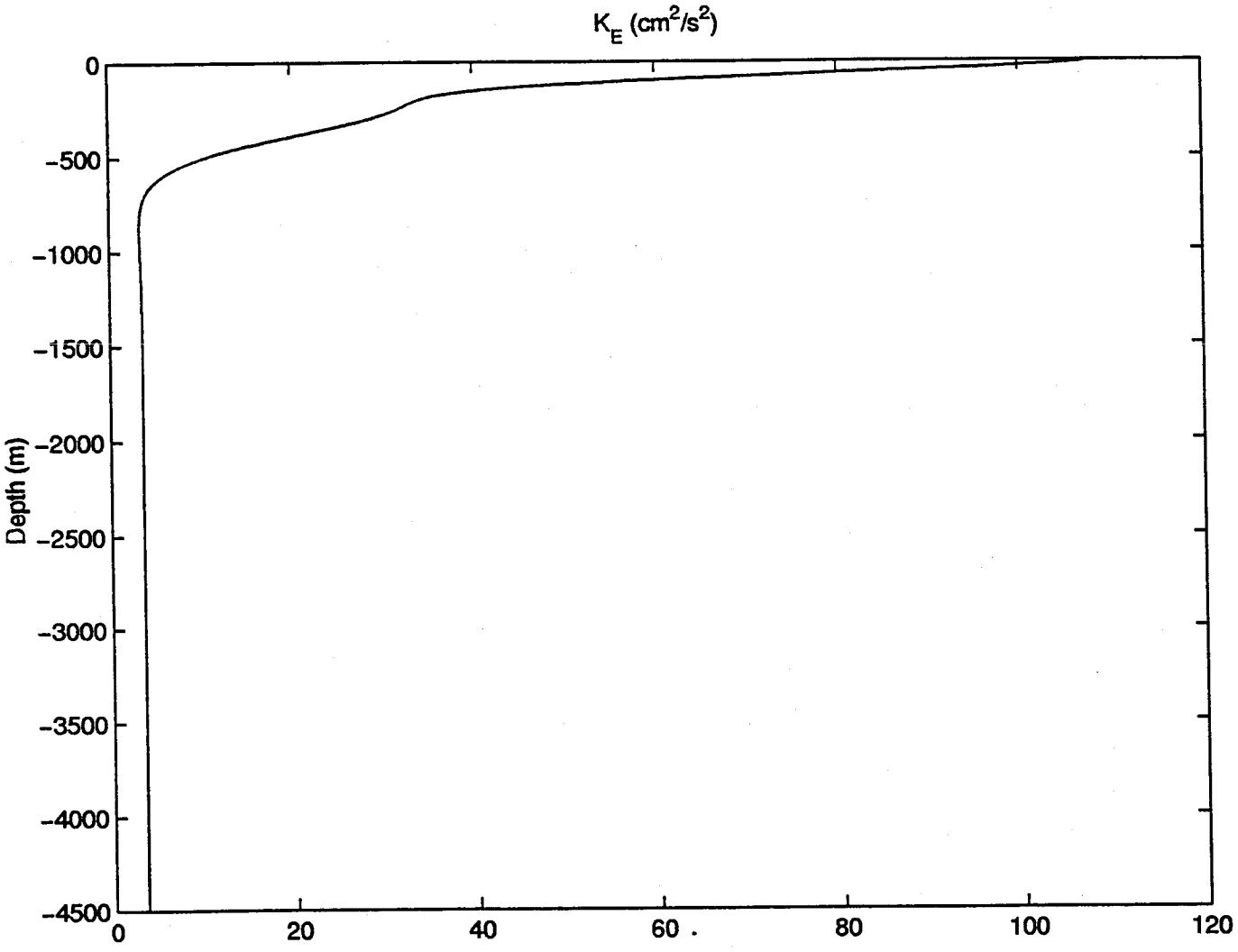

Figure 5-4: Vertical profile of the model kinetic energy at (33.2°N, 338.1°E).

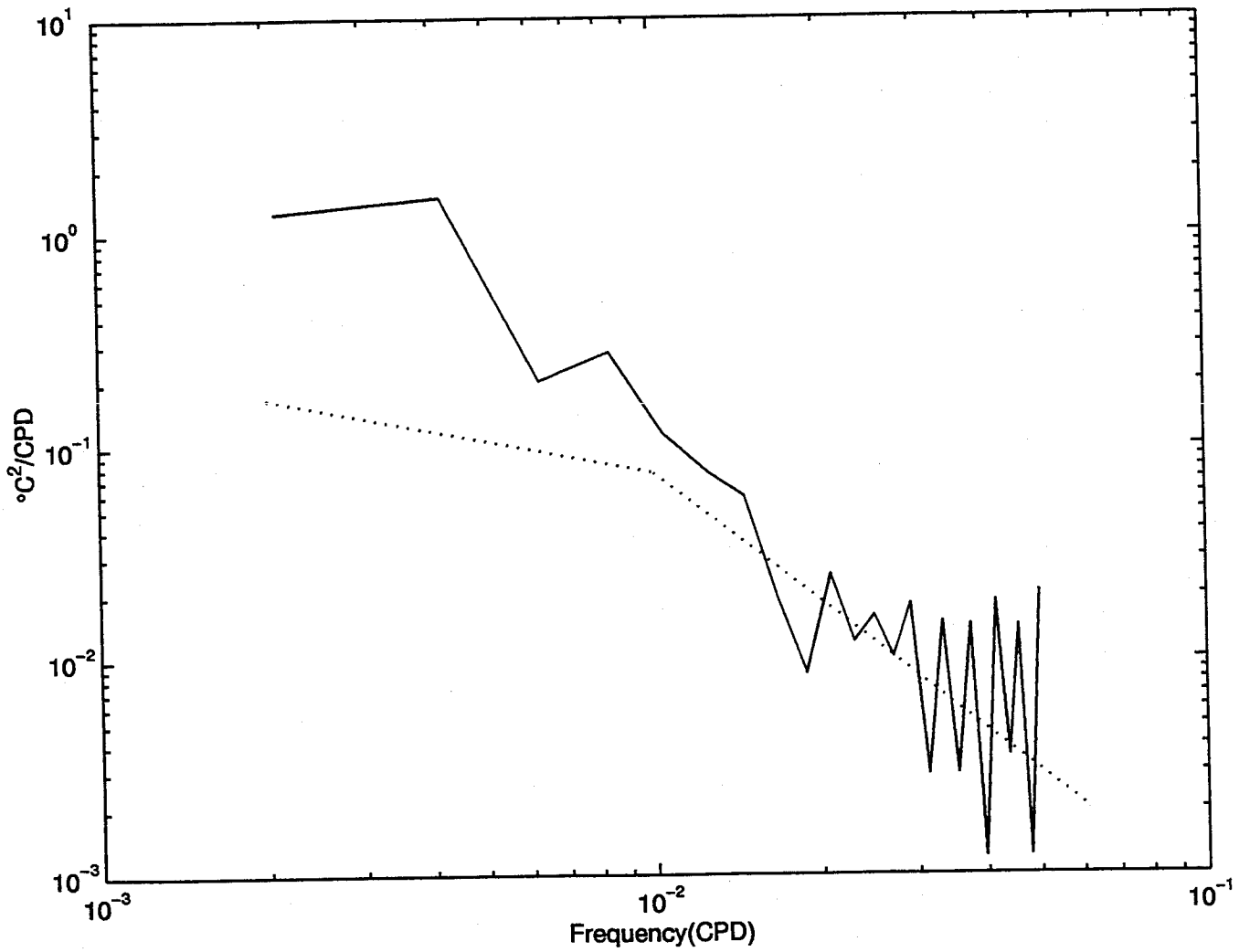

Figure 5-5: The observed range– and depth–averaged temperature frequency spectrum for the ray path "k" from ATOC (solid line) and the corresponding model spectrum (dashed line).

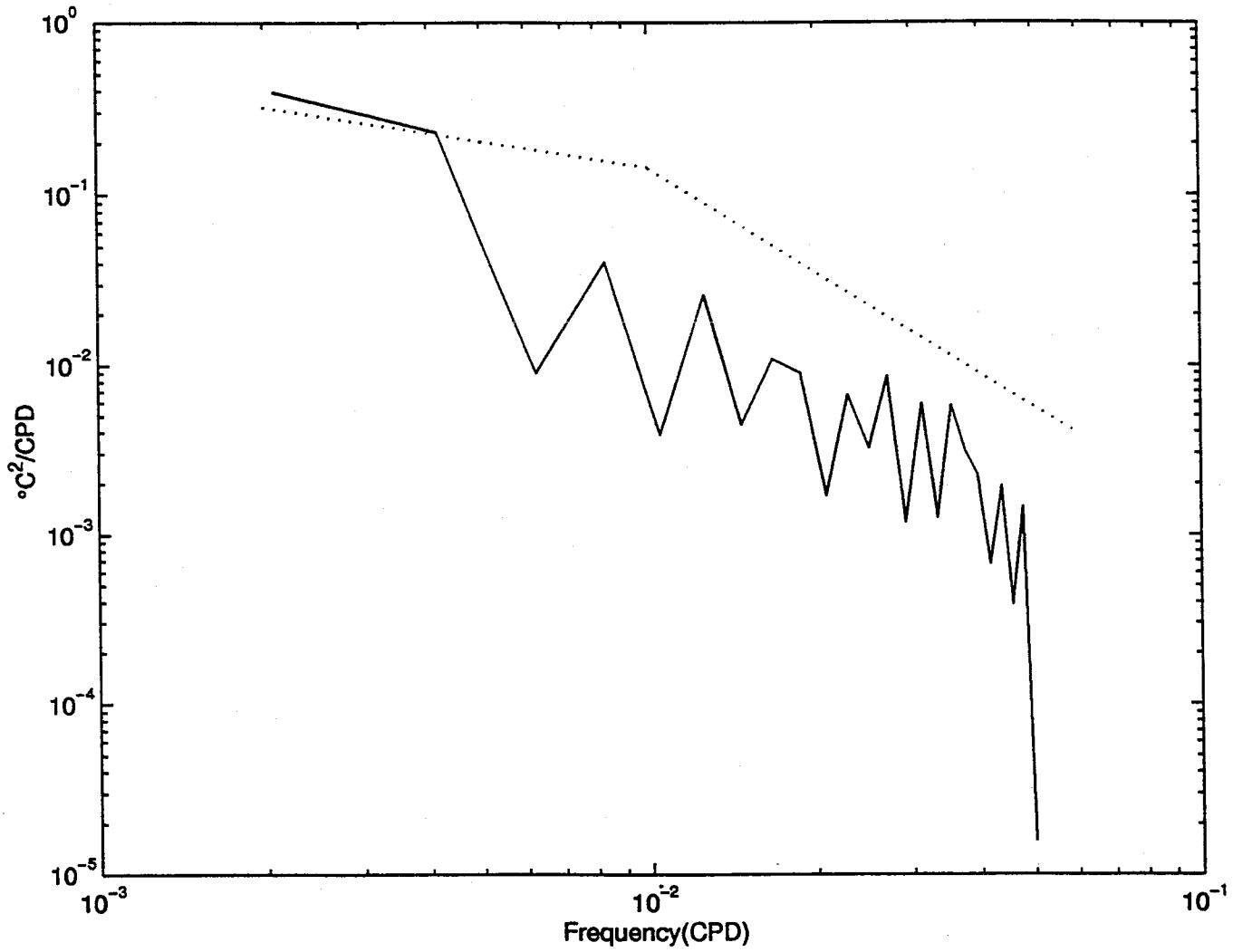

Figure 5-6: Same as in figure 5.7 except for ray path "n".

Chapter 6

Conclusion and discussion

Our work can be summarized as a spectral description of ocean low frequency variability and an attempt to contrive a simple empirical algebraic representation of the distribution of low frequency variability energy in wavenumber/frequency space.

The observations presented in chapter 4 suggest that a universal frequency/wavenumber spectrum does not exist for the low frequency variability because statistical properties such as the energy level and degree of baroclinicity are very sensitive to the physical environment. However, to zero order there are some properties independent of geography. The frequency spectra of velocity and temperature always show a steep decay with a spectral slope of about -2 at frequencies higher than 0.01 CPD and a flat slope at low frequencies. The wavenumber spectra of the velocity follows a $k^{+3/2}$ relation at wavenumbers smaller than about 0.003 CPK, k^{-1} relation at wavenumbers between 0.003 CPK and 0.007 CPK and k^{-2} relation at shorter wavelengths. The wavenumber spectra for the temperature from XBT data follows a $k^{-1/2}$ relation at wavenumbers smaller than about 0.003 CPK and a steeper decay with a slope of -3 at larger wavenumbers. The transitional point in the temperature wavenumber spectra and velocity wavenumber spectra is coincident both are at about 0.003 CPK. We show that the relationship between the observed wavenumber spectrum of kinetic energy and that of temperature is consistent with the thermal wind relation. The frequency and wavenumber spectral shape is independent of depth as well. The vertical

profile of kinetic energy is very similar across the middle ocean. Most of the kinetic energy of low frequency variability is confined to the upper ocean above 1000 m. To a good first approximation the vertical structure of the kinetic energy can be simply represented by the barotropic and the first baroclinic modes.

The low frequency variability is a function of frequency, wavenumber, vertical mode and space. Although we have shown that the tomographic measurements behave as a low–pass filter, the horizontal inhomogeneity makes it difficult to identify this filtering effect in the data. The spectral representation in wavenumber space is appropriate only in the areas where the statistical properties are relatively homogeneous. In order to overcome the difficulties associated with the inhomogeneity, we can only break the global ocean into regions where the statistical properties change slowly with geography.

Roughly speaking, there exists a regional energy density for low frequency variability. A regional model spectrum for the low frequency variability was developed in chapter 5. The model frequency spectra of temperature and kinetic energy include a parameter which represents the geography–dependent part. The model wavenumber spectra of kinetic energy are appropriate where the energy magnitude is relatively homogeneous. The model wavenumber spectra of temperature and the model frequency spectra of tomographic data are valid where both the energy magnitude and the vertical gradient of mean temperature vary slowly with geography.

If the regional energy density $\Phi(K,\omega,n,\phi,\lambda)$ is normalized by the geography–dependent factor $I(\phi,\lambda)$, we get the universal factors of the energy density, $\Phi(K,\omega,n) = C_n(K)D_n(\omega)E_0(n) \propto K^p\omega^q$. The observed kinetic energy and temperature wavenumber spectra suggest $p = 3/2$ at $K < K_0$ and $p = -2$ at $K > K_0$ for the barotropic mode, and $p = -1/2$ at $K < K_0$ and $p = -3$ at $K > K_0$ for the baroclinic mods, where K_0 is the transitional wavenumber of the wavenumber spectra. The observed frequency spectra of temperature and kinetic energy suggest that $q = -1/2$ for $\omega < \omega_0$ and $q = -2$ for $\omega > \omega_0$, where ω_0 is the transitional frequency of the frequency spec-

tra. The combination of satellite altimetry and current meter measurements suggests the vertical structure of the low frequency variability is governed by the barotropic and first two baroclinic modes. The normalized energy density which is universal is shown in Figure 6.1.

The present model has the following assumptions

(1) We assume that the energy distribution is isotropic. The assumption of horizontal isotropy is only valid at the high frequency and high wavenumber bands. At the low frequency and low wavenumber bands, there is more energy in the east–west direction.

(2) We assume that the observations at different times can be reasonably related, which implies the oceanic variability is stationary in time.

(3) The basic state is steady and the bottom of the ocean is flat.

(4) Last but not least, we assume that the buoyancy frequency N(z) is universal and can be modelled by an idealized exponential form.

Identifying where the energy of low frequency variability in the ocean comes from is an interesting problem. There are many mechanisms for the oceanic low frequency varibility [Wunsch 1981]. Some theoretical work suggests that the eddy energy is generated mainly by instability processes of intense boundary current and is radiated subsequently into the interior ocean by Rossby waves [Pedlosky 1977, Hogg 1988]. Based on the five years of high quality altimetric data from TOPEX/POSEIDON, we can obtain the three dimensional spectrum of the sea surface height $\eta(k, l, \omega)$. The three dimensional spectrum can help us to identify the direction of wave propagation and thus, to answer the question whether there is energy generated by the western boundary current and radiated subsequently into the interior.

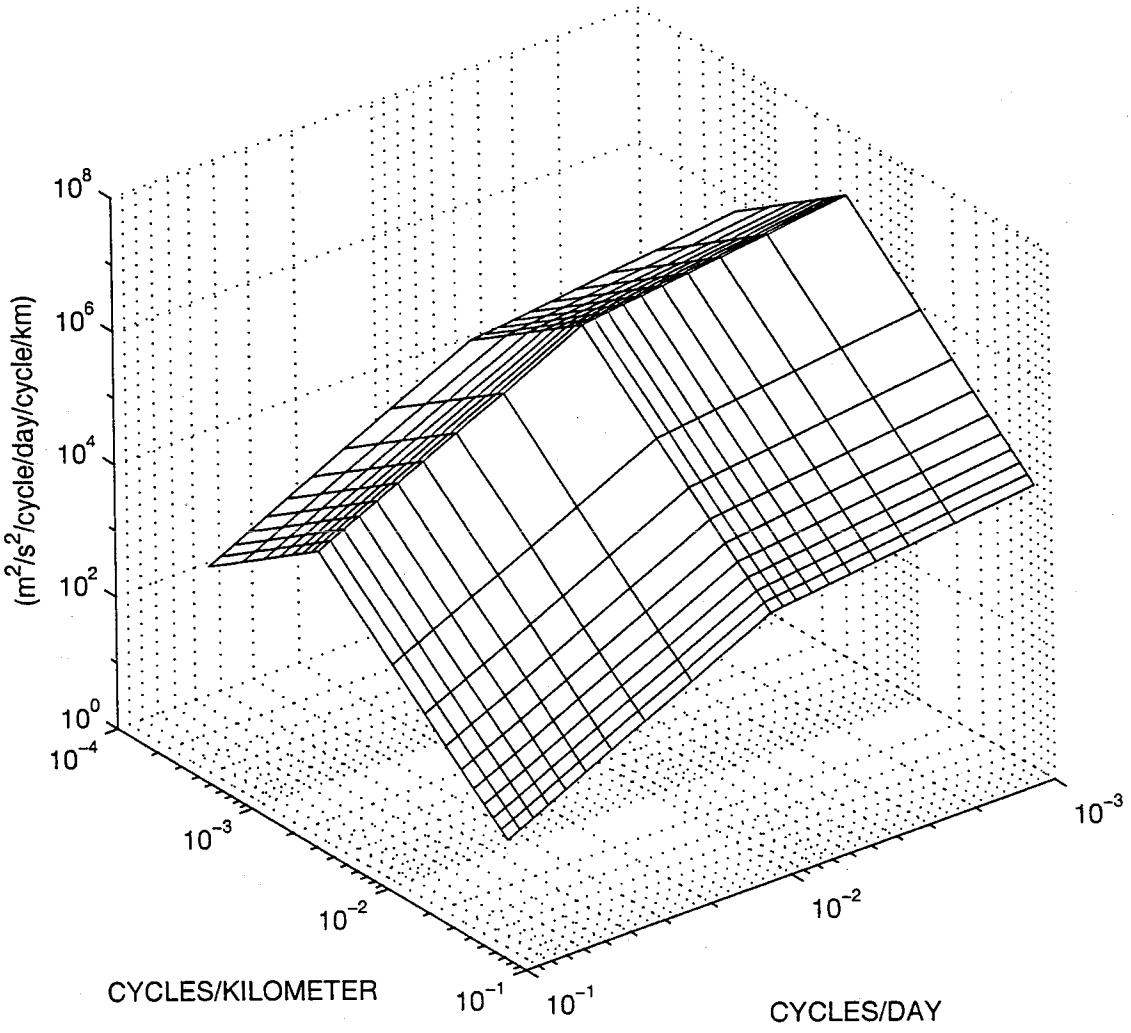
10^8
10^6
10^4
10^2
10^0
$(m^2/s^2/cycle/day/cycle/km)$
10^{-4}
10^{-3}
10^{-2}
10^{-1}
CYCLES/KILOMETER
10^{-1}
10^{-2}
10^{-3}
CYCLES/DAY

(a)

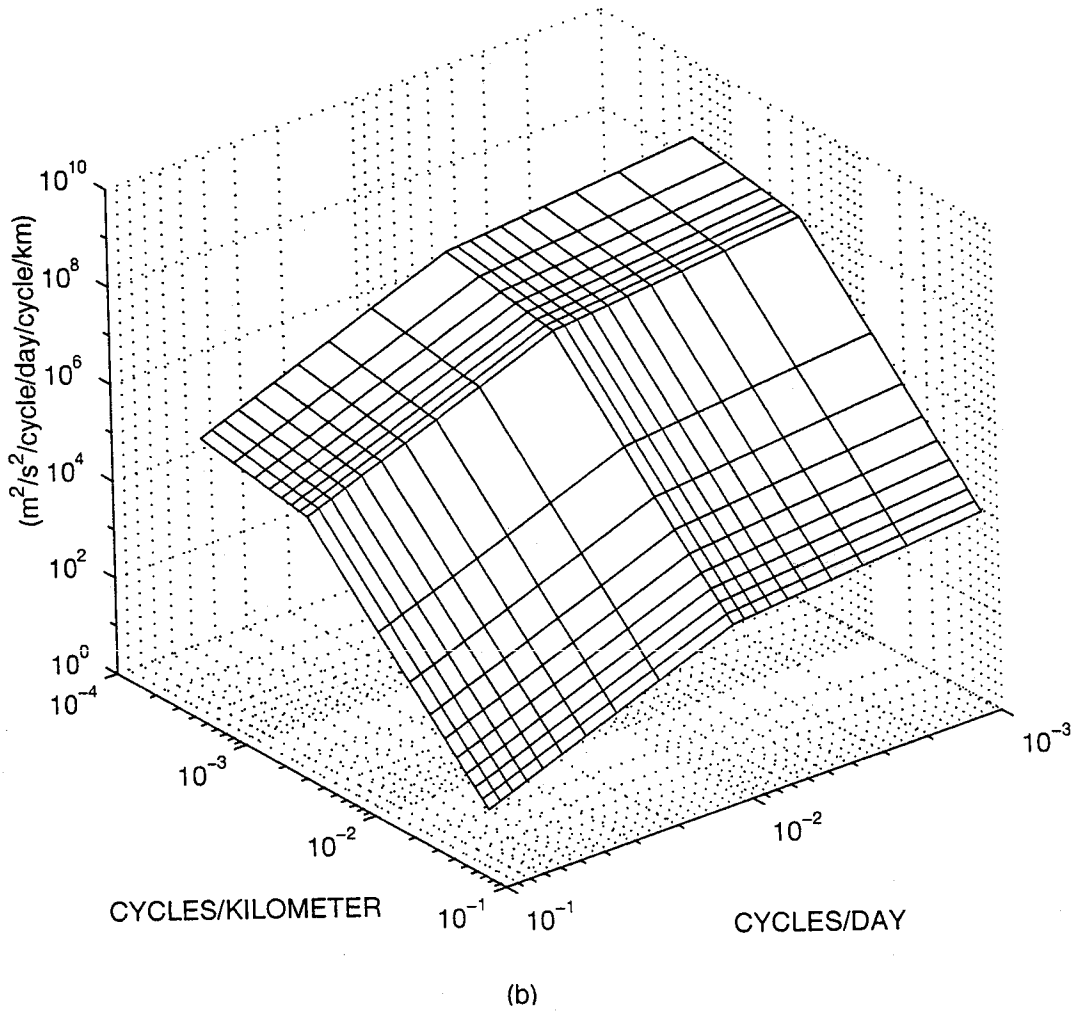

(b)

Figure 6-1: The universal factors of the energy density. (a) for the barotropic mode (b) for the first two baroclinic modes.

Bibliography

[1] Abramowitz, M. and I. A. Stegun, 1964. *Handbook of mathematical functions, with formulas, graphs, and mathematical tables.* Dover Publications, New York, 1046 pp.

[2] Bender, C. M. and S. A. Orszag, 1978. *Advanced mathematical methods for scientists and engineers.* McGraw-Hill, New York, 593 pp.

[3] Charney, J. G., 1971. Geostrophic turbulence. *J. Atmos. Sci.*, 28, 1087-1095.

[4] Dushaw, B. D., P. F. Worcester, B. D. Cornuelle, and B. M. Howe, 1993a. On equations for the speed of sound in seawater. *J. Acoust. Soc. Am.*, 93, 255-275.

[5] Dushaw, B. D., P. F. Worcester, B. D. Cornuelle, and B. M. Howe, 1993b. Variability of heat content in the central North Pacific in summer 1987 determined from longe–range acoustic transmissions. *J. Phys. Oceanogr.*, 23, 2650-2666.

[6] Dushaw, B. D., P. F. Worcester, B. D. Cornuelle, and B. M. Howe, 1994. Barotropic currents and vorticity in the central North Pacific Ocean during summer 1987 determined from long–range reciprocal acoustic transmissions. *J. Geophys. Res.*, 99, 3263-3272.

[7] Dushaw, B. D., B. M. Howe, J. A. Mercer, and R. C. Spindel, 1996. Acoustic receptions at SOSUS arrays "**k**" and "**l**" of transmissions from Pioneer Seamount and Pacific basin acoustic thermometry. *ATOC Occasional Notes,* N0. 35.

[8] Emery, W. J., W. G. Lee, and L. Maagard, 1984. Geographic and seasonal distribution of Brunt-Väisälä frequency and Rossby radii in the North Pacific and North Atlantic. *J. Phys. Oceanogr.*, 14, 294-317.

[9] Fu, L. -L., and G. R. Flierl,1980. Nonlinear energy and enstrophy transfers in a realistically stratified ocean. *Dynamics of Atmospheres and Oceans*, 4, 219-246.

[10] Garrett, C., and W. Munk, 1972. Space-time scales of internal waves. *Geophys. Fl. Dyn.*, 3, 225-264.

[11] Garrett, C., and W. Munk, 1975. Space-time scales of internal waves: a progress report. *J. Geophys. Res.*, 80, 291-297.

bibitem Gill, A. E., 1982. *Atmosphere-Ocean Dynamics*. Academic Press, 662 pp.

[12] Hogg, N. G., 1988. Stochastic wave radiation by the Gulf Stream. *J. Phys. Oceanogr.*, 18, 1687-1701.

[13] LeBlond, P. H., and L. Mysak, 1978. *Waves in the ocean*. Elsevier, New York, 602 pp.

[14] Levitus, S., and T. P. Boyer, 1994. *World ocean atlas 1994*. Vol. 4,*Temperature*, NOAA Atlas NESDIS 4, U.S.GOV.Printing Office, 117 pp.

[15] Munk, W. H., 1981. Internal waves and small-scale process. In *Evolution of Physical Oceanography. Scientific Surveys in Honor of Henry Stommel*, ed. B. Warren and C. Wunsch, 264-291. MIT Press, Cambridge, Massachusetts.

[16] Munk, W., P. F. Worcester and C. Wunsch, 1996. Ocean Acoustic Tomography. Cambridge University Press, Cambridge, 433 pp.

[17] Munk, W., and C. Wunsch, 1979. Ocean acoustic tomography: a scheme for large scale monitoring. *Deep-Sea Res.*, 26, 123-161.

[18] Munk, W., and C. Wunsch, 1982. Observing the oceans in the 1990s. *Phil. Trans. Roy. Soc.*, A307, 439-464.

[19] Munk, W., and C. Wunsch, 1997. The moon and mixing: abyssal recipes II. *Deep-Sea Res.*, in press.

[20] Müller, P., D. J. Olbers, and J. Willebrand, 1978. The IWEX spectrum. *J. Geophys. Res.*, 83, 479-500.

[21] Pedlosky, J., 1977. On the radiation of mesoscale energy in the mid–ocean. *Deep-Sea Res.*, 24, 591-600.

[22] Pedlosky, J., 1987. *Geophysical fluid dynamics.* Springer-Verlag, New York, 710 pp.

[23] Richman, J. G., 1976. Kinetics and energetics of the mesoscale mid-ocean circulation: mode, Ph.D. thesis, Massachusetts Institute of Technology/Woods Hole Oceanographic Institution, 205 pp.

[24] Richman, J. G., C. Wunsch and N. G. Hogg, 1977. Space and time scales of mesoscale motion in the sea. *Rev. Geophys.*, 15, 385-420.

[25] Rhines, P. B., 1977. The dynamics of unsteady currents. In "The Sea" (E. D. Goldberg et al., eds.), vol. 6, Chapter 7. Wiley, interscience, New York, pp. 189-318.

[26] Roden, G. I., 1975. On North Pacific temperature, salinity, sound velocity and density fronts and their relation to the wind and energy flux fields. *J. Phys. Oceanogr.*, 5, 577-571.

[27] Roemmich, D., and B. Cornuelle, 1990. Observing the fluctuations of gyre-scale ocean circulation: a study of the subtropical South Pacific. *J. Phys. Oceanogr.*, 20, 1919-1930.

[28] Schmitz, W. J., Jr., 1978. Observations of the vertical distribution of low frequency kinetic energy in the western North Atlantic. *J. Marine Res.*, 36, 295-310.

[29] Schmitz, W. J., Jr., 1988. Exploration of the eddy field in the mid-latitude North Pacific. *J. Phys. Oceanogr.*, 18, 459-468.

[30] Schmitz, W. J., Jr., 1996. On the world ocean circulation: volumme I some global features/north atlantic circulation. Woods Hole Oceanographic Institution Technical Report. WHOI-96-03 .

[31] Stammer, D., 1997. Global characteristic of ocean variability estimated from regional TOPEX/POSEIDON altimeter measurements. *J. Phys. Oceanogr.*, 27, 1743-1770.

[32] Stammer, D., R. Tokmakian, A. Semtner, and C. Wunsch, 1996. How well does a 1/4° global circulation model simulate large-scale oceanic observations? *J. Geophys. Res.*, 101, 25 779-25 812.

[33] Worcester, P. F., B. D. Dushaw, and B. M. Howe, 1990. Gyre-scale current measurements using reciprocal acoustic transmissions. *Proc. Fourth IEEE Working Conference on Current Measurement,* Clinton, MD, IEEE, 65-70.

[34] Wunsch, C., 1981. Low-frequency variability in the sea. In *Evolution of Physical Oceanography. Scientific Surveys in Honor of Henry Stommel,* ed. B. Warren and C. Wunsch, 342-374. MIT Press, Cambridge, Massachusetts.

[35] Wunsch, C., 1997. The vertical partition of oceanic horizontal kinetic energy. *J. Phys. Oceanogr.*, 27, 1770-1794.

[36] Wunsch, C., and R. Hendry, 1972. Array measurements of the bottom boundary layer and the internal wave field on the continential slope. *Geophys. Fl. Dyn.*, 4, 101-145.

[37] Wunsch, C., and D. Stammer, 1995. The global frequency-wavenumber spectrum of oceanic variability estimated from TOPEX/POSEIDON altimeter measurements. *J. Geophys. Res.*, 100, 24,895-24,910.

[38] Wunsch, C., and D. Stammer, 1997. Atmospheric loading and the oceanic "inverted barometer" effect. *Rev. Geophys.*, 35, 79-107.